RCA Review

Thermal Image from
64 × 128 PtSi IR-CCD Camera

December 1982 Volume 43 No. 4

RCARCI 43(4) 567–695 (1982)

Our cover shows a thermal image obtained from an IR-CCD camera made up of PtSi Schottky-barrier detectors discussed in the paper by Elabd and Kosonocky in this issue. Shown on the right is the scene (a man holding a match) from which the thermal image was obtained. The blue in the cover photo is due to film processing; the actual image as seen on a TV screen is in black and white.

RCA Review, published quarterly in March, June, September, and December by RCA Research and Engineering, RCA Corporation, Princeton, New Jersey 08540. Entered as second class matter July 3, 1950 under the Act of March 3, 1879. Second-class postage paid at Princeton, New Jersey, and at additional mailing offices. Effective January 1, 1983, subscription rates as follows: United States: one year $12.00, two years $21 00, three years $27.00; in other countries: one year $14.00, two years $24 50, three years $31.50. Single copies up to five years old $5.00

RCA
Review

RCA Review (ISSN 0033-6831) is a technical journal published quarterly by RCA Research and Engineering in cooperation with the subsidiaries and divisions of RCA.

Contents

569 **Theory and Measurements of Photoresponse for Thin Film Pd_2Si and PtSi Infrared Schottky-Barrier Detectors with Optical Cavity**
Hammam Elabd and Walter F. Kosonocky

590 **Piezoresistivity Effects in Plastic-Encapsulated Integrated Circuits**
Kenneth M. Schlesier, Scott A. Keneman, and Richard T. Mooney

608 **Proximity Printing of Chrome Masks**
Dietrich Meyerhofer and Joe Mitchell

626 **Real Frequency Broadband Matching Using Linear Programming**
B. S. Yarman

655 **Forces Acting on the Tool in VideoDisc Mastering**
Rabah Shahbender

665 **A Diamond-Like Carbon Film**
Joseph Zelez

675 **Sine-Wave Threshold Contrast Sensitivity Function: Dependence on Display Size**
C. R. Carlson

684 **Patents**
687 **Authors**
691 **Index to Volume 43, 1982**

December 1982 Volume 43 Number 4 **ISSN 0033-6831**

RCA Corporation

Thornton F. Bradshaw Chairman and Chief Executive Officer
Robert R. Frederick President and Chief Operating Officer

Editorial Advisory Board

Chairman, **J. J. Tietjen** RCA Laboratories
G. C. Hennessy RCA Laboratories
H. Kressel RCA Laboratories
J. Kurshan RCA Laboratories
W. J. Merz Laboratories RCA, Ltd.
A. Pinsky RCA Laboratories
K. H. Powers RCA Laboratories
R. E. Quinn RCA Laboratories
C. C. Richard International Licensing
A. H. Teger RCA Laboratories
W. M. Webster RCA Laboratories
B. F. Williams RCA Laboratories

Editor **Ralph F. Ciafone**

Assoc. Editor **Rita L. Strmensky**

Editorial Representatives

D. R. Higgs Missile and Surface Radar
C. Hoyt Consumer Electronics Division
T. E. King RCA Research and Engineering
R. Mausler National Broadcasting Company
M. Rosenthal RCA Americom, Inc.
J. Schoen Solid State Division
M. G. Pietz RCA Advanced Technology Laboratories
W. S. Sepich Commercial Communications Systems Division
J. E. Steoger RCA Service Company
D. Tannenbaum Government Communications Systems
F. Yannotti RCA Astro-Electronics

© RCA Corporation 1983. All rights reserved, except that express permission is hereby granted for the use in computer-based and other information-service systems of titles and abstracts of papers published in RCA Review.

Theory and Measurements of Photoresponse for Thin Film Pd_2Si and PtSi Infrared Schottky-Barrier Detectors With Optical Cavity

Hammam Elabd and Walter F. Kosonocky
RCA Laboratories, Princeton, NJ 08540

Abstract—A model for the photoyield of Schottky-barrier detectors (SBDs) with optical cavity is presented that is in a very good agreement with the measured data obtained on two types of developed thin-film PtSi SBDs. According to this model the photoyield (Q.E.) of these thin-film SBDs of 1.0 and 2.0% at a wavelength of 4.0 μm is 17 and 32 times higher than the photoyield of a thick-film SBD with Q.E. of 0.06%. The improvement by a factor of 4.93 and 3.46 is attributed to the increase of optical absorptance, and the additional improvement by a factor of 3.45 and 9.25 is due to an increase in the internal photoemission due to scattering (reflection) of hot holes at the surfaces of the thin-film silicide. An improvement of the photoresponse by about a factor of 2.0 is predicted by the model and has been experimentally verified. This improvement is due to use of a tuned optical cavity which includes an AR coating on the back side of the substrate and an optimum thickness of dielectric between the thin-film PtSi and the aluminum mirror.

1. Introduction

Recently high-performance PtSi and Pd_2Si Schottky-barrier IR-CCD image sensors were developed at RCA Laboratories with 32 × 63 and 64 × 128 detector elements.[1-6] The first generation Pd_2Si Schottky-barrier detector (SBD) arrays were developed for 1.0 to 2.4 μm short-

wave-infrared (SWIR) satellite-borne applications requiring passive cooling or operation at about 120K.[2,3,5] The PtSi SBD arrays were developed for 3.0 to 5.0 μm medium-wave-infrared (MWIR) thermal imaging applications.[1,4,6] These focal plane arrays (FPAs) require operating temperature of about 80K. At the present time, the SBD FPAs developed at RCA Laboratories represent the most advanced staring FPA available for operation with TV compatible frame rates and up to *f*/3.0 optics.[4,6]

This paper reviews photoemission theory and describes its application to the operation of thin-film PtSi and Pd_2Si SBDs. A model based on the theory that is in good agreement with experimental data is also presented. The original electron photoemission model from metals into vacuum was described by Fowler.[7] In the 1960's Fowler's photoyield model was modified based on studies of internal photoemission of hot electrons from metal films into a semiconductor.[8] The most commonly used expression for photoyield and responsivity of SBDs is the equation of Cohen, Vims, and Archer,[8,9] The photoemission model of thin-film SBD and p-type silicon substrate presented in this paper (1) is in better agreement with the experimental data in SWIR range than the modified Fowler photoyield expression and (2) gives the actual value of the photoyield (confirmed by data) as a function of the structural parameters of the thin-film SBDs with an optical cavity and a metalic mirror.

2. High Performance Thin-Film Pd_2Si and PtSi SBDs

2.1 Detector Structure

The construction of recently developed high-performance thin-film PtSi SBDs with optical cavity is shown in Fig. 1.[1,4] The PtSi film thickness is 20 to 100 Å. A 2000 to 10000 Å dielectric layer is deposited

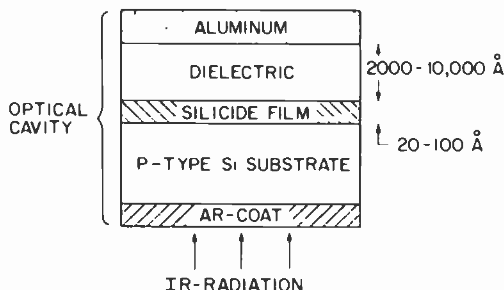

Fig. 1—The Schottky-barrier IR detector structure with optical cavity.

on the silicide film followed by an aluminum mirror. The back side of the silicon substrate is AR coated. The structure is back illuminated. The structure is designed to induce (1) an enhanced optical absorptance as a result of multiple pass of the light in the film and (2) an increase in the injection (emission) efficiency of hot holes into the substrate. The increase in the injection efficiency is the result of hot hole scattering (reflection) at the silicide-dielectric interface and will be referred to as the internal quantum efficiency gain G.

2.2 Responsivity and Quantum Efficiency

Responsivity and quantum efficiency (Q.E.) measured as a function of wavelength of the high-performance PtSi and (first generation) Pd_2Si SB detectors are shown in Fig. 2.[1-6] The experimental points are compared in this figure with the commonly used equation[8,9] of Cohen et al for the SBD responsivity R expressed as

$$R = C_1\left(1 - \frac{\Psi_{ms}\lambda}{1.24}\right)^2 \quad \text{(A/W)} \qquad [1]$$

where C_1 is the quantum efficiency coefficient in eV^{-1}, Ψ_{ms} is the metal-semiconductor Schottky-barrier in eV, and λ is the wavelength of the infrared radiation.

The theoretical curves in Fig. 2 represent the least square fit of the experimental points to Eq. [1] in the 3–6 μm range. The parameters C_1 and Ψ_{ms} are determined from the slope and the intercept of equation

$$\sqrt{Y\,h\nu} = \sqrt{C_1}\,(h\nu - \Psi_{ms}), \qquad [2]$$

where $Y = Rh\nu$ is the photoyield (quantum efficiency).

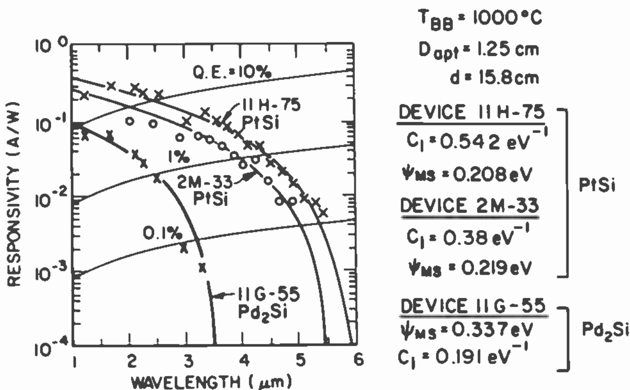

Fig. 2—Measured responsivity of thin PtSi and Pd_2Si high-performance Schottky-barrier detectors.

Inspection of Fig. 2 shows that Eq. [1] predicts too high a value for the responsivity R at short wavelengths. The model for the photoyield of an infrared SBD described in Sections 3.3 and 3.4 predicts the above discrepancy and provides a description for the C_1 coefficient in terms of the structural parameters of the thin-film SBD.

3. Photoyield Model for an Infrared SBD

3.1 Theory of Internal Photoemission

The operation of the Schottky barrier infrared detector is based on the internal photoemission of hot holes across the Schottky barrier Ψ_{ms} that is formed between the silicide layer and the p-type silicon substrate. The absorption of IR-radiation takes place in the metal silicide electrode as shown in Fig. 3. The absorbed IR photons excite valence electrons in the metal silicide to states above the fermi level, leaving behind holes. The "hot" holes are those that have energies higher than the Schottky barrier,

$$\Psi_{ms} = \phi_s - \phi_m + (E_{fs} - E_v) = X_0 + E_G - \phi_m, \quad [3]$$

$E_G = h\nu_{max}$

$\Psi_{ms} = \phi_S - \phi_M + (E_{fs} - E_V)$

$= X_0 + E_G - \phi_M$

Fig. 3—Simplified energy band diagram illustrating the photoemission in a PtSi or a Pd_2Si SBD.

where ϕ_s and ϕ_m are the work functions of the semiconductor and the metal, E_{fs} is the fermi energy, E_v is the energy at the top of the valence band, and X_0 is the electron affinity of the semiconductor.

The minimum light frequency required to excite a hole above the Schottky barrier is ν_0, corresponding to a photon energy $h\nu_0$. Under the zero temperature approximation, for metal, which is a reasonable approximation for PtSi at the temperature of 77K,

$$h\nu_0 = \Psi_{ms}. \qquad [4]$$

3.2 Escape (Emission) Probability of Hot Holes for Thick-Film SBD

The escape (emission) probability for an excited hole in the silicide depends on the relationship between the energy of the excited hole E and the barrier height Ψ_{ms}. As shown in Fig. 4, for zero-temperature approximation, the excited hole with $E \leq \Psi_{ms}$ (i.e., a cold hole) has an escape probability of about zero for a wide barrier. However, an excited hole with $E \geq \Psi_{ms}$ (i.e., a hot hole) has an escape probability $P(E)$, which is defined by the criterion requiring that the momentum of the hot hole normal to the silicide-silicon interface correspond to a kinetic energy greater than the barrier Ψ_{ms}. As illustrated by Fig. 5, the escape probability of a hot hole $P(E)$ can be expressed as

$$P(E) = \frac{2\pi E^2(1 - \cos\theta)}{4\pi E^2} = \frac{1 - \cos\theta}{2}, \qquad [5]$$

where $\cos\theta = \sqrt{\Psi_{ms}/E}$, E is the hole energy referred to the fermi level and θ defines the solid angle for the escape of hot holes with energy E. The critical (maximum) escape angle θ_0 for the radiation with photon

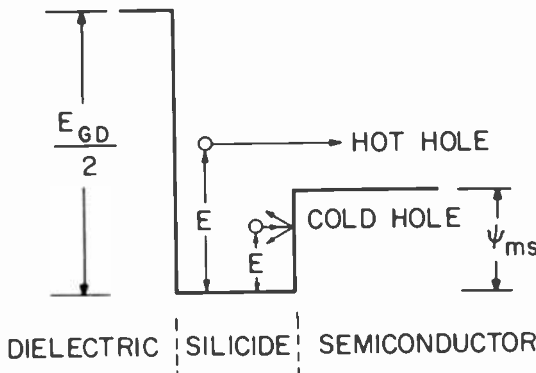

Fig. 4—Illustration of the hot hole emission over the Schottky barrier.

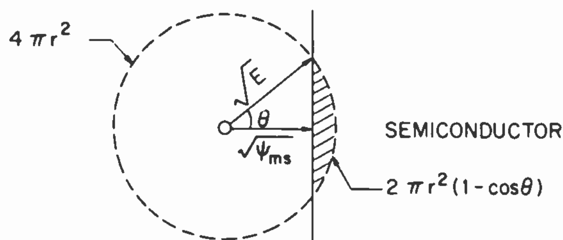

$P(E) = \frac{1}{2}(1 - \cos\theta)$

Fig. 5—Graphic representation of the solid angle for escape of hot holes.

energy $h\nu$ or at wavelength λ is defined by the equation

$$\theta_0 = \cos^{-1}\sqrt{\frac{\Psi_{ms}}{h\nu}} = \cos^{-1}\sqrt{\frac{\Psi_{ms}\lambda}{1.24}}. \qquad [6]$$

The variation of the critical escape angle θ_0 with wavelength is shown in Fig. 6. For PtSi SBDs operating in the 3–5 μm band (MWIR), θ_0 varies between 43° and 20°. For Pd_2Si SBD, θ_0 varies between 58 and 31° in the 1 to 2.5 μm SWIR range.

For thick metal films the variation of the escape probability with the wavelength of incident radiation is shown in Fig. 7. For PtSi-SBD, $P(E)$ is below 13% in the MWIR band; while for Pd_2Si-SBD, $P(E)$ is below 19% in the SWIR band.

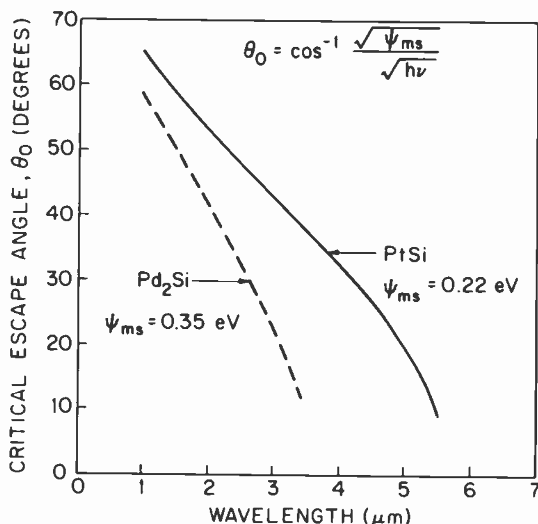

Fig. 6—The critical escape angle of hot holes versus the wavelength of the incident photon for a PtSi and a Pd_2Si SBD with Ψ_{ms} of 0.22 eV and 0.35 eV, respectively.

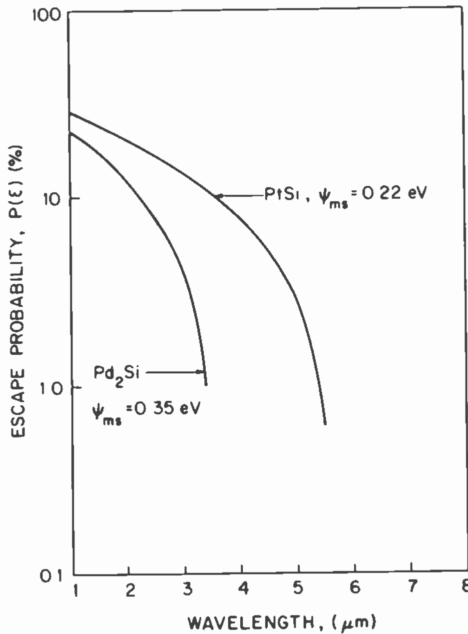

Fig. 7—Escape (emission) probability of hot holes from PtSi and Pd_2Si layers into silicon.

The escape probability for cold holes is larger than zero for a Schottky barrier with narrow barrier width. The cold hole tunneling probability can be calculated from a simple quantum mechanical model that takes into account the wave nature of the carriers.[10] For example, the tunneling probability of a 0.1-eV hole through the 0.15-eV barrier of IrSi SBD drops from 1 to 10^{-9} as the barrier width increases from 10 to 100 Å.

3.3 Photoyield of Thick-Film SBD

For typical infrared light frequencies, $h\nu << E_f$. Therefore, it is reasonable to assume in the case of PtSi and Pd_2Si detectors that the density of states dN/dE, the probability of excitation of any hole, and the mean free path are constant over the excitation range.[8*] In addition, the zero temperature approximation for metals allows us to define a sharp threshold for photoemission at Ψ_{ms}. Following Archer's analysis,[8] the total number of possible excited states for holes, as shown in

* This assumption is not valid, however, for the case of IrSi detectors where the 5*d* and 6*p* bands do not overlap.[10]

Fig. 3, is

$$N_T = \int_0^{h\nu} \frac{dN}{dE}\, dE = \frac{dN}{dE}\, h\nu. \qquad [7]$$

The number of states N from which hole emission across the barrier Ψ_{ms} may occur is

$$\begin{aligned} N &= \int_{\Psi_{ms}}^{h\nu} \frac{dN}{dE} P(E)\, dE \\ &= \frac{1}{2}\frac{dN}{dE} \int_{\Psi_{ms}}^{h\nu} \left[1 - \left(\frac{\Psi_{ms}}{E}\right)^{1/2}\right] dE \\ &= \frac{1}{2}\frac{dN}{dE} (h\nu - 2\sqrt{\Psi_{ms} h\nu} + \Psi_{ms}) \\ &= \frac{1}{2}\frac{dN}{dE} h\nu \left(1 - \sqrt{\frac{\Psi_{ms}}{h\nu}}\right)^2 \text{ or} \end{aligned} \qquad [8]$$

$$N = \frac{1}{2}\frac{dN}{dT} h\nu (1 - \cos\theta_0)^2 \qquad [9]$$

where θ_0 is defined by Eq. [6].

Assuming that the mean free path for hot holes is much longer than the penetration depth of infrared radiation (see Sec. 4.1), the internal quantum efficiency Y_i of SBD for the infrared radiation absorbed in the silicide film can be expressed using Eqs. [7]–[9] as

$$Y_i = \frac{N}{N_T} = \frac{1}{2}\left(1 - \sqrt{\frac{\Psi_{ms}}{h\nu}}\right)^2 \qquad [10]$$

or

$$Y_i = \frac{1}{2}(1 - \cos\theta_0)^2. \qquad [11]$$

The external quantum efficiency (photoyield) may be expressed as follows:

$$Y = A(\lambda) Y_i$$

$$Y = \frac{A(\lambda)}{2}\left(1 - \sqrt{\frac{\Psi_{ms}}{h\nu}}\right)^2 \qquad [12]$$

$$Y = \frac{A(\lambda)}{2}\left(1 - \sqrt{\frac{\Psi_{ms}\lambda}{1.24}}\right)^2$$

$$Y = \frac{A(\lambda)}{2}(1 - \cos\theta_0)^2. \qquad [13]$$

Here $A(\lambda)$ is the optical absorptance in the spectral window of the detector and is defined as the ratio of irradiance (optical power) absorbed by the silicide film to the incident irradiance on the SBD. Generally $A(\lambda)$ for thick metals is below 10%; for very thin Pt and Pd films, it can be as high as 20 to 60% (see Secs. 4.1 to 4.3).

For light frequencies around ν_0, where $h\nu_0 = \Psi_{ms}$, Eq. [8] may be approximated by

$$N = \int_{\Psi_{ms}}^{h\nu} \frac{dN}{dE}\left(\frac{E - \Psi_{ms}}{4E}\right) dE. \quad [14]$$

It follows that in this case the internal quantum efficiency can be expressed as

$$Y_i = \frac{(h\nu - \Psi_{ms})}{4\,h\nu} - \frac{\Psi_{ms}}{4\,h\nu}\ln\left(\frac{h\nu}{\Psi_{ms}}\right) \approx \frac{1}{8\,\Psi_{ms}}\frac{(h\nu - \Psi_{ms})^2}{h\nu}. \quad [15]$$

The external quantum efficiency (photoyield) corresponding to Eq. [15] is

$$Y = \frac{A(\lambda)}{8\Psi_{ms}}\frac{(h\nu - \Psi_{ms})^2}{h\nu}$$

$$= C_1\frac{(h\nu - \Psi_{ms})^2}{h\nu}, \quad [16]$$

where C_1 is given by

$$C_1 = \frac{A(\lambda)}{8\,\Psi_{ms}}. \quad [17]$$

At this point it should be noted that Eqs. [15] to [17] differ from the equation of Cohen et al[8] for electron emission by the proportionality factor, i.e., in Eq. [15] the proportionality factor is

$$\frac{1}{8\,\Psi_{ms}} \quad [18]$$

instead of

$$\frac{1}{8[E_f + \Psi_{ms}]} \quad [19]$$

as given in Ref. [8]. This implies that for SBDs with constant density of states the photoyield and the so called quantum efficiency coefficient C_1 are inversely proportional to the barrier height Ψ_{ms}. This is consistent with measurements performed on our SBDs, where we have lowered the Schottky barrier, Ψ_{ms}, by increasing the doping of the surface of the p-type silicon substrate with boron implants.[10]

3.4 Photoyield of Thin-Film SBD

In thin-film SBDs, in which the thickness of the silicide t is much smaller than the attenuation length L of hot holes,[11] an increase in the escape probability of hot holes is expected due to the scattering (reflections) of the hot holes at the silicide surfaces. As illustrated in Fig. 8, the angle of the hot hole to the normal of the silicide-silicon interface θ_1 is larger than the maximum escape angle θ_0. After scattering (reflection) at the silicide-silicon and silicide-dielectric interfaces, the hot hole may acquire an angle $\theta_2 < \theta_0$ and be emitted into the silicon.

According to this model for thin-film SBD, the hot hole with $\theta > \theta_0$ can be reflected up to n times from either the silicide-silicon or the silicide-dielectric interface before its energy E is reduced to the value of Ψ_{ms}. This can be expressed as

$$E \exp\left(-\frac{2nt}{L}\right) = \Psi_{ms}, \quad [20]$$

$$n = \frac{L}{2t} \ln\left(\frac{E}{\Psi_{ms}}\right), \quad [21]$$

where t is the metal film thickness and L is the projected mean free path in the direction normal to the interface, or the attenuation length measured from the photoresponse variation with film thickness after correcting for changes in the absorptance.[11] In this model we assume that at each reflection, the energy of the hot hole is conserved but the angle of reflection is uncorrelated with the angle of incidence. The loss of energy of the hot hole, described by the attenuation length, is attributed to the hot hole scattering with phonones and the barrier scattering in the thin silicide film.

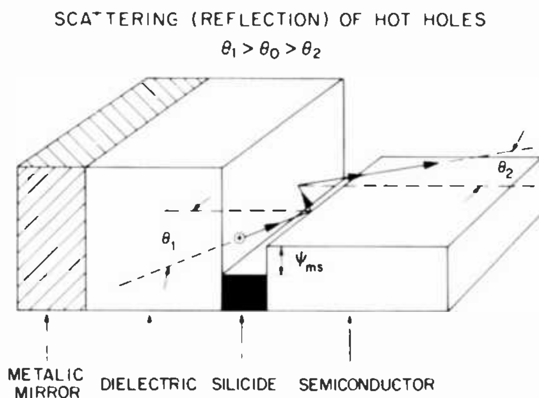

Fig. 8—Graphic representation of the scattering process of hot holes at the potential barriers at the silicide-silicon and silicon-dielectric interface.

For IR radiation with energy $h\nu$, the maximum number of reflections n_{max} is

$$n_{max} = \frac{L}{2t} \ln\left(\frac{h\nu}{\Psi_{ms}}\right). \qquad [22]$$

According to this model, the escape probability $P_t(h\nu)$ of a hot hole with energy $E = h\nu$ in a thin-film silicide can be approximated by

$$\begin{aligned} P_t(h\nu) = P(h\nu) &+ P(h\nu)\exp\left(\frac{-2t}{L}\right) \\ &+ P(h\nu)\exp\left(\frac{-4t}{L}\right) \cdots \\ &+ P(h\nu)\exp\left(\frac{-2nt}{L}\right) \end{aligned} \qquad [23]$$

or

$$\begin{aligned} P_t(h\nu) = \frac{1}{2}(1 - \cos\theta_0) + \frac{1}{2}(1 - \cos\theta_1) + \cdots \\ + \frac{1}{2}(1 - \cos\theta_n), \end{aligned} \qquad [24]$$

where n is defined by Eq. [22]. In Eqs. [23] and [24] we have assumed that $P(h\nu) << 1.0$ and that terms like

$$[1 - P(h\nu)]P(h\nu)\exp\left(\frac{-2t}{L}\right)$$

can be approximated by

$$P(h\nu)\exp\left(\frac{-2t}{L}\right).$$

To express the increase of internal quantum efficiency Y_i^t of thin-film SBD over the internal quantum efficiency Y_i of a thick film we introduce a quantum efficiency gain coefficient G, such that

$$Y_i^t = GY_i, \qquad [25]$$

and the photoyield, or external quantum efficiency Y_t, for a thin-film SBD is

$$Y_t = AGY_i. \qquad [26]$$

In our model for the thin-film SBD the gain coefficient G is defined as

$$G = \frac{P_t(h\nu)}{P(h\nu)}, \qquad [27]$$

where $P_t(h\nu)$ is defined by Eq. [23] or Eq. [24] and $P(h\nu)$ is defined by Eq. [5] (see Fig. 5). The gain coefficient G can be expressed as

$$G = \frac{1 - \cos\theta_0 + [n - (\cos\theta_1 + \cos\theta_2 \cdots \cos\theta_n)]}{1 - \cos\theta_0}$$

$$= 1 + \frac{n - \exp\left(\frac{t}{L}\right)\sqrt{\frac{\Psi_{ms}}{h\nu}}\,\frac{1 - \exp\left(\frac{nt}{L}\right)}{1 - \exp\left(\frac{t}{L}\right)}}{1 - \sqrt{\frac{\Psi_{ms}}{h\nu}}} \qquad [28]$$

where

$$n = \frac{L}{2t}\ln\left(\frac{h\nu}{\Psi_{ms}}\right)$$

represents the maximum number of chances that a hot hole (with energy $h\nu$) has for emission into the silicon. The solution of Eq. [28] as a function of L/t and λ is shown in Fig. 9 for $\psi_{ms} = 0.22$ eV.

At this point it should be added that the attenuation length L is expected to vary with the energy of the hot hole (i.e., from initial energy E_i to final energy E_f). Under low energy excitation conditions, the attenuation length[11] can be defined as

$$L \sim \left(\frac{1}{E_f^2} - \frac{1}{E_i^2}\right) + \frac{1}{6}\left(\frac{1}{E_f} - \frac{1}{E_i}\right). \qquad [29]$$

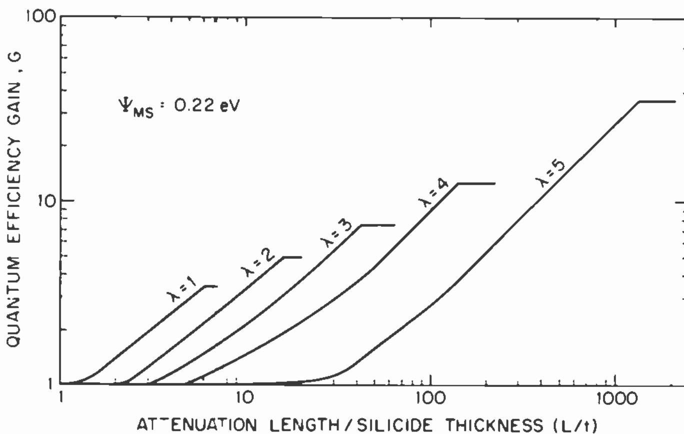

Fig. 9—Calculated quantum efficiency gain G for PtSi Schottky-barrier detector for different wavelengths versus the ratio of the hot carrier attenuation length to the silicide film thickness.

Therefore, the gain coefficient G for $h\nu$ approaching the value of Ψ_{ms} may not decrease as indicated in Fig. 9 due to longer attenuation length L. Also the maximum value of the gain coefficient G is limited to a value of $G = 1/P(h\nu)$ at which $P_t(h\nu) = 1.0$, or when all of the hot holes are emitted into the silicon.

Returning to Eq. [28], for $L >> t$ the value of G can be approximated as

$$G = \frac{sL}{t}$$

where $G > 1$. The value of s in this approximation is

$$S = \frac{1}{2}\frac{\ln(h\nu/\Psi_{ms})}{1 - \sqrt{\Psi_{ms}/h\nu}} - 1$$

where s is a constant for any given value of $h\nu$.

The external quantum efficiency (photoyield) for SBD can now be expressed as

$$Y_t = \frac{A(\lambda)G}{2}\left(1 - \sqrt{\frac{\Psi_{ms}}{h\nu}}\right)^2, \qquad [32]$$

where the gain coefficient $G = 1$ for thick-film silicide and $G > 1$ for thin-film silicide.

For light frequency, ν, close to ν_0 where $h\nu_0 = \Psi_{ms}$, the photoyield for thin-film SBD can be approximated by

$$Y = \frac{A(\lambda)G}{8\Psi_{ms}}\frac{(h\nu - \Psi_{ms})^2}{h\nu}$$

$$= C_1\frac{(h\nu - \Psi_{ms})^2}{h\nu} \qquad [33]$$

where C_1 is given by

$$C_1 = \frac{A(\lambda)G}{8\Psi_{ms}} = \frac{A(\lambda)}{8\Psi_{ms}}\frac{sL}{t} \qquad [34]$$

Fig. 10 shows the responsivity of IR-SBD as computed from Eqs. [32] and [33] where $R = Y/h\nu$ for $G = 1$ and $\Psi_{ms} = 0.22$ eV corresponding to PtSi SBD. As curves A and B show, the two models coincide above 3.5 μm. Eq. [32] predicts photoyield saturation in the SWIR where $E >> \Psi_{ms}$ and a resulting drop in responsivity, as shown on Fig. 10. This is consistent with experimental measurements on PtSi SBDs (see Fig. 14). In addition, curve C in Fig. 10 shows the theoretical limit on the responsivity of a PtSi SBD which is attained if all hot holes are emitted into silicon. This theoretical limit corresponds to $G \simeq 5$ at 1 μm and $G \simeq 100$ at 5.3 μm. This limit also assumes 100% absorptance,

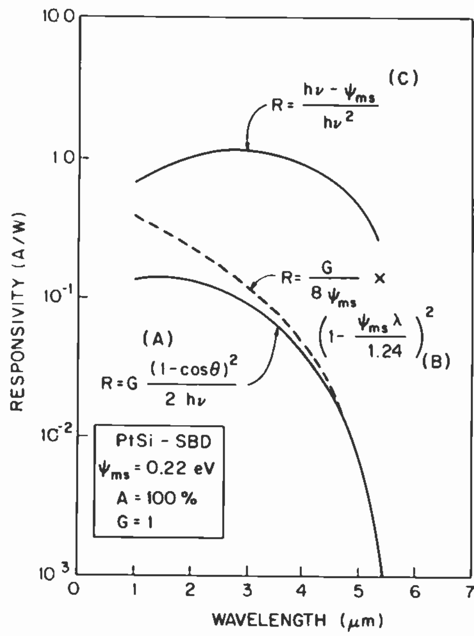

Fig. 10—Comparison of calculated responsivities of a PtSi-SBD versus wavelength for (a) an exact solution, (b) an approximation for $h\nu \approx \Psi_{ms}$, and (c) an upper limit for responsivity when $G \rightarrow \infty$.

which may be approached with an optical cavity. This limit can be expressed as:

$$Y = \frac{h\nu - \Psi_{ms}}{h\nu}. \qquad [35]$$

Fig. 11 shows the internal quantum efficiency expected from Pd_2Si SBD for the case of $G = 1$ and $A = 100\%$. Again this is compared to the theoretical limit estimated from the ratio of hot holes to the total number of excited holes.

3.5 Computer Simulation of the Absorptance

The effect of the thickness of the dielectric layer on the absorptance of the PtSi film at 4 μm for the 11H-type SBD (See Fig. 2) is shown on Fig. 12. This simulation of the absorptance in the silicide film of the SBD structure shown in Fig. 12 was computed using Fresnel equations. It was done using measured values of the index of refraction and absorption coefficient for the thin-film silicides and the two types of dielectrics. This analysis did not include reflection of the silicon-air interface (i.e., it assumes a perfect AR coat). The four curves in Fig. 12 illustrate the effect on the absorptance of the aluminum mirror and

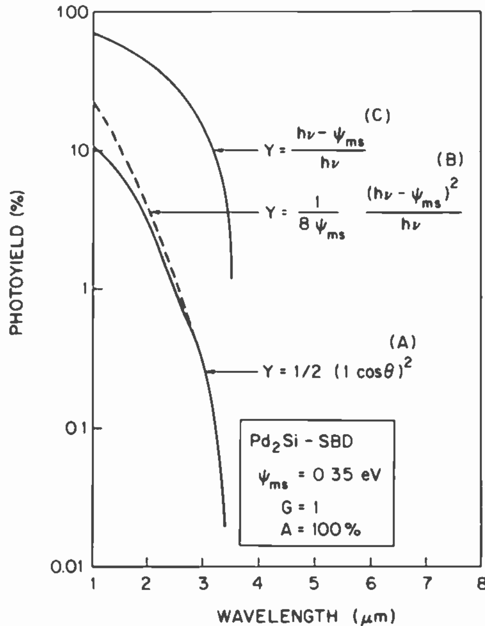

Fig. 11—Photoyield wavelength dependence of Pd_2Si-SBD for (a), (b), and (c) the same as for Fig. 10.

the variation of the thickness of the two types of dielectrics (No. 1 and No. 2) placed between the silicide and the aluminum mirror. In the case of the dielectric No. 1 the aluminum mirror enhances the absorptance by a factor of 4 at the tuning frequency.

4. Photoresponse Measurements on PtSi-SBDs with Optical Cavity

4.1 Comparison of Measured and Calculated Responsivity

The measured values (crosses) of responsivity for the 11H-type thin-film PtSi SBD are compared in Fig. 13 with three calculated curves. Curve (a), where $R = Y/h\nu$, was calculated using Eq. [32] for $AG = 1.6$ and $\Psi_{ms} = 0.208$ eV. Eq. [32] predicts the saturation of SBD responsivity in the SWIR band as is observed experimentally. This should be compared with curves (b) and (c) for the commonly used Archer photoyield expression following Eq. [33]. It should be noted that, according to Eq. [34], the quantum efficiency coefficient C_1 should be 0.95 eV^{-1} if AG is a constant and equals 1.6 across the band (see curve (b)). However, a least square fit to the data of Fig. 13 between 3.0 and 6.0 μm yields C_1 of 0.54 eV^{-1} (see curve (c)). The difference between C_1

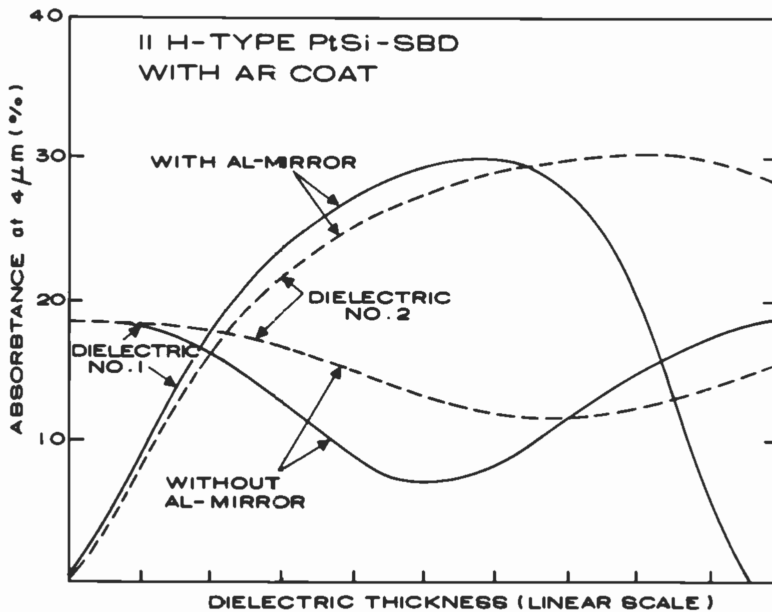

Fig. 12—Absorptance of 11H type SBD versus the thickness of two types of dielectrics.

= 0.54 eV^{-1} and C_1 = 0.95 eV^{-1} is due to inaccuracy of Eq. [33] below 4.0 μm and possible variations of the AG product across the band.

4.2 Estimated Values of Quantum Efficiency Gain Factors and Improvement of Absorptance in Thin-Film PtSi SBDs

As shown in Fig. 2, the measured values of quantum efficiency at 4 μm without AR coat of the PtSi 2M-type and 11H-type SBD are 1.0 and 2%, respectively. However, according to Eq. [32] for $G = 1.0$, $A = 5.0\%$ (see Fig. 14), and $\Psi_{ms} = 0.22$eV, the Q.E. at 4.0 μm for thick-film PtSi is 0.06%* This means that the Q.E. improvement over the thick-film PtSi SBD can be estimated to be about 17 times for the 2M-type SBD and 32 times for the 11H-type SBD. The computed absorptance without AR coating for the 2M-type SBD is ~25% and for the 11H-type is ~17% (see Fig. 12). Therefore, in the case of the 11H-type PtSi SBD, a factor of 3.46 is attributed to the improvement in absorptance and a factor of 9.25 is attributed to the enhancement of the escape (emission) probability of the hot holes due to scattering (reflection) at the silicide surfaces (or the quantum efficiency gain G). In the case of

---

* In this comparison, we assume Ψ_{ms} = 0.22 eV for all PtSi SBDs. The Q.E. of 0.06% for thick-film PtSi SBD at 4.0 μm is also in good agreement with measured values.

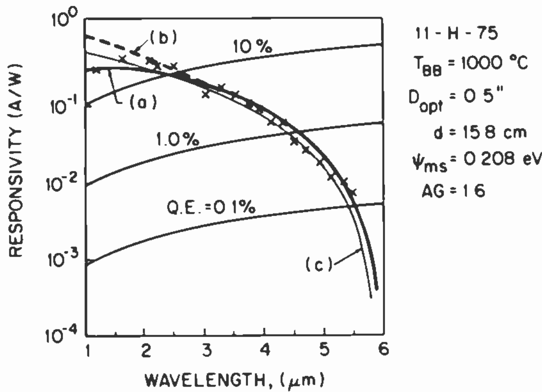

Fig. 13—Curve fitting of the measured 11H type SBD responsivity with different model equation for $AG = 1.6$ and $\Psi_{ms} = 0.208$ eV for (a) an exact expression for the responsivity (Eg. [32]), (b) an approximate expression for the responsivity following Eg. [33] for $C_1 = 0.95$ eV^{-1}, and (c) the responsivity following Eg. [33] for $C_1 = 0.54$ eV^{-1}.

the 2M-type SBD, the improvement in optical absorptance is estimated to be a factor of 4.93 over that of a thick-film PtSi SBD while the quantum efficiency gain G is estimated to be 3.45.

4.3 Optimization of Photoyield as a Function of Thickness of the Silicide Film

To illustrate the optimization of the SBD photoyield with the thickness of the silicide, Fig. 14 shows the curve of absorptance A of PtSi, the curve of the quantum efficiency gain G, and the curve of the product AG as the function of thickness of the PtSi layer normalized to the absorption length. The curve for the absorptance A computed using Fresnel equations for the case of a PtSi film on a silicon substrate is compared here with measured experimental points (triangles) at the wavelength $\lambda = 4.0$ μm. It should be noted that for a thick PtSi film, the value of the simulated absorptance A approaches 5.0%. The quantum efficiency gain curve (G) is computed by Eq. [28] (see Fig. 9) for $\lambda = 4.0$ μm, $\Psi_{ms} = 0.22$ eV, and $L = 12.5$ times the absorption length of PtSi. The value for L was determined using Eq. [28] from the estimated values G for the 2M-type and the 11-H type PtSi SBD with film thickness of 0.26 and 0.10 of the PtSi absorption length, respectively. The two experimental (estimated) points for G (solid circles) are shown in Fig. 14. An inspection of Fig. 14 shows that the peak of AG product curve for PtSi film without aluminum reflector occurs at a thickness of the PtSi layer that is less than one eighth of the absorption length of PtSi.

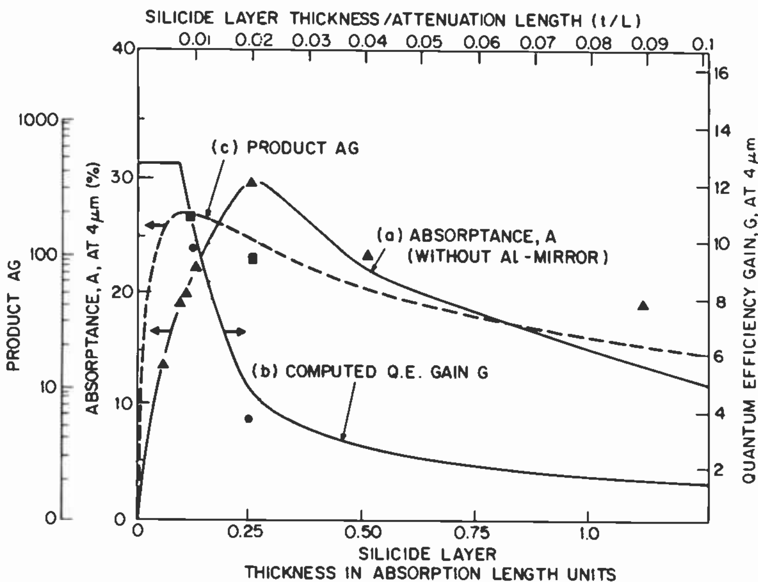

Fig. 14—The optimization of the photoyield of PtSi-SBD by (curve a) the variation of the calculated curves for absorptance *A*, (curve b) the quantum efficiency gain G and (curve c) the *AG* product as the function of the thickness of the silicide layer. The experimentally determined points for absorptance *A* are triangles, the circles are for Q.E. gain, and the squares for the *AG* product.

4.4 The Photoresponse of PtSi SBDs with Optical Cavity

The quantum efficiency of 1.0% and 2.0% for the 2M-type and the 11H-type PtSi SBDs shown in Fig. 2 were obtained without an AR coating on the back surface of silicon and with a nonoptimum thickness of the dielectric between the PtSi and the aluminum mirror. Our recent data shows that an AR coating improves the response of SBDs by a factor of about 1.3. Furthermore, data on a number of 11H-type SBDs prepared with an AR coat and an optimized thickness of dielectric (i.e., a tuned optical cavity) shows an improvement in response by a factor of 1.6 to 1.9. The above measured improvement in photoresponse is in good agreement with the calculated improvement in absorptance by a factor of 1.4 due to an optimized thickness of the dielectric (according to Fig. 12) and a factor of 1.3 due to the AR coat. Therefore, the total predicted improvement in photoresponse of the 11H-type SBDs corresponds to a factor of 1.82. Similar analysis for the 2M-type SBDs predicts a possible total improvement by a factor of 2.1.

Fig. 15 demonstrates the effect of the aluminum mirror on the photoresponse of a 32 × 63-element IR-CCD imager with 11H-type

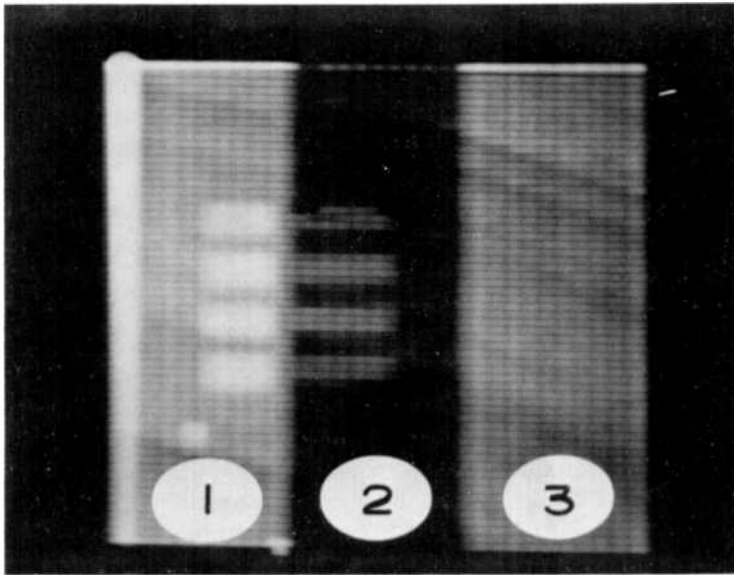

Fig. 15—Photograph of the TV monitor for a 32 × 63 element IR-CCD imager illustrating the effect of the aluminum mirror on the photoresponse.

SBDs with an optimum thickness of the dielectric over the PtSi for a tuned optical cavity. The SBDs in Region 1 were covered with full aluminum mirrors and the SBDs in Region 2 had no aluminum mirrors. The SBDs in Region 3 were covered by aluminum mirrors over about 50% of the detector area for a test not directly related to this discussion. The picture of the TV monitor shown in Fig. 15 is for a black body source 30°C above ambient positioned on Regions 1 and 2. Measurements on a number of tested imagers showed that the ratio of the response in Region 1 (with aluminum mirror) to that in Region 2 (no aluminum mirror) is between 2.5 to 3.4. These measurements are consistent with the calculated curves in Fig. 12 and represent additional conclusive evidence for the predicted enhancement of absorptance in SBDs due to the tuned optical cavity.

5. Conclusions

A model has been presented for the photoyield of the thin-film infrared Schottky-barrier detectors with optical cavity that predicts the measured data obtained for PtSi SBDs. According to this model, an improvement in the photoyield by factors of 17 and 32 for the two types of developed thin-film PtSi SBDs (2M and 11H) over the thick-film PtSi SBDs is attributed to:

(1) the improvement in optical absorptance by a factor of 4.93 for the

2M SBD and a factor of 3.46 for the 11H SBD, and

(2) the increase in the internal quantum efficiency resulting from the increased probability of emission of hot holes in thin-film silicide due to scattering at the silicide surfaces (referred to as the quantum efficiency gain G) of 3.45 for the 2M SBD and 9.25 for the 11H SBD.

According to the model presented, the attenuation length L of hot holes corresponding to energy of $h\nu = 0.31$ eV ($\lambda = 4.0$ μm) is 12.5 times the absorption length in the thin-film PtSi. The model also indicates that the 11H SBDs have about the optimal thickness of PtSi film.

Simulation of the absorptance as a function of the thickness of the dielectric between the PtSi film and the aluminum mirror predicts an improvement in photoyield due to the tuning of the optical cavity by a factor of 1.82 for the 11H-type SBDs and by a factor of 2.1 for the 2M-type SBDs. This improvement in photoyield will increase the quantum efficiency of the 11H-type SBDs from 2.0% to 3.6% at a wavelength of 4.0 μm.

High-density IR-CCD focal plane arrays with such PtSi Schottky-barrier detectors operating as staring imagers at 60 frames/second should be capable of very high-quality thermal imaging against the 300 K background.

Finally the Schottky-barrier emission model described here for thin-film PtSi SBDs can be used to optimize the performance of the photoyield of other infrared SBDs such as the Pd_2Si and the IrSi SBDs.

References:

[1] W. F. Kosonocky, H. Elabd, H. G. Erhardt, F. V. Shallcross, T. Villani, G. Meray, M. J. Cantella, J. Klein, and N. Roberts, "64 × 128-element High-Performance PtSi IR-CCD Image Sensor," 1981 IEDM, Washington, DC, Dec. 7, 1981.

[2] H. Elabd, T. Villani, and W. F. Kosonocky, "Palladium-Silicide Schottky-Barrier IR-CCD for SWIR Applications at Intermediate Temperatures," *IEEE-ED Letters*, EDL-3, p. 89, April 1982.

[3] H. Elabd, "Multispectral Earth Imaging: Applications of Metal Silicide Schottky-Barrier Mosaic Sensors," American Astronautical Society 20th Goddard Memorial Symposium on Spacelab, Space Platforms, and the Future, NASA Goddard Space Flight Center, March 17–19, 1982.

[4] W. F. Kosonocky, H. Elabd, H. G. Erhardt, F. V. Shallcross, G. M. Meray, T. S. Villani, J. V. Groppe, R. Miller, V. L. Frantz, M. J. Cantella, J. Klein, and N. Roberts, "Design and Performance of 64 × 128-Element PtSi Schottky-Barrier IR-CCD Focal Plane Array," SPIE's Tech. Symp. East '82, Arlington, VA, May 3–7, 1982.

[5] H. Elabd, T. S. Villani, and J. R. Tower, "High Density Schottky-Barrier IRCCD Sensors for SWIR Applications at Intermediate Temperature," SPIE's Tech. Symp. East '82, Arlington, VA, May 3–7, 1982.

[6] W. F. Kosonocky, H. Elabd, H. G. Erhardt, F. V. Shallcross, G. M. Meary, R. Miller, T. S. Villani, J. V. Groppe, V. L. Frantz, and F. J. Tams, III, "Schottky-Barrier Infrared Image Sensors," *RCA Engineer*, 27-3, May–June, 1982.

[7] R. H. Fowler, "The Analysis of Photoelectric Sensitivity Curves for Clean Metals at Various Temperatures," *Phys. Rev.*, **38**, p. 45 (1981).
[8] J. Cohen, J. Vilms, and R. J. Archer, "Investigation of Semiconductor Schottky Barriers for Optical Detection and Cathodic Emission," Air Force Cambridge Research Labs. Report No. 68-0651 (1968).
[9] F. D. Shepherd, R. W. Taylor, L. H. Skolnik, B. R. Capone, S. A. Roosild, W. F. Kosonocky, and E. S. Kohn, "Schottky IRCCD Thermal Imaging," *Adv. Electron Electron Phys.*, **22**, 7th Symp. Photo-Electronic Image Devices, 1979, pp. 495–512.
[10] H. Elabd and W. F. Kosonocky, to be published.
[11] J. J. Quinn, "Range of Excited Electrons in Metals," *Phys. Rev.*, **126**, p. 1453 (1962).

Piezoresistivity Effects in Plastic-Encapsulated Integrated Circuits

Kenneth M. Schlesier
RCA Laboratories, Princeton, NJ 08540

Scott A. Keneman and Richard T. Mooney
RCA Consumer Electronics Division, Indianapolis, IN 46206

Abstract—Plastic encapsulation produces compressive stress in an integrated circuit die. Stress may alter the value of diffused or implanted resistors via the piezoresistivity effect. Circuit parameters that depend on resistance or resistance ratios (a) may not meet the intended parameter design center, (b) have increased parameter distribution width due to stress variations from package to package, and (c) have parameter drifts that result in performance failure due to changes in package stress during usage.

Encapsulation stress is calculated with the Finite Element Method (FEM). The largest stress components are compressive and parallel to die edges. FEM stress values and piezoresistivity equations are used to compute effects on p-type resistors formed on a (100) substrate.

Piezoresistive analysis is applied to the Chroma/Luma IC. In the original layout, dc offsets between RGB color outputs drifted due to package stress instability. Drifts were eliminated by (a) re-layout of resistors according to piezoresistivity design rules and (b) fabrication of the original layout on 45° rotated substrates.

Parameters most sensitive to piezoresistivity are dc matching as in the Chroma/Luma and dc gains or attenuations as in D/A converters. C-clamp pressure on an IC package is an effective method of detecting sensitivity to package stress. Thermal cycling and comparison of ceramic and plastic units are also good detection methods for piezoresistivity problems.

1. Introduction

The piezoresistivity effect in silicon has been used to make strain, pressure, and force sensors,[1-9] and more recently it has been used to measure stress on a plastic-encapsulated silicon die. This paper discusses piezoresistivity effects on the electrical characteristics of integrated circuits (ICs). Linear bipolar circuits use ratio matching between *p*-type resistors extensively. Encapsulation stress can alter these ratios,

thereby affecting electrical performance. Perhaps more important, changes in encapsulation stress during usage can produce parameter drifts that result in performance failures.

Encapsulation stress has been demonstrated to be a factor in the reliability of ICs. Inayoshi et al. correlated passivation defect density with the stress produced by various encapsulaton resins.[10] Isagawa et al. reported metalization deformation as a result of encapsulation strain and thermal cycling.[11] Usell and Smiley have measured encapsulation strain with commercial piezoresistive strain sensors and have calculated stress levels with the Finite Element Method.[12] They report that strain induces cracks in dielectrics between double layer metals, and they discuss gap formation between the die surface and encapsulant. Schroen et al.[13] and Spencer et al.[14] incorporated piezoresistive stress-sensing resistors on reliability test devices. They have measured package stresses as large as 60% of silicon fracture stress for some molding compounds. They report stress effects on MOS threshold and gain, and discuss a low-temperature, long-time cycle for post-mold curing. This cycle reduces stress but increases Al metal corrosion rate during pressure cooker tests. Komatsu et al. used a diffused resistor array to derive a detailed map of stress contours across the die surface.[15] They discuss the effects of resistor orientation and show that the stress sensitivity of p-type resistors is near minimum when they are parallel to cubic [100] type crystal directions.

In Sec. 2 of this paper the stress distributions on an encapsulated die are calculated with the Finite Element Method. Sec. 3 briefly reviews piezoresistivity theory and uses FEM stresses to determine piezoresistive effects on resistors as a function of location and orientation on a (100) die surface. Piezoresistivity analysis is applied to the Chroma/Luma IC in Sec. 4. In its initial form this device had parameter drifts due to package stress instability. Two successful approaches that reduce drift to an acceptable level are presented.

2. Stress Calculation

The stress distribution in an encapsulated silicon die has been computed with the Finite Element Method (FEM). FEM requires dividing the IC package, lead frame, and die into small volume elements. The geometric distortion and centroid stress of each element can be computed with an FEM computer program. The program used for this calculation is the ANSYS Finite Element Computer Program, produced by Swanson Analysis of Houston, PA and accessed through the Westinghouse Computer Center in Pittsburgh, PA.

Inputs to the program are the set of elements described by geometry

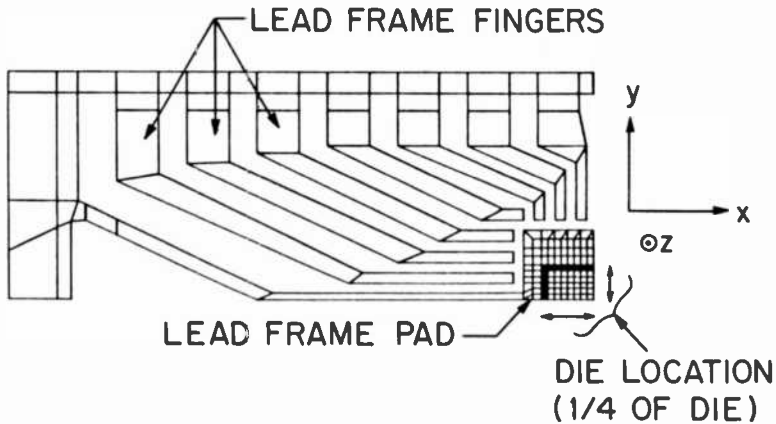

Fig. 1—Top view of elements used for FEM stress calculation.

and location, and the elastic properties of each element. Some of the elements are shown in Fig. 1. The element sizes and shapes are based on a standard 28-pin copper lead frame package and a die size of 148 by 103 mils. It was assumed that the die is mounted at the center of the lead frame so that ¼ symmetry could be used. The finest element breakup is at the silicon die location where ¼ of the chip is divided into 48 elements. The vertical dimension is divided into layers that include two levels of epoxy above and below the lead frame and die levels. The epoxy die attach between silicon and copper is not included.

A key assumption is that the package system is stress-free at the 175°C epoxy cure temperature and that the major stresses are developed by thermal contraction of the materials around the die upon cooling to room temperature. This assumption is supported by Refs. 10 and 12. The material properties of the components are shown in Table 1. Values for Si and Cu are from standard references but the properties of the epoxy novolac are estimates from people familiar

Table 1—Assumed Material Properties

Material	PROPERTIES Young's Modulus (psi)	Poisson's Ration	Coefficient of Thermal Expansion (°C^{-1})
Si	2.73×10^7	0.355	2.7×10^{-6}
Cu	1.6×10^7	0.355	17.7×10^{-6}
Epoxy Molding Material	2×10^6*	0.31	26×10^{-6}, T < 150°C 63×10^{-6}, T > 150°C

* See text
Cool-down details: 175° C → 25°C

with this material. The elastic modulus of the epoxy is temperature-dependent;[12] however, reliable characterizations were not available when computations were performed. Consequently, a temperature-independent modulus was used for calculations. Perhaps more important is that slippage occurs between epoxy and the die or lead frame. Slippage between epoxy and the die surface has been demonstrated in Ref. 11, suggesting reducing the effective modulus for the nodal FEM model that does not permit slippage to occur. Slippage effects are taken into account by using a modulus of 2×10^4 psi. Computations based on values closer to those of Table 1 led to stress levels in excess of the fracture stress of silicon and predicted piezoresistivity effects much larger than those observed. The use of an effective modulus to account for slippage prevents a simple FEM comparison of various epoxies by merely inserting their published modulus values. Slippage between the die and lead frame may also affect stress levels. Experimentally, it was observed that piezoresistivity effects were not strongly dependent on the die attach or lead frame materials with the exception of eutectic die mounting. On the other hand, piezoresistivity effects were significantly reduced when the die was coated with a thick layer of elastomer prior to epoxy encapsulation. It was concluded that the chip/lead frame interface is of secondary importance in calculating stress levels.

The major FEM results are the centroid stresses in each silicon element. Table 2a shows orthogonal stresses S_x, S_y, and S_z parallel to long edge, short edge, and vertical directions, respectively. The corresponding shear stresses T_{zy}, T_{zx}, and T_{yx} are given in Table 2b. Equal stress contour maps for S_x, S_y, and T_{yx} are shown in Figs. 2a, 2b, and 2c. These maps were derived from a linear interpolation of the stress values of Table 2.

Compressive stresses parallel to die edges are the largest components in each element. Vertical stress is much smaller, and in the second row of elements from the die edges it is tensile (positive) rather than compressive. Epoxy does not adhere to the die surface so that tensile stress may be an artifact of the nodal (no slippage) limitation of FEM modeling. At the die center (and in most elements) S_x is larger than S_y. This is due to die aspect ratio rather than the fact that the long die edge is parallel to the long axis of the package. Fig. 2 shows that magnitudes of S_x are smallest along the y edge and increase toward the die center. Similarly, S_y is smallest along the x edge. The largest S_x and S_y values occur at the midpoint of the x and y edges, respectively. Shear stress in the surface plane, T_{yx}, maximizes at the corners and goes toward zero along the center lines of the die. These characteristics agree with equal stress contours experimentally derived in Ref. 15.

Table 2a—Orthogonal Stress (10^6 dynes/cm^2)

Die Corner

−1788 −1762 − 397	−1972 −1366 + 78	−2015 −1320 − 95	−2080 −1278 − 63	−2148 −1271 − 73	−2200 −1261 − 74	−2235 −1266 − 75	−2253 −1266 − 76
−1418 −1873 + 98	−1783 −1661 + 129	−1939 −1551 + 39	−2028 −1476 + 68	−2100 −1451 + 63	−2153 −1438 + 64	−2188 −1431 + 65	−2206 −1429 + 65
−1423 −1856 − 88	−1711 −1775 + 42	−1893 −1694 − 56	−2016 −1610 − 28	−2102 −1571 − 31	−2161 −1548 − 30	−2199 −1536 − 30	−2218 −1531 − 30
−1430 −1886 − 65	−1679 −1821 + 75	−1843 −1780 − 34	−1971 −1703 − 4	−2066 −1659 − 9	−2131 −1631 − 8	−2172 −1615 − 8	−2193 −1608 − 8
−1471 −1942 − 77	−1688 −1856 + 75	−1830 −1830 − 36	−1953 −1761 − 7	−2050 −1720 − 12	−2118 −1689 − 12	−2162 −1671 − 12	−2183 −1663 − 11
−1499 −1963 − 72	−1694 −1880 + 78	−1828 −1853 − 37	−1945 −1788 − 6	−2042 −1748 − 12	−2110 −1718 − 11	−2155 −1699 − 11	−2177 −1690 − 11

Die Center

KEY S_x / S_y / S_z

Table 2b—Shear Stress (10^6 dynes/cm^2)

Die Corner

+614 −647 +624	+221 −230 +512	+250 −163 +329	+239 −134 +235	+238 − 95 +167	+238 − 65 +112	+239 − 38 64	+239 − 12 + 2
+203 −235 +491	+ 2 + 7 +512	+ 19 + 13 +375	+ 20 − 4 +266	+ 21 − 2 +187	+ 21 − 2 +124	+ 21 − 2 + 71	+ 21 − 1 + 23
+121 −281 +284	− 16 − 6 +351	+ 5 + 5 +291	+ 4 − 14 +218	+ 6 − 9 +154	+ 7 − 8 +103	+ 6 − 4 + 59	+ 7 − 1 + 19
+100 −292 +175	+ 2 − 5 +216	+ 3 − 3 +195	+ 11 − 13 +155	+ 13 − 7 +113	+ 14 − 6 + 76	+ 14 − 3 + 43	+ 14 − 1 + 14
+ 69 −300 + 95	+ 2 − 5 +122	+ 7 − 4 +110	+ 5 − 16 + 91	+ 7 − 8 + 68	+ 7 − 6 + 47	+ 7 − 4 + 27	+ 7 − 1 + 9
+ 22 −302 + 27	+ 1 − 2 + 40	+ 2 − 4 + 35	+ 2 − 15 + 30	+ 2 − 8 + 22	+ 2 − 6 + 15	+ 2 − 4 + 9	− 2 − 1 + 3

Die Center

KEY T_{zy} / T_{zx} / T_{yx}

The calculated stress magnitude may not agree with actual conditions due to the somewhat arbitrary choice of temperature-independent elastic modulus for epoxy. However, the distribution shape and relative stress magnitudes are believed to be accurate. These factors

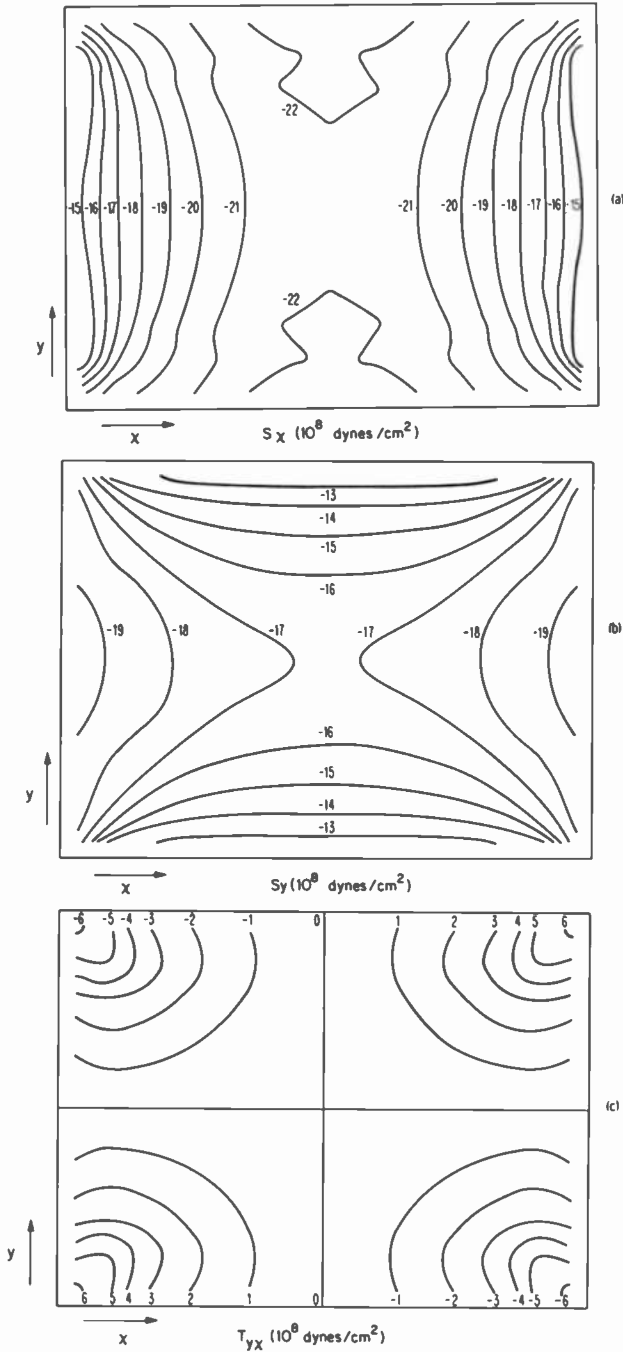

Fig. 2—(a) Equal-stress contour map for S_x parallel to the long die edge. (b) Equal-stress contour map for S_y stress parallel to the short die edge. (c) Equal-stress contour map for T_{yx} shear stress in the plane of the die.

control the location and orientation dependence of piezoresistivity effects on the silicon die.

3. Piezoresistivity

Piezoresistivity in silicon was first characterized by Smith.[16] When external stress is applied to silicon, its resistivity becomes anisotropic. Stress-induced resistivity change is dependent on the direction of current flow with respect to the crystal lattice. The three-dimensional effects of piezoresistivity are described by six fractional resistivity changes. These changes are related to stress through a 6×6 matrix of coupling coefficients. Due to symmetry of the silicon crystal lattice, only three of the possible 36 coefficients are independent and are commonly denoted as Π_{11}, Π_{12}, and Π_{44}. The remaining coefficients can be derived from these three. The fundamental coefficients have been experimentally determined; they are dependent on carrier type (n or p), temperature, and doping density. The doping density of diffused resistors is nonuniform; however, effective coefficients that depend primarily on surface concentration can be used.[17,18] In this paper, coefficients for p-type resistors are assumed to be 3, −1, and 90 in units of 10^{-12} $cm^2/dyne$ for Π_{11}, Π_{12} and Π_{44}, respectively. These numbers are based on a discussion of observed values given by Clark and Wise.[6]

The coupling coefficient matrix is dependent on the choice of coordinate system with respect to the silicon lattice. The basic coupling matrix occurs when x, y, z directions are parallel to the cubic axes of the crystal. This situation is pictured in Fig. 3a where x and y axes of a silicon die are parallel to the [010] and [001] directions in the plane of the (100) silicon surface. The x, y, z axes correspond to the FEM calculation. For this condition, the piezoresistivity coupling matrix is

$$\begin{vmatrix}\Delta_{xx}\\ \Delta_{yy}\\ \Delta_{zz}\\ \Delta_{zy}\\ \Delta_{zx}\\ \Delta_{yx}\end{vmatrix} = \begin{vmatrix}\Pi_{11} & \Pi_{12} & \Pi_{12} & 0 & 0 & 0\\ \Pi_{12} & \Pi_{11} & \Pi_{12} & 0 & 0 & 0\\ \Pi_{22} & \Pi_{12} & \Pi_{11} & 0 & 0 & 0\\ 0 & 0 & 0 & \Pi_{44} & 0 & 0\\ 0 & 0 & 0 & 0 & \Pi_{44} & 0\\ 0 & 0 & 0 & 0 & 0 & \Pi_{44}\end{vmatrix} \times \begin{vmatrix}S_x\\ S_y\\ S_z\\ T_{zy}\\ T_{zx}\\ Y_{yx}\end{vmatrix}. \quad [1]$$

Values of Δ are fractional resistivity changes and S and T are normal and shear stresses in $dynes/cm^2$. Subscripts of Δ refer to directions of resistivity change and current. For example, Δ_{yx} is the stress-induced resistivity change in the y direction due to current flow in the x direction. The formulism of piezoresistivity is based on electric field changes in response to stress under constant current density condi-

tions. Therefore, Δ_{yx} is a result of a stress-induced change in the y component of electric field due to the x component of current density. Symmetry of the silicon lattice results in the converse conditions; i.e., $\Delta_{yx} = \Delta_{xy}$, $\Delta_{zx} = \Delta_{xz}$, and $\Delta_{zy} = \Delta_{yz}$. For IC resistors, current is constrained to flow in the direction of resistor length. The electric field that determines potential drop across the resistor is parallel to current flow. Therefore, the fractional resistivity changes of interest are Δ_{xx} and Δ_{yy} which affect resistors parallel to the x and y directions. Resistivity change can be equated to resistance change if the resistor is sufficiently small so that stress is constant along its length. For the condition of Fig. 3a, the fractional resistance changes can be computed from [1] as:

$$\Delta_{xx} = \Delta R_x/R_x = (3S_x - S_y - S_z) \times 10^{-12}. \quad [2]$$

$$\Delta_{yy} = \Delta R_y/R_y = (-S_x + 3S_y - S_z) \times 10^{-12} \quad [3]$$

The fundamental coefficient values given above are used in Eqs. [2] and [3].

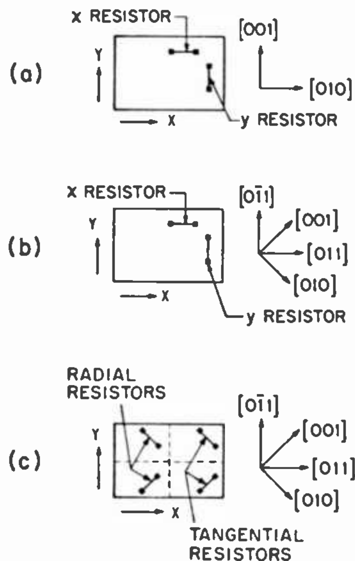

Fig. 3—Die and resistor orientations on a (100) silicon wafer: (a) edges and resistors in [100] type directions for minimum piezoresistivity effects, (b) conventional orientation with edges and resistors in [110] type directions which maximizes piezoresistivity effects, (c) edges in [110] directions and resistors in [100] directions for minimum piezoresistivity effects.

IC fabrication on (100) wafers usually employs die edges and resistor elements parallel to [011]-type directions as shown in Fig. 3b. This orientation results in die edges that are parallel to natural cleavage lines of the wafer but are rotated by 45° from the cubic axes in the wafer plane. Phann and Thurston[19] have derived expressions for piezoresistivity coupling coefficients in any coordinate system as a function of the fundamental coefficients and the direction cosines relating the coordinate system to the cubic axes. The coupling matrix for Fig. 3b is

$$\begin{vmatrix} \tfrac{1}{2}(\Pi_{11}+\Pi_{12}+\Pi_{44}) & \tfrac{1}{2}(\Pi_{11}+\Pi_{12}-\Pi_{44}) & \Pi_{12} & 0 & 0 & 0 \\ \tfrac{1}{2}(\Pi_{11}+\Pi_{12}+\Pi_{44}) & \tfrac{1}{2}(\Pi_{11}+\Pi_{12}+\Pi_{44}) & \Pi_{12} & 0 & 0 & 0 \\ \Pi_{12} & \Pi_{12} & \Pi_{11} & 0 & 0 & 0 \\ 0 & 0 & 0 & \Pi_{44} & 0 & 0 \\ 0 & 0 & 0 & 0 & \Pi_{44} & 0 \\ 0 & 0 & 0 & 0 & 0 & (\Pi_{11}-\Pi_{12}) \end{vmatrix} . \qquad [4]$$

The fractional resistance changes for the orientation of Fig. 3(b) are

$$\Delta_{xx} = \Delta R_x/R_x = (46S_x - 44S_y - S_z) \times 10^{-12} \qquad [5]$$

$$\Delta_{yy} = \Delta R_y/R_y = (-44S_x + 46S_y - S_z) \times 10^{-12} \qquad [6]$$

The coefficients multiplying S_x and S_y are more than an order of magnitude larger compared to Eqs. [2] and [3] because they depend on the larger shear coupling coefficient Π_{44}. Since S_x and S_y are the largest encapsulation stresses, piezoresistivity effects are large for the conventional (100) orientation. Note that neither of the orientations discussed above involve shear stress.

Piezoresistivity effects can be reduced by using standard die edge orientation and resistors tilted at 45° as shown in Fig. 3c. Resistors lie along cubic axes, and so coupling matrix Eq. [1] can be used. However, the stress components must be expressed in a coordinate system rotated 45° about the z axis. The stress components in this system are a function of FEM stress components and the direction cosines relating the rotated coordinate system to the x, y, z direction.[19] In terms of FEM stresses the fractional resistivity changes are:

$$\Delta R/R_{45} = \tfrac{1}{2}(\Pi_{11} + \Pi_{12})(S_x + S_y) + \Pi_{12}S_z \pm (\Pi_{11} - \Pi_{12})T_{yx} \qquad [7]$$

and

$$\Delta R/R_{45} = (S_x + S_y - S_z \pm 4T_{yx}) \times 10^{-12} \qquad [8]$$

The + and − signs for T_{yx} are for tangential and radial resistors, respectively, as defined in Fig. 3c.

Fractional resistance changes were calculated with the FEM stress values of Table 2. For resistors parallel to cubic directions, as in Figs. 3a and c, the changes are relatively small and always negative. The maximum and minimum resistivity changes for Fig. 3a occur at the midpoint of the long edge where $\Delta R_x/R_x = -0.55\%$ and $\Delta R_y/R_y = -0.15\%$. Therefore, the largest stress-induced resistor ratio error among any set of resistors is 0.40% independent of their location or orientation. This number is halved if all resistors are in the same direction. Stress-induced mismatch is insignificant for closely spaced parallel resistors. Variations of resistor width, doping density, and contact resistance are more significant factors in ratio errors. A similar situation applies to the 45° tilted resistors of Fig. 3c. In this case the largest shifts occur at die corners where radial and tangential resistors change by −0.60% and −0.11%, respectively.

Effects are much larger for the standard orientation, Fig. 3b. Change in x resistors can be from −4.79% to 1.78% depending on location. The range for y resistors is − 2.46% to 4.09%. Fig. 4 shows maps of equal shift contours for x resistors (a) and y resistors (b). These maps were derived by interpolation between calculated values at the center of each element. Results from the upper left quadrant were mirrored into the other three quadrants.

Although encapsulation shifts are large for the standard orientation, resistor matching can be preserved by careful design. At most locations shifts are opposite in polarity for x and y resistors. A pair of resistors that are not entirely parallel (e.g., one is folded and has both x and y segments) will become mismatched after encapsulation even if they are in close proximity and located near the die center. Note that equal shift contour gradients increase near the die edges. A set of parallel x resistors placed near the x edge will become mismatched because the resistor nearest the edge will shift more than the others. The same is true of y resistors near the y edge. Suggestions for avoiding stress-induced mismatch for this orientation are:

(1) Matched resistors should be parallel and in close proximity. If they must be folded due to space limitations, they should be divided into a series of metal-connected resistors all of which are parallel and in close proximity.
(2) Matched resistors should be placed as close to the die center as possible.
(3) If matched resistors must be placed close to an edge, they should be perpendicular to it. This applies only if the resistors have nearly equal lengths.
(4) Corners should be avoided.

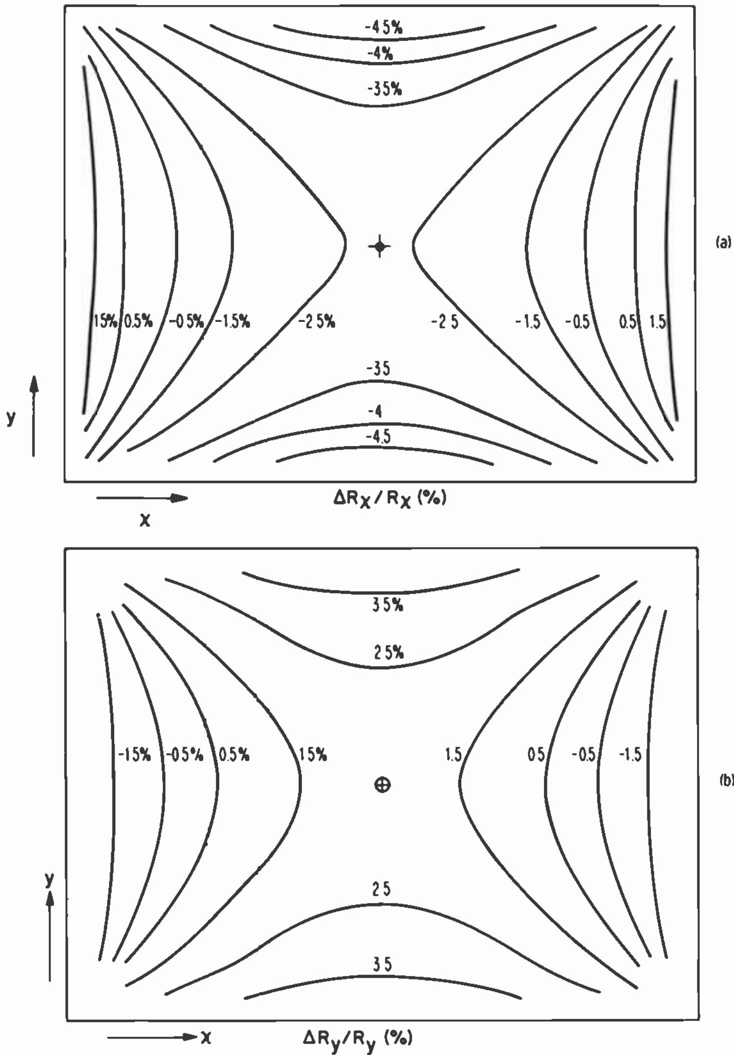

Fig. 4—(a) Contour map for package stress-induced shifts of *x* resistors for conventional (100) die orientation (see Fig. 3b). (b) Contour map for package stress-induced shifts of *y* resistors for conventional (100) die orientation (see Fig. 3b).

These suggestions should be adequate for eliminating piezoresistive encapsulation effects on many circuits using the conventional orientation. However, they may result in wasted die area or become impossible if a large number of resistors must be matched, as in a D/A resistor ladder network.

When die edges and resistors are parallel to cubic axes (Fig. 3a), stress-induced mismatch is virtually eliminated. This orientation does not require special rules and it can be used with existing designs that are affected by peizoresistivity. It can be accomplished by a simple 45° rotation of a standard (100) substrate with respect to photomasks or by using (100) substrates with a properly positioned flat. Care must be taken at the die separation process. Wafer sawing must be used rather than the conventional "scribe and break" method.

4. Application

Piezoresistivity analysis was applied to a Chroma/Luma IC designed for use in television receivers.[21] This IC decodes chrominance information from the baseband signal and combines it with luminance information to produce red, green, and blue (RGB) output signals. These signals control brightness and color information viewed on the television screen.

The dc offset voltages among RGB outputs are critical parameters for proper receiver performance. Ideally, there should be no offset, but this is rarely achieved due to IC process tolerances and the complex circuitry used to generate the outputs. Therefore offsets are nulled by external potentiometers during manufacture of the receiver. After adjustment, offset stability becomes extremely important. Offset drifts of 30 mV can be discerned by a critical observer and drifts greater than 90 mV can be detected as a colored background by many TV viewers. In its initial form many Chroma/Luma ICs exhibited excessive drift during reliability tests and simulated receiver operation. Offset drifts were found to be a result of piezoresistivity and package stress instability.

RGB outputs are produced by three separate but identical circuits that contain several matched resistor pairs. Resistors must be placed at different die locations so that stress instability will affect each resistor and the corresponding output in a different manner, thereby resulting in offset drift.

Fig. 5 is a schematic of the dc coupled output circuitry. Each color output incorporates a matrix amplifier, level shifter, luminance summer, and blank/buffer stage. The latter provides low output impedance as well as blanking during horizontal, vertical retrace. Inputs to the matrix amplifiers are derived from the in-phase (I) and quadrature (Q) components of the demodulated chrominance signal. Appropriate fractional values of I and Q are combined in the matrix amplifiers to regenerate $R - Y$, $G - Y$ and $B - Y$ color difference signals. The luminance (brightness) signal, Y, is added in the luminance summers.

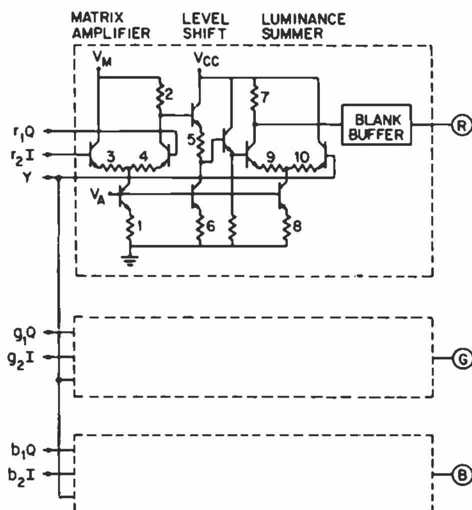

Fig. 5—Schematic of the dc coupled circuit for color output signals used in the Chroma/Luma IC. Circuitry for green and blue outputs is identical to that shown for the red output.

DC offsets are measured when there is no chrominance signal. Inputs to the matrix amplifiers are at near equal dc levels determined by the quiescent state of the driving circuitry. The luminance input is at a dc level determined by the black level reference signal and the customer brightness control. During testing, the brightness control is typically set to give 4 V (nominal) at the RGB outputs. These conditions were used in a sensitivity analysis to determine the effects of each resistor on output in millivolts of output change per 1% resistance change. Resistors with more than 20-mV/% sensitivity are labeled with numbers in Fig. 5. There are five pairs of resistors having approximately equal but opposite polarity sensitivity. For example, +1% change in resistors 1 and 2 causes +52 mV and −52 mV output changes, respectively, thereby canceling their effects.

Fig. 6 shows the approximate layout of critical resistors on a background grid representing elements used in the FEM stress calculation. Resistors are labeled with a number and letter referring to the schematic diagram and color, respectively. The piezoresistive change for each resistor was calculated with Eqs. [5] and [6] (standard (100) orientation) and the stress values at its location. Resistors that spanned more than one element and/or had legs in both the x and y directions were divided into sections. Resistance change in each section was calculated individually and then added to determine total resistance change. Interpolated stress values were used for sections that lay near

grid lines. The net effect on outputs is the algebraic sum of products (% change) × (sensitivity) for resistors in each color circuit. The calculated shifts from 4 V are 139, −74, and −135 mV for R, G, and B, respectively. In the actual circuit the B output is chopper-stabilized to the brightness control voltage. This is accomplished by adjusting the dc value of the *Y* signal during the black level reference portion of the horizontal retrace period. As a result, the shift of one color cannot be detected; only offset between colors can be measured. The calculation predicts offset shifts of B−R = −274 mV, B−G = −61 mV, and R−G = 213 mV.

Piezoresistive shifts are due to both orientation and location of various resistors. For example, the predominantly *x* and *y* orientations of 7R and 8R, respectively, contribute +214-mV shift to the R output. The separation of resistors 1R, 1G, and 1B from their matching components 2R, 2G, and 2B contributes −86 mV to the R output and −112 mV to the G and B outputs. Encapsulation-induced offsets can also be considered as a result of mismatch between corresponding resistors in each color. For example, the large B−R and R−G offsets are mostly due to the predominately *x* orientation of 7R compared to the predominately *y* orientation of 7B and 7G.

During the course of investigation, the following effects were observed:

(1) Offsets measured at wafer probe are significantly shifted by encapsulation, 200 to 500 mV typically.

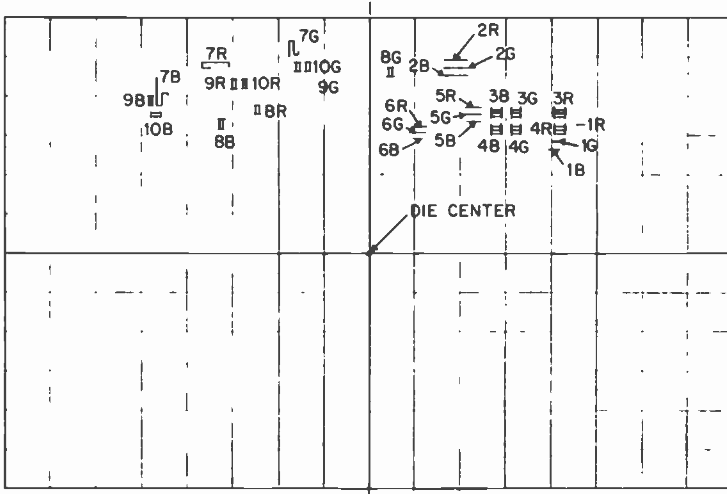

Fig. 6—Initial layout of critical resistors used in the color output circuit.

(2) Simultaneously molded devices have differing amounts of encapsulation shift indicating nonreproducible stress levels or distributions.
(3) Thermal cycling changes offsets, but pressure cooker and bias life tests have little effect.
(4) The amount of thermal-cycle-induced drift varies widely among devices, but the overall tendency is to change offsets toward wafer probe values suggesting stress relaxation.
(5) Offsets can be reversibly changed by application of C-clamp pressure on the long axis of the package.

Thermal cycling (−60 to 150°C) and C-clamp pressure were found to be valuable tests for detecting instabilities related to encapsulation stress and the piezoresistivity effect.

Two approaches were taken to minimize encapsulation offset shifts and the subsequent offset drifts. The first was to rotate the (100) substrate by 45° with respect to photomasks to make resistors and die edges parallel to cubic axes. The second was to redesign critical resistor layout and use standard (100) orientation. For this approach all resistors were oriented in the x direction and placed in the third row of elements from the long die edge. Both methods reduced encapsulation shift and eliminated the offset drift problem.

Table 3 summarizes data for encapsulation, thermal cycle, and C-clamp tests. Encapsulation shift is given in Table 3a. The data represent the difference between the average offsets in plastic packages and the average offsets in ceramic packages. It is assumed that devices in ceramic packages are relatively stress-free. Offset shift is significantly reduced by the 45° substrate rotation and the redesign methods. The calculated offsets for the original configuration are included in Table 3a. They are smaller than experimental results but agree in polarity and relative magnitude. It is believed that the major discrepancy is because FEM stress values are too small. An underestimation of Π_{11} and Π_{44} coupling coefficients and the nodal limitations of the FEM calculation may also contribute errors. It should be noted that offsets have a wide distribution approaching the magnitude of average shifts. In light of this fact, the agreement between calculated and average shift is quite good.

Thermal cycle stability in plastic packages is shown in Table 3b. Offsets were measured before and after 20 thermal cycles for each device in the test. The data in this part of the Table represent the average of offset drifts. After 20 thermal cycles, all original circuits had at least one offset drift larger than 30 mV and most had a drift larger than 90 mV. None of the improved circuits failed the 30-mV criteria up to 80 thermal cycles.

Table 3—Summary of Test Data

(a) Encapsulation Stability: Shift from average ceramic offsets to average plastic offsets (mV)

	B-R	*B-G*	*R-G*
Original (Calculated)	−274	− 61	213
Original	−520	−172	343
Original 45°	94	59	− 35
Redesign	− 10	− 5	15

(b) Thermal Cycle Stability: Average offset change after 20 thermal cycles (mV)

	B-R	*B-G*	*R-G*
Original	142	81	− 63
Original 45°	− 2	− 8	− 10
Redesign	1	−11	− 10

(c) C-Clamp Pressure Stability, Typical (mV)

	B-R	*B-G*	*R-G*
Original	−667	−289	378
Original 45°	19	6	− 13
Redesign	10	− 7	− 17

C-clamp pressure stability is shown in Table 3c. The data represent typical offset changes induced by the uncalibrated hand of an enthusiastic assistant. The large difference between original and improved devices does not warrant a sophisticated pressure application system.

5. Conclusion

Plastic encapsulation results in large compressive stress on an integrated circuit. Encapsulation stress can affect electrical parameters via the piezoresistivity effect. Bipolar/linear circuits make extensive use of precise resistor ratio matching and therefore can be sensitive to stress. Resistor ladder networks used in A/D and D/A converters are also subject to stress effects. Piezoresistivity effects are most significant when precise dc gains and attenuations must be achieved by resistor matching.

Encapsulation stress is not constant; it changes as a function of time and ambient conditions. This can result in drift or instability of electrical parameters. Encapsulation stress is not uniform from one package to another even if they are simultaneously molded. Attempts to compensate for stress effects by circuit design are often unsuccessful.

The stress distribution on silicon die was calculated by the Finite Element Method. The largest stresses are compressive and parallel to die edges. Vertical and shear stresses are relatively small. FEM stress values were used to determine piezoresistivity effects on p-type resistors formed on a (100) silicon substrate. It was shown that the conven-

tional (100) substrate orientation is highly sensitive to stress because resistors are parallel to [110] type directions. A 45° rotation of substrate with respect to photomasks results in resistors parallel to [100] type directions. These resistors are much less sensitive to stress.

Piezoresistivity analysis was applied to the Chroma/Luma IC. The original layout design on a standard (100) substrate resulted in encapsulation-induced change and instability of the RGB color output voltages. Instabilities were eliminated after a careful redesign of critical resistor layout. Fabrication of the original design on a 45° rotated substrate also eliminated instabilities.

Thermal cycling and C-clamp pressure applied to the long axis of the package are valuable tests for detecting piezoresistive effects.

Acknowledgments

The authors are indebted to J. Hettiger for suggesting the C-clamp pressure test, to J. Armer and E. Wittman for measurements of Chroma/Luma circuits, to J. Sosniak for sensitivity analysis, to J. McCarty for manuscript preparation, and especially to J. Carnes for direction at the beginning of the project and R. Dawson for continuing encouragement.

References

[1] W. P. Mason and R. N. Thurston, "Use of Piezoresistive Materials in the Measurement of Displacement, Force and Torque," *J. Acoust. Soc. Am.*, **29**, p. 1096 (1957).

[2] O. N. Tugt and D. Long, "Recent Developments in Semiconductor Piezoresistive Devices," *Solid-State Electronics*, **6**, p. 323 (1963).

[3] D. E. Fulkerson, "A Silicon Integrated Circuit Force Sensor," *IEEE Trans. Electron Devices*, **ED-16**, p. 867 (1969).

[4] E. R. Peake, A. R. Zias, and J. V. Egan, "Solid-State Digital Pressure Transducer," *IEEE Trans. Electron Devices*, **ED-16**, p. 870 (1969).

[5] Kulite Semiconductor Products, Inc., Ridgefield, NJ.

[6] S. K. Clark and K. D. Wise, "Pressure Sensitivity in Anisotropically Etched Thin-Diaphram Pressure Sensors," *IEEE Trans. Electron Devices*, **ED-26**, p. 1887 (1979).

[7] W. H. Ko, J. Hynecek, and S. F. Boettcher, "Development of a Miniature Pressure Transducer for Biomedical Applications," *IEEE Trans. Electron Devices*, **ED-26**, p. 1896 (1979).

[8] J. M. Borky and K. D. Wise, "Integrated Signal Conditioning for Silicon Pressure Sensors," *IEEE Trans. Electron Devices*, **ED-26**, p. 1906 (1979).

[9] L. M. Roylance and J. B. Angell, "A Batch-Fabricated Silicon Accelerometer," *IEEE Trans. Electron Devices*, **ED-26**, p. 1911 (1979).

[10] H. Inayoshi, K. Nishi, S. Okikawa, and Y. Wakashima, "Moisture-Induced Corrosion and Stress on the Chip in Plastic-Encapsulated LSIs," *IEEE Proc. Reliability Physics Symposium*, **17**, p. 113 (1979).

[11] M. Isagawa, Y. Iwasaki, and T. Sutoh, "Deformation of Al Metalization in Plastic Encapsulated Semiconductor Devices Caused by Thermal Shock," *IEEE Proc. Reliability Physics Symposium*, **18**, p. 171 (1980).

[12] R. J. Usell, Jr. and S. A. Smiley, "Experimental and Mathematical Determination of Mechanical Strains Within Plastic IC Packages and Their Effect on Devices During Environmental Tests," *IEEE Proc. Reliability Physics Symposium*, **19**, p. 65 (1981).

[13] J. L. Spencer, W. H. Schroen, G. A. Bednarz, J. A. Bryan, T. D. Metzgar, R. D. Cleveland, and D. R. Edwards, "New Quantitative Measurements of IC Stress

Introduced by Plastic Packages," *IEEE Proc. Reliability Physics Symposium*, **19**, p. 74 (1981).
[14] W. H. Schroen, J. L. Spencer, J. A. Brian, R. D. Cleveland, T. D. Metzgar, and D. R. Edwards, "Reliability Tests and Stress on Plastic Integrated Circuits," *IEEE Proc. Reliability Physics Symposium*, **19**, p. 81 (1981).
[15] S. Komatsu, K. Suzuki, N. Iida, T. Aoki, T. Ito, and H. Sawazaki, "Stress-Insensitive Diffused Resistor Network for a High Accuracy Monolithic D/A Converter," IEDM Technical Digest, 1980 International Electron Devices Meeting, p. 144 (1980).
[16] C. S. Smith, "Piezoresistance Effect in Germanium and Silicon," *Physical Review*, **94**, p. 42 (1954).
[17] O. N. Tufte and E. L. Stezer, "Piezoresistive Properties of Silicon Diffused Layers," *J. Applied Phys.*, **34**, p. 313 (1963).
[18] D. R. Kerr and A. G. Milnes, "Piezoresistance of Diffused Layers in Cubic Semiconductors," *J. Applied Phys.*, **34**, p. 727 (1963).
[19] W. G. Pfann and R. N. Thurston, "Semiconducting Stress Transducers Utilizing the Transverse and Shear Piezoresistive Effects," *J. Applied Phys.*, **32**, p. 2008 (1961).
[20] A. E. H. Love, *A Treatise on the Mathematical Theory of Elasticity*, Dover Publications, New York, 4th Ed., p. 80 (1944).
[21] L. A. Harwood, E. J. Wittmann, J. Hettiger, and R. L. Shanley, "Integrated NTSC Chrominance/Luminance Processor," *IEEE Trans. Consumer Electronics*, **CE-26**, p. 693 (1980).

Proximity Printing of Chrome Masks

Dietrich Meyerhofer
RCA Laboratories, Princeton, NJ 08540

Joe Mitchell
Solid State Division, Somerville, NJ 08876

Abstract—We have investigated the application of proximity printing to the copying of chrome masks used in the fabrication of integrated circuits. The images were produced on chrome blanks coated with various positive and negative photoresists. Employing a test mask with lines and spaces of varying size, we studied the printing process as a function of separation between master and print. When plotting the difference in width between etched lines on the print and the corresponding feature on the mask as a function of the separation, one observes fluctuations due to the movement of the diffraction peaks in the optical image. For the negative resist, the average difference in width is approximately constant to separations of 25 μm, while for positive resists it changes monotonically with increasing gap spacing. We have compared the measured results with calculations using a model of the resist exposure and development. Measured values of resist parameters are used in the model which produces good agreement with experiment. Calculated details of the resist profiles are compared with SEM photographs of the developed resist layer.

These investigations show that, with a proximity gap of 12 μm, long lines and spaces can be well reproduced if they are 3 μm or wider. The situation is less satisfactory for small squares and rectangles where the corners become rounded before the sides change position. Good images of squares are limited to dimensions 5–10 μm and larger. Images in negative resist are less sensitive to the size of the proximity gap than those in positive resist. We conclude that proximity printing would be difficult to apply to mask replication, but that it has considerable promise for replicating 10× step-and-repeat reticles.

1. Introduction

At the present time, copying of chrome masks is done by contact-printing. This limits the number of prints that can be produced from a master because each contact printing step is likely to produce defects in the mask. It is, therefore, desirable to have a noncontact technique for duplicating masks. One of the simplest such techniques is proximity printing, where the photosensitive surface is separated by a few mi-

crometers from the master object. This imaging process is essentially a shadowing process, complicated by the diffraction of light at the edges of the patterns. The only optics required is a system to produce a large uniform-intensity beam of appropriate collimation.

This paper explores the application of proximity printing to the replication of chrome masks. A large collimated beam from a pulsed xenon light source was used for illumination. The degree of collimation and the spectral distribution could be varied to a limited extent. The shape and quality of the resulting images were investigated as a function of the object-to-image spacing. Simple test patterns were used to facilitate the analysis. They consist of lines and spaces of 1 to 10 μm dimensions, and of squares and corners of similar sizes.

Four different photoresists were compared for the quality of the images that can be produced. As shown in Table 1, they differ markedly in their spectral responses. ADNR II is a negative resist developed at RCA. It is a combination of an azid type sensitizer and a Novalak resin and is sensitive only in the deep UV (260 nm). In contrast to other negative resists, it can produce images of very high resolution, similar to positive resists. Of the positive resists, AZ-2400[1] is a diazoquinone-resin combination similar to AZ-1470 or HPR-204. It is sensitive in both the near and deep UV, with the near UV sensitivity dominating. PMMA[2] and PBS[3] are sensitive only in the deep UV at 230 and 185 nm, respectively. PBS has not been used much as a photoresist because of the difficulty of operating in this wavelength region. However, we expect the magnitude of the diffraction effects to decrease with decreasing wavelength, and be at a minimum for PBS resist.

The large number of parameters involved in these experiments makes it impossible to investigate all the variations experimentally. Therefore, we have studied analytic models of the experiment using the computer program SAMPLE,[4] which we adapted for this purpose. The model is verified by comparing the calculated resist profiles with experimental observations. It can then be used to determine suitable operating conditions.

Table 1—Photoresist Blanks Used for Printing

	AZ-2400	ADNR II	PMMA	PBS
Resist Thickness (μm)	1.0	0.7	0.5	0.4
Soft Bake (minutes)	20 at 90°C	20 at 75°C		60 at 120°C
Relative Exposure	1	0.5	20	8
Development Time (sec)	60	100	90	70
Developer	AZ-2401:H_2O (1:4)	AZ-Devel. (Full Str.)	MIBK	MIAK:H_2O

2. Experiment

2.1 Sample Preparation

The test samples were prepared from Cr-coated photomask blanks whose flatness was determined by a Tropel Flatness Analyzer to be within ≤ 2 μm. The plates selected were covered with the resist to be evaluated in the usual manner by spin coating to the required thickness (Table 1). The samples were softbaked for the appropriate time and at the temperature recommended for each resist.

2.2 Exposure and Development

The samples were exposed with our pulsed Xe exposure system (Fig. 1).[5] A 4-mm source was used, which can be considered to be a point source for purposes of this experiment. The light falling on the object is approximately coherent. The pulsed xenon source has a thermal emission spectrum (Fig. 2). As long as the current density and, therefore, the temperature are high enough, the lamp emits very efficiently in the deep UV.

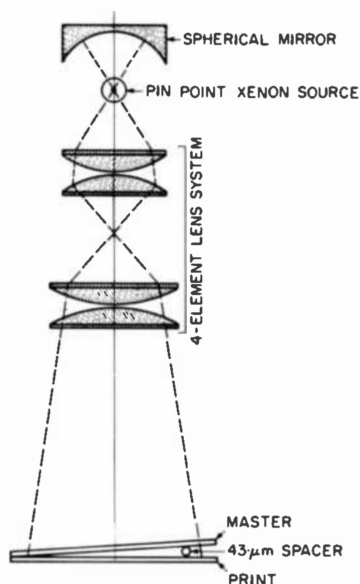

Fig. 1—Schematic diagram of pulsed xenon exposure system for copying chrome masks. The master and print are shown in the test configuration in which the proximity gap changes in a linear manner from one side of the image to the other.

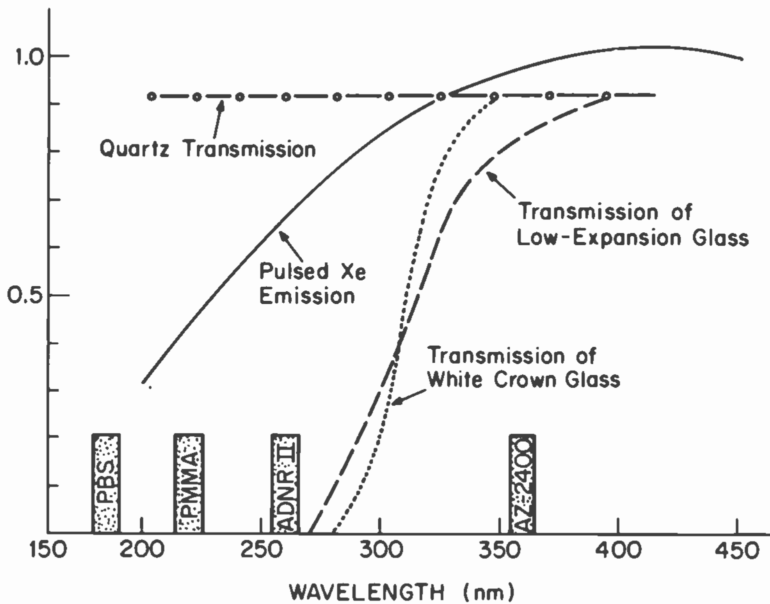

Fig. 2—Spectral dependence of the transmission of various substrates and of the output of the pulsed xenon source. The wavelength regions in which the resists used have their peak sensitivity are shown shaded. The output of the xenon source is plotted in arbitrary units for a current density of 3000 Å/cm^2.

The master object used in these tests is a chrome-on-quartz mask composed of an array of "BTL test patterns," which consist of a variety of simple features of various dimensions. The substrate was flat to better than 1 μm and transparent to wavelengths as short as 170 nm.

To obtain as much information as possible, the out-of-contact exposure configuration used a wedge-shaped arrangement of object and image plates. The two plates touched at one edge and were separated by 43 μm at the other edge by a wire of that diameter. This caused the proximity gap to vary linearly along a row of patterns on the master. The position of each pattern was determined from the numerical pattern information used in writing the master. With this information, the gap spacing of each pattern was calculated.

Exposure tests were made to determine an appropriate exposure for each material. Table 1 lists the exposure requirements for each resist evaluated, relative to AZ-2400. For example, PMMA required 20 times the number of flashes that AZ-2400 required, while ADNR-II needed only half the number. The PBS plates were exposed in a N_2 atmosphere to eliminate the filtering effects of ozone on the exposing deep-UV radiation to which PBS is sensitive.

Beaker development was used for AZ-2400, ADNR-II, and PMMA. The PBS samples were spin-developed and postbaked. After etching, all samples were stripped in Shipley AZ-1112, except PMMA which was stripped in Allied Stripper No. 4 with HNO_3 added.

2.3 Analysis of Results

The width of the resist lines was measured with an ITP electronic measuring system. The features investigated were groups of lines and spaces of 4, 6, and 10 μm width and single lines of 3 and 5 μm widths. The measured chrome features on the print were compared with the dimension of the corresponding feature on the master. The difference between the two, Δ, was recorded as a function of proximity gap.

In analyzing the linewidth changes it was observed that the light distribution of the xenon exposure source was not uniform. An intensity measurement with a flash integrator sensitive to 365-nm light showed 15% higher intensity at the center of the system than at the edges. The dependence on wavelength was studied by producing images in which the master and print plates were kept parallel at a uniform separation of 25 μm.

The radial changes in linewidth under these conditions are shown in Fig. 3. The vertical positions of the curves are arbitrary, since the

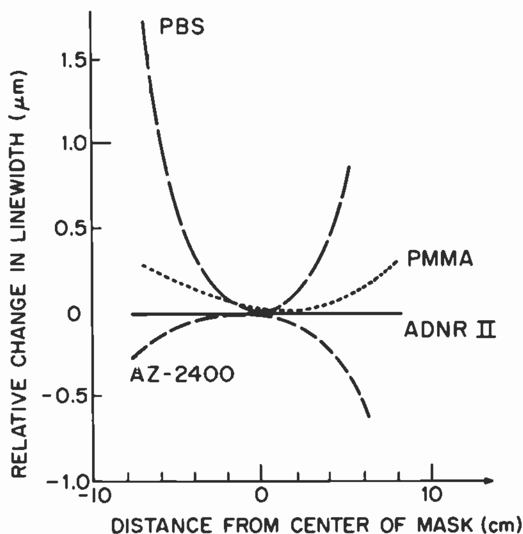

Fig. 3—Radial variation in linewidth on prints made with four different resists. A 5-μm space was chosen on the mask, and the width of the corresponding etched feature on the print was measured. The difference is plotted here, normalized to the center of the mask.

absolute linewidth depends on the processing. The curve for AZ-2400 which is predominantly sensitive in the 365-nm region shows the expected dependence on illumination intensity, with smaller spaces at the outside of the field. In contrast to this, PBS, which responds only at very short wavelengths, shows much larger spaces at the outside. This is because the exposing radiation is partly absorbed by the quartz lenses. The total thickness of quartz in the center of the condensing system is 6.5 cm. The lenses are made of Suprasil, which at this thickness absorbs 30–40% of 185-nm light. Near the outside of the field the absorption is small, leading to increased exposure compared to the center of the field. In the intermediate-wavelength region, the two effects balance each other, so that at 265 nm, where ADNR II is sensitive, the light distribution appears to be uniform.

The radial variations in light intensity can be reduced to zero at any given wavelength by adjusting the optical elements appropriately. In the present case, which is adjusted for ADNR II, the measured linewidth values of the other resists were corrected for the radial variation using the curves of Fig. 3.

To measure finer details of the process, SEM photographs were made of some of the resist patterns before the resist had been stripped. Generally, images formed at a separation distance of ≈ 13 μm were used for this work.

3. Modeling

The program SAMPLE was developed at the University of California to model exposure, bleaching, and development of photoresist films on various surfaces. Simple one-dimensional exposure patterns, namely, single lines, single spaces, and multiple lines and spaces, are used as objects. The exposure patterns and profiles are analyzed along a line at right angles to these features.

We have extended the SAMPLE program to generate images pro-

Table 2—Parameter Values Used in the Calculations

Resist	Wavelength nm	Index of Refraction	Absorption Coefficient μm^{-1}	Bleaching Parameter mJ/cm^2
ADNR II	260	1.80	4.2	0.027
AZ-2400	254	2.00	2.1	0.015
	280	1.86	5.1	0.015
	365	1.68	0.24	0.015
	405	1.65	0.33	0.015

Chrome: Index of refraction = 2.6 + 2.0i

duced by proximity printing. The magnitude of the proximity print gap is adjustable and various illumination conditions, from collimated to diffuse, can be simulated. The resist parameter values used in these calculations had been previously measured by us. The illumination and resist parameters used in the calculations are listed in Table 2.

An example of a calculated illumination pattern at the resist film is shown in Fig. 4. A 4-μm space on a mask separated by 10 μm from the resist is illuminated with parallel light. The figure shows only one-half of the symmetric pattern, i.e., the edge of the perfect image of the space would fall at $x = 2$ μm. It can be seen that diffraction causes the image to be significantly distorted and that the intensity at 2 μm is only about 20% of the incident light intensity. The illumination pattern is strongly dependent on the wavelength of the incident light, as the diffraction peaks change position with wavelength. However, at the edge of the ideal image, the curves almost coincide, contrary to expectation. Thus, we do not expect the developed line edge to show much change with wavelength.

After the image is calculated, SAMPLE determines the bleaching of the resist layer due to exposure. Because of absorption, the light intensity decreases with depth. It increases with time as bleaching takes place. These effects are combined to calculate the amount of

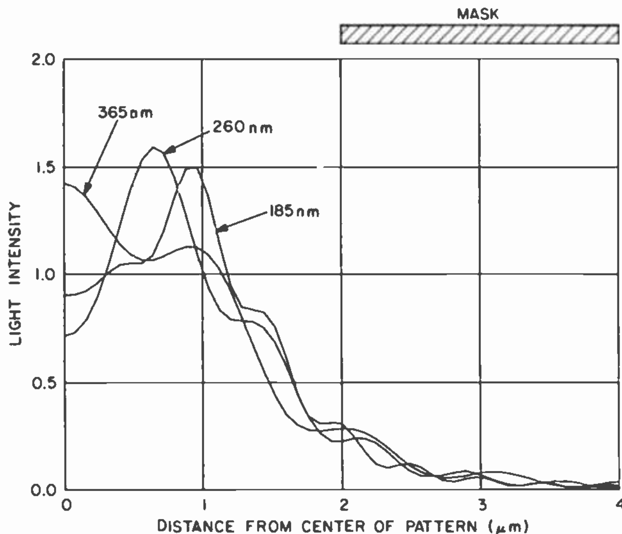

Fig. 4—Example of the calculated light distribution in the image plane for proximity printing. The incident light is collimated; the mask is a single slit of 4-μm width located 10 μm from the image plane. The curves are symmetric about $x = 0$. The light distribution is shown for the three different wavelengths indicated.

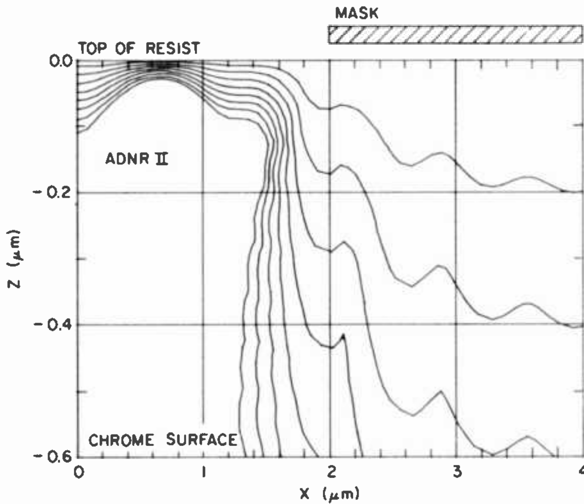

Fig. 5—Calculated development contours of a film of ADNR II exposed under the illumination conditions of Fig. 4. The mask is exposed with a dose of 10 mJ/cm^2 at a wavelength of 260 nm. The location of the slit on the mask is indicated schematically. The resist thickness is 0.6 μm. The profiles shown are calculated after equal intervals of development time.

bleaching at each point in the resist at the end of the exposure. This quantity determines the development rate at the corresponding points.

The developing process is modeled by calculating the resist profiles after various development times using a string model. The chrome etch process (wet or dry) is not included in the model program at this time, so we simply assume that etching only takes place in the areas where the resist has been removed completely.

An example of developed resist contours after illumination with the intensity patterns of Fig. 4 is shown in Fig. 5 for the negative photoresist ADNR II with 260-nm exposure and in Fig. 6 for the positive resist AZ-2400 with 365-nm exposure. The profiles are shown at 8 different development times. The values of the development times are only significant in relation to each other, since they may be changed by adjusting the strength of the developer without affecting the profiles appreciably.

The shapes of the edge profiles of the two resists are quite different. The negative resist produces a much steeper profile when the development has proceeded to the nominal pattern edge than does the positive resist. This is because the exposure decreases with depth. With a negative resist, this causes more rapid development at lower depths leading to a sharpening of the edge and eventual undercutting.

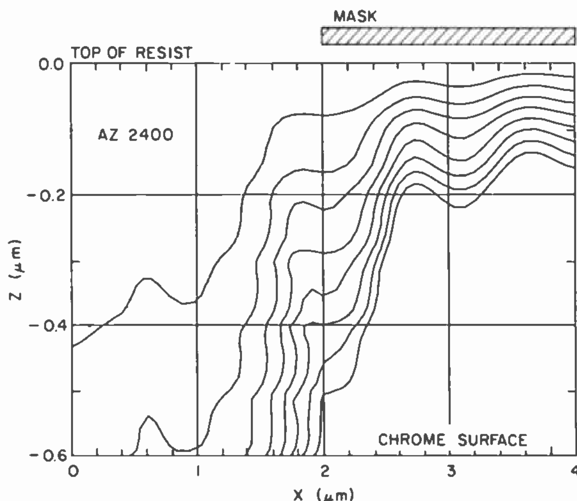

Fig. 6—Calculated development countours for a film of AZ-2400 under the same conditions as in Fig. 4. The exposure is 25 mJ/cm^2 at 365 nm.

This argument is valid here because, unlike conventional negative resists, ADNR II does not swell or distort in the developer.

The calculated image dimensions are obtained from development curves such as those of Figs. 5 and 6. We determined the error in linewidth as twice the difference, Δ, between the edge of the ideal image and that of the bottom of the profile at a specified development time.

4. Results

4.1 Linewidths on Negative Resist Plates

We first calculated the dependence of the widths of various lines and spaces on the gap spacing. We used the parameters of ADNR II from Table 2. The absorption characteristics of the resin and the spectral sensitivity of the sensitizer combine to produce a resist with a relatively narrow spectral response centered around 260 nm. Thus the exposure of ADNR II with a xenon lamp can be well approximated by a single-wavelength illumination of the mask, as was used in Fig. 5. For the modeling, the resist thickness is taken as 0.7 μm, the experimental value.

The calculated Δ for a space of 5-μm width is plotted as a function of proximity gap spacing in Fig. 7 (circles). A development time was chosen that caused the linewidth at a gap spacing of 10 μm to have the nominal value. Illumination by a pinpoint source was assumed. These calculated values show considerable fluctuations as the gap spacing

changes. The fluctuations are caused by the complicated optical image with its diffraction peaks and valleys (Fig. 4).

Fig. 7 also shows the corresponding measured values of Δ for ADNR II (crosses). The exposure was with the high-coherence small-area xenon source. There is a negative bias of about 0.5 μm caused by overdevelopment. The fluctuations due to interference peaks are evident. They are less pronounced than the calculations predict, but show the same general trend. This probably means that the light source is less coherent than the calculations assumed. This explanation was tested by calculating Δ for the case of a large area light source. We assumed that the incident light at the master formed a cone with a half angle of 0.025 radian. Using the same exposure dose and development time, we observed that the Δ values for this light source were similar to those of the coherent source (Fig. 7), but that the amplitude of the fluctuations was indeed reduced by at least a factor of two.

When the fluctuations in the experimental data are averaged out, the dimension of the imaged feature remains independent of gap spacing to about 25 μm, an important practical consideration. In contrast to this, the average calculated values increase with gap spacing over the entire range.

To faithfully print a complicated IC pattern, Δ must be the same for features of all sizes. To determine whether this is possible with a

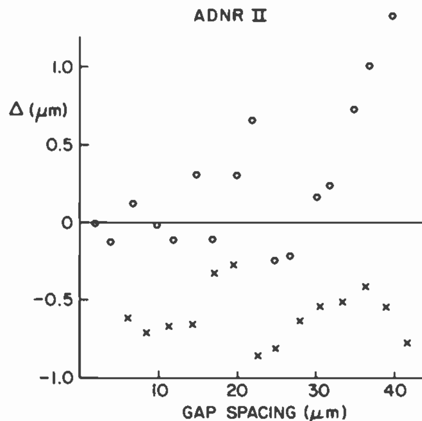

Fig. 7—Difference, Δ, between the width of the developed resist line and the width of the corresponding space on the mask for negative resist ADNR II as a function of the proximity gap. The object is a 5-μm wide space in an opaque background. The experimental points are shown by the crosses, the calculated ones by the circles. For both cases the wavelength of the light is 260 nm and the dose is 5.6 mJ/cm^2. The resist thickness is 0.7 μm. For the calculation the development time is adjusted to produce the nominal line width at a gap of 10 μm.

proximity imaging system, we calculated Δ for spaces of 3, 4, 5, and 6 μm; for a single 4-μm line; and for a grating of 4-μm lines and spaces. Identical exposure and development parameters were used for all cases. The results show that, for gap values from 4 to 15 μm, Δ is constant and the same for all these features.

4.2 Linewidths on Positive Resist Plates

The positive resist AZ-2400 was modeled in the same way as the negative resist. The parameters were taken from Table 2. We simulated the effect of the broadband xenon source on this resist by constructing the illuminating light out of the four wavelenths at which the resist sensitivity is greatest: 254, 280, 365, and 405 nm. The resist film was taken to be 0.6 μm thick as in the experiment.

The results for a 5-μm space are plotted in Fig. 8 (circles). In this case Δ is the difference between the opening in the resist and the width of the space at the object mask. The size of the opening decreases as the proximity gap increases.

Changing from a pinpoint source to an extended source and varying the size of the mask space produce results similar to those for ADNR II. For example, at 15-μm gap spacing, the difference in Δ between a 3-

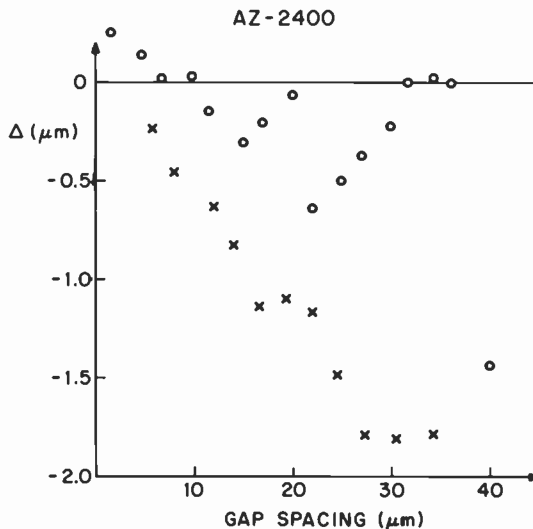

Fig. 8—Experimental (x) and calculated (o) linewidth change, Δ, in AZ-2400 resist for a 5-μm space as a function of the proximity gap spacing. For the calculation, the light source is composed of four different wavelengths and the total dose is 50 mJ/cm^2. The resist thickness is 1.0 μm.

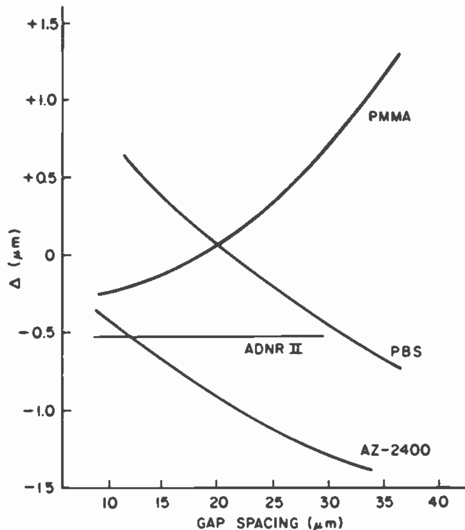

Fig. 9—Measured linewidth change, Δ, as function of the proximity gap spacing for the four resists. Smooth curves have been drawn through the experimental points to emphasize the differences.

μm space and a 6-μm space is almost 0.4 μm. At smaller gap spacings the difference is reduced.

The experimental data for AZ-2400 are shown by the crosses in Fig. 8. As in the case of the negative resist, the fluctuations about the mean are smaller than predicted by the calculations. The general trend is similar, with Δ decreasing more rapidly than the calculations predict. This makes AZ-2400 less promising for this application than ADNR II because the gap spacing requires more careful control.

Similar measurements were performed on the positive resists, PBS and PMMA. We did not model these materials because accurate parameter values were not available. PMMA is sensitive around 220 nm and has a very low absorption coefficient. PBS, which is primarily an electron beam resist, is sensitive only at much shorter wavelengths (approximately 185 nm). The measured values of linewidth error on these two resists are compared with those of AZ-2400 and ADNR II in Fig. 9. The fluctuations were averaged out to emphasize the differences among the resists. PMMA shows the opposite dependence from that of the other two positive resists. This may be because the PMMA films are only lightly absorbing, so that the films were uniformly exposed throughout the thickness. The other two resists have larger absorption, causing the bottom of the films to be less exposed than the top. The profile is thus more sensitive to the exact nature of the light distribution.

4.3 Resist Profiles

The detailed shape of the features formed in the resist layers was studied by scanning electron microscopy. Profiles and cross-sections from one of the ADNR II plates are reproduced in Fig. 10. They show graphically the effect of the interference patterns on the optical intensity distribution. For example, in (d) there is some resist left in the center of the clear area, even though that region is under the middle of the line on the master. Similar images are obtained for the other resists.

The experimental profiles of Fig. 10 are compared with the calcu-

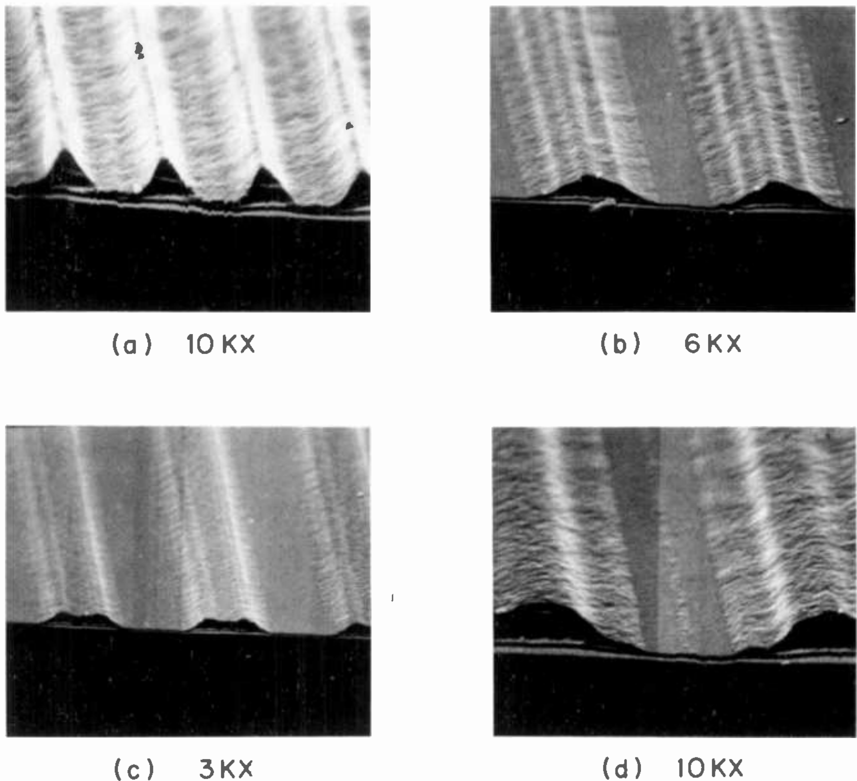

Fig. 10—Scanning electron micrographs of resist profiles in ADNR II at a proximity gap of 13 μm. The exposed and developed plates were broken so that the cross section of the features can be seen and measured. (a), (b), and (c) were taken on groups of equal lines and spaces, of widths 1, 3, and 5 μm, respectively. The symmetric pattern repeats with a period of twice the width. (d) was exposed with a single line of 3-μm width on the mask.

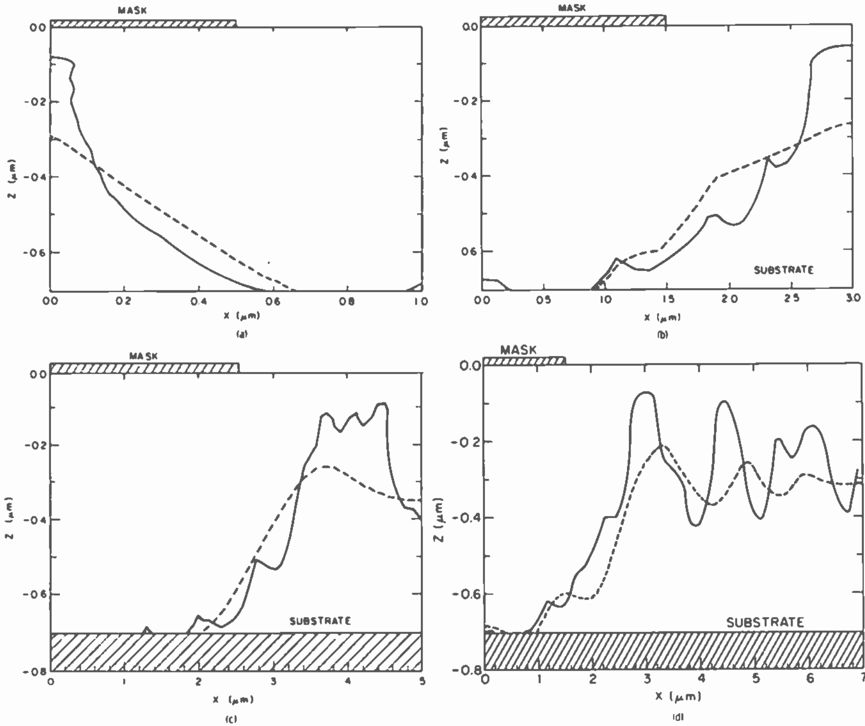

Fig. 11—Comparison of measured and calculated resist profiles in ADNR II. The four figures correspond to those of Fig. 10. The experimental curves (---) are derived from the photos of Fig. 10; the solid curves are calculated with the same parameters as in Fig. 7 and a development time of 10.6 sec.

lated ones in Fig. 11. The dashed curves are copied from the cross sections of Fig. 10. The solid curves were calculated as before, using the experimental exposure dose of 5.6 mJ/cm^2. The development time was adjusted to fit the experimental curves and was the same for all profiles. It can be seen that the calculations reproduce the general features of the interference patterns, such as the remaining resist in the center of Fig. 10d. A particularly striking example is the case of the 1-μm lines and spaces. The solid curve of Fig. 11 (a) predicts that the nonremoved resist lies under the line on the mask, rather than under the space as is required for faithful imaging on a negative resist. The experimental resist line falls in the same place, as is demonstrated in Fig. 12. The photograph shows three line-space patterns of different size on the chrome mask as well as on the etched chrome print. The 4- and 2-μm sizes are faithfully reproduced (in opposite tone because of the negative resist used). However, where there were eight 1-μm spaces

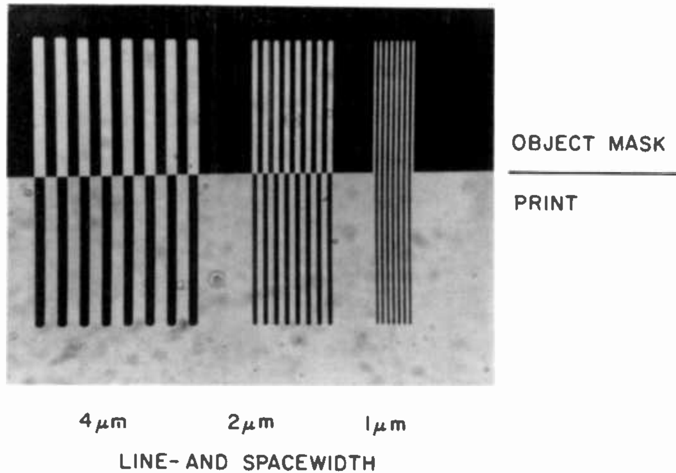

Fig. 12—Photomicrographs of the mask and the chrome print of patterns of equal lines and spaces. The linewidths are indicated on the figure.

on the mask, there are only seven chrome lines on the print, i.e., the lines lie under the lines on the mask, as shown in Fig. 11 (a).

The calculated locations of the peaks and valleys are somewhat different from the experimental ones. This is due either to the proximity gap differing somewhat from the nominal 12.5-μm value or to some approximations used in the model. The experimental patterns also show a "lower contrast" than the calculated ones, due to less than complete coherence of the illumination.

5. Two-Dimensional Patterns

So far, this investigation has been limited to one-dimensional features because of the limitations of the modeling calculations, particularly for the resist development step. Experimental results of imaging square features are shown in Figs. 13 and 14. Fig. 13 contains photomicrographs of squares and line-ends of 3-, 5-, and 10-μm dimensions imaged into ADNR II with a 12-μm proximity gap. The shapes of the resist profiles show good qualitative agreement with the calculations and measurements of L. K. White.[6] The 10-μm features are reproduced with good fidelity, while 5-μm features show some rounding of the corners. For 3-μm features, the shape changes completely.

Fig. 14 compares results for 10-μm squares for the two positive resists PMMA (sensitive at 220 nm) and AZ-2400 (sensitive at 365 nm and beyond) for three different proximity gap values. PMMA produces

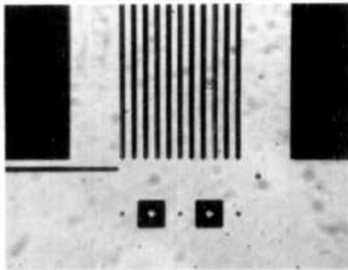
3 μm LINES
AND SQUARES

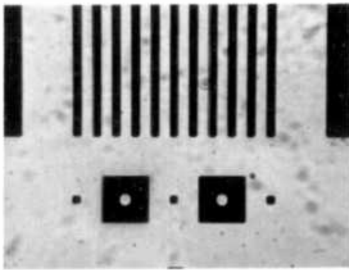
5 μm LINES
AND SQUARES

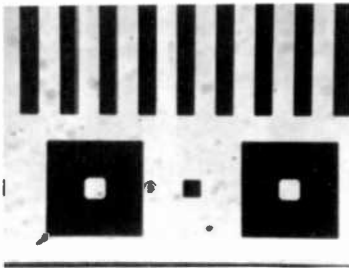
10 μm LINES
AND SQUARES

Fig. 13—Photomicrographs of 3-, 5-, and 10-μm squares on the chrome print. The proximity gap measured 12 μm, and the imaging was done in ADNR II resist.

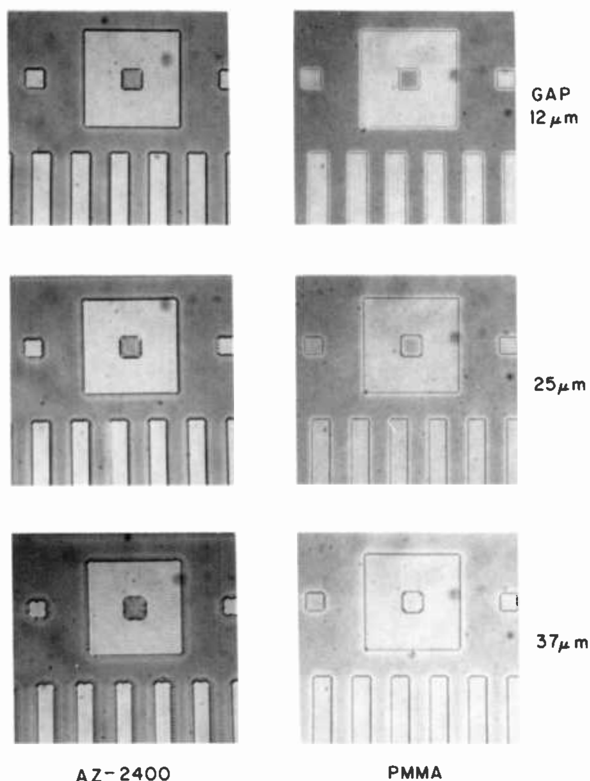

Fig. 14—Comparison of the resist profiles of 10-μm squares in two different positive resists and at three different gap spacings. The peak sensitivity of AZ-2400 is at 365 nm and longer wavelengths, while PMMA is only sensitive in the 220-nm region.

patterns with better fidelity, particularly at the smaller gap values, as is expected from the wavelength difference.

6. Conclusions

We have investigated the technique of out-of-contact proximity printing of chrome masks and have measured the images of long lines and spaces and compared them with the predictions of the SAMPLE calculation. We have also presented some images of two-dimensional features.

We find that lines and spaces as narrow as 3 μm are well reproduced by proximity printing with gaps between 12 and 25 μm. The negative resist ADNR II produces images of linewidths that are less sensitive

to variation in gap-spacing than those produced by the three positive resists. This is important, because nonflatness of the substrates will cause the gap spacing to vary over the image. Two-dimensional features are less well reproduced than lines and spaces. The smallest squares that are well-imaged are between 5- and 10-μm size.

This means that it is unlikely that proximity printing will be applied to copying the 1× masks required for IC generation. However, this technique is satisfactory for duplicating 10× reticles for step-and-repeat printers. The resolution of these printers is about 1 μm for lines and spaces and 1.5 μm for squares. The 10-times-larger features on the reticles can be well replicated by proximity printing. At present, reticles cannot be copied because contact printing introduces too many defects. While ADNR II is the preferred resist for imaging, any of the positive resists will also produce adequate images for reticles if changing the tone of the reticle is undesirable.

Acknowledgments

Fausto Caprari designed and built the xenon light source that made these investigations feasible. We thank him for his assistance and many useful discussions. M. Kaplan and D. L. Ross have made many helpful suggestions in reviewing the manuscript.

References

[1] B. J. Lin, "AZ-2400 as Deep UV Photoresist," *J. Electrochem. Soc.*, **125**, p. 154C, (1978).
[2] B. J. Lin, "Deep UV Lithography," *J. Vac. Sci. Technol.*, **12**, p. 1317, (1975).
[3] M. Feldman, D. L. White, D. A. Chandross, M. J. Bowden, and J. Applebaum, "Demonstration of Photolithography at 1850 A," *Proc. Kodak Microelectronics Seminar 1975*, p. 40.
[4] W. Oldham, S. N. Nandgaonkar, A. R. Neureuther, and M. O'Toole, "A General Simulator for VLSI Lithography and Etching Processes: Part I—Application to Projection Lithography," *IEEE Trans. Electron Dev.*, **ED-26**, p. 711, (1979).
[5] F. Caprari and D. A. Doane, "A Novel Exposure System for High Resolution Deep UV Lithography," *J. Electrochem. Soc.*, **127**(8), p. 336C, (1980). (Electrochemical Society Fall 1980 Meeting, Extended Abstract No. 332.)
[6] L. K. White, "Proximity Printing of Contact Hole Masks," *Interface '81*, Kodak Microelectronics Seminar, Oct 15–16, 1981.

Real Frequency Broadband Matching Using Linear Programming

B. S. Yarman
RCA Laboratories, Princeton, NJ 08540

ABSTRACT—The real frequency technique for single matching problems is implemented employing linear programming. A computational procedure is suggested to approach an optimum design, and computer experiments are performed to investigate the nature of the technique. Different versions of the technique are given for application to bandpass problems. Realizability aspects of the method are also discussed. It is shown that the advantage of using linear programming together with the real frequency technique is that of embedding realizability and design constraints in the computer algorithm as a set of linear inequalities. Examples are presented to show the application of the technique.

1. Introduction

In the design of communication networks, a fundamental problem is to realize a lossless network between a given source and load so that the transfer of power is maximized over a prescribed frequency band. The source network can be represented by an ideal voltage generator with a series impedance given by Thevenin's theorem. In some cases, the source impedance is a pure resistance. In this paper, we refer to power transfer from a resistive generator to a complex load as "single matching" and from a complex generator to a complex load as "double matching."

In 1977, a new numerical approach known as the real frequency technique, was introduced by Carlin[1] for the solution of single-matching problems. The real frequency technique utilizes real-frequency

(measured) data bypassing analytic gain-bandwidth theory. Neither the equalizer topology nor the analytic form of a system transfer function are assumed. They are the result of the design process.

The heart of Carlin's approach resides in generation of the positive real (PR) input impedance $Z_q(j\omega) = R_q(\omega) + jX_q(\omega)$ looking into a lossless matching network with resistive termination. Let the load impedance be $Z_L(j\omega) = R_L(\omega) + jX_L(\omega)$, then the transducer power gain is given by

$$T(\omega) = \frac{4R_q(\omega)R_L(\omega)}{[R_q(\omega) + R_L(\omega)]^2 + [X_q(\omega) + X_L(\omega)]^2}.$$

Once the impedance of the device $Z_L(j\omega)$ is given, $T(\omega)$ depends only on $R_q(\omega)$ and $X_q(\omega)$. If we assume that the unknown impedance $Z_q(j\omega)$ is a minimum reactance function, then $X_q(\omega)$ can be related to $R_q(\omega)$ by Hilbert transformations.[16] In Carlin's approach, the complete problem is solved in two steps. First, $R_q(\omega)$ is described as a set of linear combinations of unknown line segments and, assuming $Z_q(j\omega)$ is minimum reactance, $X_q(\omega)$ is written as the linear combination of the same unknown line segments. These straight line segments are computed in such a way that the transducer power gain is optimized. The second step is to approximate $Z_q(j\omega)$ by a rational function; then $Z_q(j\omega)$ is synthesized as a lossless network with resistive termination.

In this paper, Carlin's real frequency technique for single-matching problems is implemented employing linear programming. For details of the real frequency technique, which are not included here, the reader is referred to Ref. [1].

2. Real Frequency Technique Using Linear Programming

Linear programming is by far the optimization technique in widest and most general use.[2-4] The basic concept is that, given any feasible solution X_0 to a nonlinear programming problem, a linear program can be constructed by expanding each nonlinear function in a taylor series about X_0 and ignoring higher order terms.[2] In many optimization problems, linear programming has been used as a search technique to minimize nonlinear functions without having to evaluate the derivatives.[5] In this paper, however, we preferred to linearize the objective function, since the derivatives from the previous iterations supply significant information.

We have applied the linear programming technique to the following cases:

(1) computation of line segments to optimize transducer power gain, and
(2) approximation of line segments by rational functions.

An efficient solution to linear programming problems can be obtained by the simplex (or revised simplex) technique of Dantzig.[6] Here, we employ the modified revised simplex technique.[7-9]

2.1 Computation of Driving Point Input Impedance (Z_q) of Resistive Terminated Equalizer by Line Segments to Optimize Transducer Power Gain (TPG)

Having chosen the break points R_k as unknowns, the TPG can be expanded in Taylor series in the neighborhood of a given initial guess vector R_0*

$$R_0^T = [r_1, r_2, \cdots r_m],$$

where m is the number of unknown break points. Let Z_q be the unknown driving point impedance of the resistive terminated equalizer and assume it to be minimum reactance. Then, on the $j\omega$ axis

$$Z_q(j\omega) = R_q(\omega) + jX_q(\omega), \tag{1a}$$

the load Z_L

$$Z_L = R_L(\omega) + jX_L(\omega) \tag{1b}$$

and TPG is

$$\begin{aligned} T &= 4\frac{R_q R_L}{(R_q + R_L)^2 + (X_q + X_L)^2} \\ &\approx T(\omega, R_0) + \left(\frac{\partial T}{\partial R}\right)^T \Bigg|_{R_0} (R - R_0) + \cdots . \end{aligned} \tag{2}$$

Neglecting the higher order terms, T is linearized as

$$\hat{T}(\omega, R) = T(\omega, R_0) + b^T(\omega, R_0)(R - R_0) \tag{3}$$

where

$$b(\omega, R_0) = \frac{\partial T(\omega, R)}{\partial R}\Bigg|_{R_0} \tag{4}$$

is the gradient vector. Let G_0 be prescribed as the flat gain level; then one defines the deviation from G_0 as

$$\varepsilon(\omega, R) = \hat{T}(\omega, R) - G_0. \tag{5}$$

* Vector R was used as the unknown vector. It consists of the break points of $R_q(\omega)$ and, generally, the last break point is fixed at zero.

Let e be the maximum of $\varepsilon(\omega, R)$ over the prescribed frequency band ΔB:

$$e = \max_j |\varepsilon(\omega_j, R)|;\ \omega_j \in \Delta B. \quad [6]$$

Observe that

$$e \geq |e(\omega_j, R)| \quad [7]$$

which can be written as

$$e \geq \varepsilon(\omega_j, R) \quad [8a]$$

$$e \leq -\varepsilon(\omega_j, R). \quad [8b]$$

The following problem can be set up. Let $Z = e = \max|e(\omega_j, R)|$ be the objective function to be minimized subject to the constraints of Eq. [8], where e is also considered an unknown. Then the linear programming problem can be formulated step by step as follows:

1. Linearize TPG $\hat{T}(\omega, R)$ in the neighborhood of R_o,

$$\hat{T}(\omega, R) = T(\omega, R_o) + b^T(\omega, R_o)\Delta R,$$

where $\Delta R = R - R_o$ and

$$b^T(\omega, R_0) = [b_1(\omega)b_2(\omega)\ \cdots\ b_m(\omega)] = \text{gradient vector.}$$

2. Define the deviation from the given flat gain level G_o over the sampling frequency chosen in the passband,

$$\begin{aligned} e_j &= \varepsilon(\omega_j, R) \\ &= \hat{T}(\omega, R) - G_0 \\ &= f_j + \sum_{k=1}^{m} b_{jk} r_k,\ j = 1, 2, \cdots, n. \end{aligned} \quad [9]$$

Here

$$f_j = T(\omega, R_0) - \sum_{k=1}^{m} b_{jk} r_{ok} - G_0 \quad [10]$$

$$b_{jk} = \left.\frac{\partial T(\omega_j, R)}{\partial r_k}\right| \text{at } R = R_0 \quad [11]$$

where r_{ok} = components of initial guess vector $R_0 \geq 0$, r_k = components of unknown vector $R \geq 0$, n is the number of sampling points in ΔB, and m is the number of breakpoints, which are chosen as unknowns.

3. Define maximum deviation from G_0

$$e = \max|\varepsilon(\omega_j, R)| \geq 0 \omega_j \in \Delta B,$$

as the objective function. Then the primal form of linear programming

is written to minimize the objective function Z:

$$Z = e \quad [12]$$

subject to the constraints

$$e - \sum_{k=1}^{m} b_{jk} r_k \geq f_j$$
$$e + \sum_{k=1}^{m} b_{jk} r_k \geq -f_j \quad [13]$$

such that unknowns e, $r_k \geq 0$, where $k = 1, 2, \cdots, m$ and $j = 1, 2, \cdots, n$.

In this presentation, there are $(m + 1)$ unknowns and $2n$ inequalities. Generally, the number of sampling points n is much greater than the number of unknowns $(m + 1)$. Therefore, it is more efficient to solve the dual problem.

It is crucial to point out that the above programming requires all r_k to be positive. Hence the physical realizability of the input impedance is built into the formulation of the problem.

One of the most efficient algorithms to solve Eq. [12] is the revised-simplex technique. It requires all the unknowns to be positive, which is a unique advantage compared to nonlinear optimization techniques. For this reason, it is preferable in many applications even though it may require more computations.

Before formulating the dual-problem, we will write the primal problem in the matrix form. It will then be easier to set up the dual problem just by taking the transpose of the matrices.

2.2 Primal Form of Linear Programming

Based upon the previous presentation and notation, we summarize the primal problem in the matrix form. Let e be r_o, the maximum deviation, which is also chosen as an unknown, i.e., $e = r_o$. Denote the new unknown vector (including r_o) with R_{m+1}:

$$R^T_{(m+1)} = (r_o, r_1, \cdots, r_m), \quad [14]$$

where the index $(m + 1)$ shows the number of components in R. Hereafter, similar notations will be employed to indicate the dimension of vectors or matrices (e.g., A_{nm} = Matrix A having n rows and m columns). Also index p and d will be used to denote the variables for primal and dual problems, respectively.

The objective function for primal problem is

$$Z_p = C_P{}^T R_{(m+1)} \quad [15]$$

to be minimized subject to the constraints*

$$D_{2n,(m+1)}R_{(m+1)} \geq F_{2n} \quad [16]$$

with $r_k \geq 0$, $k = 0, 1, 2, \cdots, m$, where

$$C_P^T = (1 \vdots 0_m^T)$$

$$0_m^T = (0, 0, \cdots 0)$$

$$D_{2n,(m+1)} = \begin{bmatrix} U_n & -B_{nm} \\ U_n & B_{nm} \end{bmatrix}$$

$$U_n^T = (1, 1, \cdots, 1)$$

$$B_{nm} = [b_{jk}]\begin{matrix} j = 1, 2, \cdots, n \\ k = 1, 2, \cdots, m \end{matrix}$$

$$b_{jk} = \frac{\partial T(\omega_j, R)}{\partial r_k} \text{ at } R = R_0$$

$$F_{2n}^T = [F_n^T \vdots - F_n^T]$$

$$F_n^T = (f_1, f_2, \cdots, f_n)$$

$$f_j = T(\omega_j, R_0) - \sum_{k=1}^{m} b_{jk} r_{0k} - G_0$$

2.3 Dual Form of Linear Programming

It can be shown that the solution to the set Eq. [16] may also be obtained by solving the following dual problem.[6-8] The objective function Z_d is

$$Z_d = C_d^T X_{2n}, \quad [17]$$

to be maximized subject to the constraints

$$A_d X_{2n} \leq B_d \quad [18]$$

with $X_i \geq 0$, $i = 1, 2, \cdots, n$ where X_{2n} is the unknown vector, X_i is the component of the unknown vector, and

$$C_d = F_{2n} \quad [19]$$

$$A_d = D^T = \begin{bmatrix} - U_n^T & U_n^T \\ B_{nm}^T & B_{nm}^T \end{bmatrix} \quad [20]$$

$$B_d = C_p. \quad [21]$$

* Superscript T indicates the transpose of a vector or matrix.

Having computed the unknown vector X from the dual problem, an optimal solution to the primal problem can easily be computed. In the dual problem, optimal feasible solution X should have the first $(m + 1)$ component different from zero, and the last $2n - (m + 1)$ component should be zero. If $A_{(m+1),(m+1)}$, B_{m+1} and F_{m+1} are the corresponding matrices to optimal feasible solution at the last iteration, the solution to the primal problem is

$$R_{m+1} = A^{-1}_{(m+1),(m+1)}F_{m+1}, \qquad [22]$$

with

$$r_0 = Z_p = Z_d. \qquad [23]$$

Nevertheless, the dual and the primal solutions to the linear programming are efficiently computed along with the numerical work.

2.4 Uniform Approximation of a Given Flat Gain G_0

In the previous section, the linear programming was set up such that the maximum deviation e from the flat gain level G_0 was minimized. This approach leads to a uniform approximation of G_0 in the passband.

The least square approximation of G_0 has the disadvantage that it may miss such details of the data as a spike of short duration. Uniform approximations do not suffer from this problem, but may require more computational effort. Whether or not this additional cost is justified depends on the application.

A simple example will be given to illustrate the use of linear programming in the computation of line segments vis-a-vis the uniform approximation of G_0.

A resistive generator is matched to an $R \| C$ load with $R = 1$, $C = 5$ (Fig. 1). The input admittance Y_q of the resistive terminated equalizer was computed using the line segments, so that a given flat gain G_0 is uniform by approximation. Seven break points are distributed between $\omega_0 = 0$ and $\omega_c = 1.1$, (0, 0.2, 0.4, 0.6, 0.8, 1, 1.1). The revised simplex technique was used to compute the six unknown break points in the passband ($\omega_0 = 0$, $\omega_c = 1$). Passband ($\omega_0 - \omega_c$) was divided into five

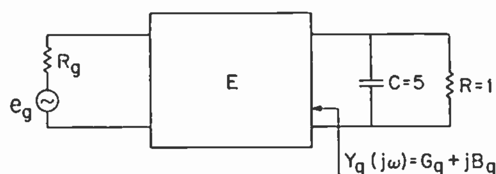

Fig. 1—Conceptual matching of an $R \| C$ load.

Table 1—Performance of Equalizer in Fig. 1 (Using Revised Simplex Technique)

Maximum Gain: 0.7
Minimum Gain: 0.681
Ripple Factor Δ: 0.0279
$\Delta = \dfrac{G_{max}}{G_{min}} - 1$

equal intervals to carry out the computations. Performance of the equalizer is shown in Table 1 and break points are plotted in Fig. 2.

2.5 Rational Form of the Input Impedance

2.5.1 Approximation of Line Segments with Rational Functions

The simplest form of the real part of the input impedance (R_q) is given as

$$R_q(\text{or } G_q) = \frac{1}{P_n(\omega^2)}\,;\ P_n(\omega^2) > 0, \qquad [24]$$

where $P_n(\omega^2)$ is a positive even polynomial. This form of $R_q(\omega^2)$ corresponds to a lossless LC lowpass ladder terminated in a resistance.

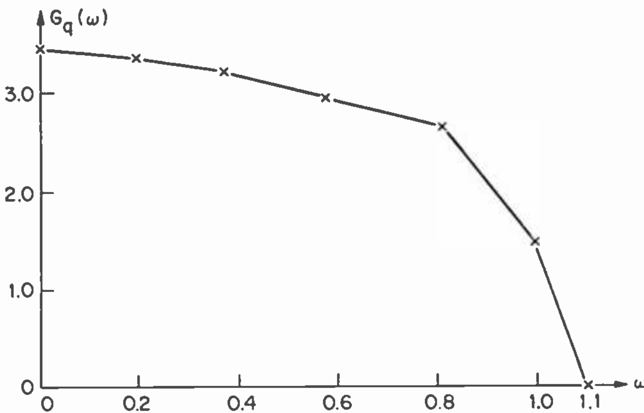

FIXED BREAK FREQUENCIES	0.0	0.2	0.4	0.6	0.8	1.0	1.1
COMPUTED BREAK POINTS FOR Gq	3.4758	3.4268	3.2745	2.9913	2.5512	1.6511	0.0

Fig. 2—Plot of the conductance curve G_q of Fig. 1. The computations given were carried out using revised simplex technique for the approximation of G_0.

For given data points (e.g., line segments for R_q), coefficients of polynomial $P_n(\omega^2)$ can be computed via revised simplex. Let

$$P_n(\omega^2) = X_0 + X_1\omega^2 + \cdots + X_m\omega^{2m} > 0, \quad [25]$$

where X_i, is the unknown coefficient to be determined.

Since $P_n(\omega^2)$ is strictly positive, the coefficients X_0 and X_m have to be positive too. This is necessary but not sufficient for $P_n(\omega^2)$ to be positive. For many practical cases, it may be sufficient to force $(X_0, X_m) > 0$ to make $P_n(\omega^2)$ positive.* However, no sign restriction is imposed on the rest of X_i, except $P_n(\omega^2)$ is positive.

It is important to note that simplex or revised simplex algorithms require nonnegative unknowns in the formation of the problem. Therefore, when the coefficients of Eq. [25] are computed, they have to be expressed in terms of nonnegative variables. The following outline may be followed to set-up the linear programming problem.

1. Let $P_n(\omega^2) = \sum_{i=0}^{m} X_i\omega^{2i}$

2. Define error function $e(\omega_j)$

$$e(\omega_j) = e_j$$

$$e_j = P_n(\omega_j^2) - \frac{1}{R_q(\omega_j)}$$

3. Define objective function Z

$$Z = \max|e(\omega_j)| = e$$

4. Set-up the unknown vector W with

$$X_0 > 0$$

$$X_m > 0$$

$$X_i = u_i - v_i,\ i = 1, 2, \cdots, (m-1)$$

where $(u_i, v_i) \geqslant 0$. Then

$$W^T = [e, X_0, u_1, u_2, \cdots, u_{m-1}, v_1, v_2, \cdots, v_{m-1}, X_m]$$
$$= [w, w_1, w_2, w_3, w_4, \cdots, w_{2m+1}, w_{2m+2}].$$

5. The primal problem can be written as the objective function $Z = w_1$ to be minimized subject to constraints

$$\left.\begin{matrix} w_1 \geqslant e_j \\ w_1 \leqslant -e_j \end{matrix}\right\} \forall\ \omega_j \in \Delta B.$$

* So far this has been the case for all the low-pass and some of the bandpass problems solved using real frequency techniques.

with $w_k \geq 0$, $k = 1, 2, \cdots (2m+1)$, where

$$e_j = \sum_{i=1}^{m-1} u_i\omega^{2i} - \sum_{i=1}^{m-1} v_i\omega^{2i} + X_0 + X_m\omega^{2m} - \left\{\frac{1}{R_q(\omega_j)}\right\}$$

$$= w_2 + w_3\omega^2 + w_4\omega^4 + \cdots$$

$$+ w_{2m+1}\omega^{2(m-1)} + w_{2m+2}\omega^{2m} - \left\{\frac{1}{R_q(\omega_j)}\right\}.$$

In the matrix form, the objective function $Z = C^TW$ is to be minimized subject to constraints $AW \geq F$ where

$$C^T = (1 \mid 0^T_{2m+1}) = (1, 0, 0, \cdots, 0)$$

$$A = \left[\frac{U_n \mid \Omega}{U_n \mid -\Omega}\right]; \Omega = [\omega_j^{2k}], \begin{cases} j = 1, 2, \cdots, n \\ k = 1, 2, \cdots, (m+1) \end{cases}$$

$$F = [F_n^T \mid - F_n^T], F_n = [f_1, f_2, \cdots, f_n]$$

$$U_n^T = (1, 1, \cdots 1), f_i = \frac{1}{R_q(\omega_j)}.$$

Having set up the primal problem in matrix form, it is more efficient to solve the dual problem, since the number of sampling points (n) is much greater than the number of unknowns $(2m+2)$.

2.5.2 Uniform Approximation of Flat Gain G_0 When the Input Impedance (or Admittance) is a Rational Function

The procedure that may be followed for this case is very similar to the one explained in Section 2.1. Combining Sec. 2.5.1 with Sec 2.1, the following set-up may be proposed to approximate the TPG uniformly about the given flat level G_0. For this case, the real part (R_q) of the driving point impedance of the equalizer is chosen as a rational function and the unknowns of the problem are the coefficients of $R_q(\omega^2)$. The imaginary part X_q of the input impedance is generated by the line segment technique, i.e., rational $R_q(\omega^2)$ is sampled by a reasonable number of line segments. Then the same line segments are used to generate $X_q(\omega)$. This procedure avoids the generation of the analytic form of the input impedance $Z_q(j\omega)$ in the course of optimization. The objective function $Z_p = C_p{}^TW$ is to be minimized subject to the constraints $A_pW \geq F_p$. W is defined as in the previous section and

$$C_p{}^T = [C^T_{m+1} \mid C^T_{m+1}],$$

$$C^T_{m+1} = (1, 0, \cdots, 0) = (1 \quad 0_m{}^T),$$

$$F_p = [F_n^T \mid -F_n^T],$$

$$A_p = \left[\begin{array}{c|c} U_n & -B_{nm} \\ \hline U_n & B_{nm} \end{array}\right]$$

$$U_n^T = (1, \cdots, 1),$$

$$B_{nm} = \left.\frac{\partial T(\omega_j, x)}{\partial X_k}\right| = [b_{kj}], \text{ at } X = X_0$$

$$F_n = (f_1, f_2, \cdots f_n)$$

$$f_i = f(\omega_i) = T(\omega_i, X_0) - G - \left(\frac{\partial T}{\partial X}\right)\Bigg|_{X_0}^{T} X_0,$$

X = unknown vector

X_0 = initial guess to X.

m = degree of polynomial $P_m(\omega^2)$, which is written as

$$R_q(\omega^2) = \frac{1}{P_m(\omega^2)}; \; P_m(\omega^2) = X_0 + X_1\omega^2 + \cdots + X_m\omega^{2m},$$

where n is the number of sampling points over the prescribed pass band.

2.6 Dual Problem

As was pointed out in the previous sections, it is more efficient to solve the dual problem as follows. The objective function $Z_d = C_d^T Y$ is to be maximized subject to the constraints $A_d Y \leqslant F_d$ such that $y_i \geqslant 0$. Here

$A_d = A_p^T$

$C_d = F_p^T$

$F_d = C_p^T$

Y = unknown vector

The solution to the primal problem can be computed using Eq. [22].

2.7 Comparison of Uniform and Least Square Approximations

As an example, 3-element lossless equalizers were constructed for *RCL* Load (Fig. 3) such that the transducer power gain was optimized for a given flat gain G_O employing the following techniques: (1) approximation of G_O in the least square sense[9] and (2) uniform approximation of G_O using revised simplex. For both cases, the real part of the

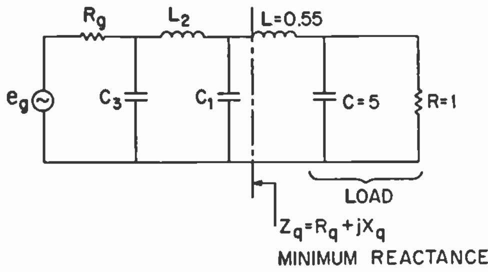

Fig. 3—Circuit topology of the 3-element lossless equalizer.

minimum reactance input impedance (R_q) was chosen as

$$R_q(\omega^2) = \frac{x_0}{1 + x_1\omega^2 + x_2\omega^4 + x_3\omega^6}. \quad [26]$$

Along with the computations, the imaginary part of the input impedance (X_q) was generated using the line segment technique over 200 points between $\omega_0 = 0.0$ and $\omega_e = 5$. Final element values and the performance of the equalizers are summarized in Table 2.

3. Optimum Matching[11]

In broadband matching, when a complex load is to be matched to a resistive (or, in general, a complex) generator by a lossless equalizer, the major interest is focused on the passband gain. The best performance requires that minimum passband gain be as large as possible. Accordingly, in this paper, the following optimum gain-bandwidth criterion by Carlin is used.

Let m be the order of the matching equalizer, where m is equal to the number of energy storage elements in the equalizer. For a given order of m and given passband, the equalizer with optimum gain-bandwidth response is the one with maximum value of minimum gain in the passband. Note that, in this definition, a pair of perfectly-coupled coils is counted as one energy storage element.

Based upon the above definition, it was shown that, in contradiction to Refs. [12]-[15], the equalizers constructed from analytic gain-bandwidth theory using Chebyshev polynomials are not optimum.

Table 2—Element Values and Performance of 3-Element Equalizer Constructed Using Revised Simplex and Least Square Optimizations

	C_1	L_2	C_3	R_g	G_0	ϵ
Revised Simplex	5.28	0.512	2.7	0.347	0.684	0.080
Least Square	5.31	0.552	2.54	0.372	0.697	0.093

In this section using the optimum gain-bandwidth criterion, a simple numerical procedure is given to search for the optimum design. The procedure was implemented for the real-frequency technique.

The first step is to linearize the gain function in the neighborhood of a given initial guess x_0 (as was the case for the uniform approximation of G_0). Then the objective function Z is defined as the minimum gain over the passband. Hence one maximizes the minimum gain. Let $R_q(\omega^2, x)$ be defined as in Eq. [24]. The transducer power gain is linearized in the neighborhood of a given initial guess x_0. Then the following steps may be used to set up the linear programming problem:
(1) Linearize the transducer power gain:

$$\hat{T}(\omega, x) = T(\omega, x_0) + \left(\frac{\partial T}{\partial x}\right)^T \Delta x. \qquad [27]$$

(2) Define the objective function Z as

$$Z = \text{minimum of } \hat{T}(\omega, x) \geq 0, \qquad [28]$$

which is to be maximized subject to the constraints minimum of $\hat{T}(\omega, x) \leq \hat{T}(\omega, x)$.
(3) Primal Problem: Let G_{min} = minimum of $T(\omega, x)$ in the passband. The objective function

$$Z = G_{min} \qquad [29]$$

is to be maximized subject to constraints

$$G_{min} \leq T(\omega_j, x_0) + b^T(\omega_j)(x - x_0)$$

$$G_{min} \geq G_0$$

where G_0 is the restriction on the lower bound of gain, G_{min} and the components of vector X are the unknowns, and ΔB is the prescribed passband.

We write Eq. [29] in the matrix form. The objective function

$$Z = C_p{}^T x$$

is to be maximized subject to constraint

$$A_p X \geq F_p,$$

where

$X^T = (G_{min}, X_0, x_1, \cdots X_m)$ the unknown vector

$C_p{}^T = (1 \,\vdots\, 0^T_{m+1})$

$A_p = [-U_n \,\vdots\, B_{n,(m+1)}]$

$F_p{}^T = (f_1, f_2, \cdots, f_n)$

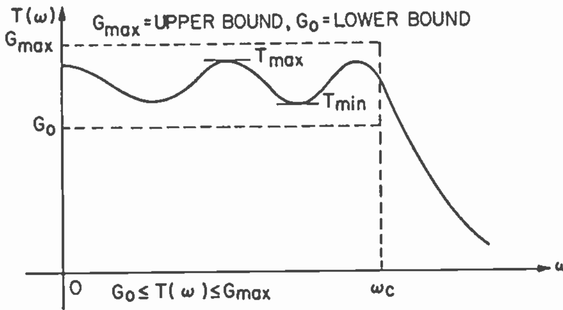

Fig. 4—Flat upper and lower bounds forced on the transducer power gain in the passband ($0 \leq \omega \leq \omega c$).

$$f_j = b^T(\omega_j)X_0 - T(\omega_j, X_0)$$

$$b^T(\omega_j) = \left.\frac{\partial T(\omega_j, X)^T}{\partial X}\right|_{X_0} = (b_{0j}, b_{1j}, \cdots, b_{mj})$$

$B_{n,(m+1)} = [b_{kj}]$, $k = 0, 1, 2, \cdots, m$ and $j = 1, 2, \cdots, n$.

The same problem can be set up to solve the unknown vector ΔX in Eq. [27] with

$$X_0 + \Delta X_0 \geq 0$$

$$X_n + \Delta X_n \geq 0$$

and the constraints of Eq. [29]. This increases the number of inequalities, but the difference between the solutions is not noticeable.

Note that in the above formulation, it is also possible to impose an upper bound on the gain function over the prescribed frequency band. This idea can be implemented by adding one more set of inequalities to the conditions of Eq. [29]:

$$\hat{G}(\omega_i, X) \leq G_{max}, \omega; \in \Delta B$$

where G_{max} is the desired upper bound. Hence within the range of specified lower and upper bound (or, for a specified ripple factor or less) it is possible to maximize the minimum gain (Fig. 4).

It is important to point out that, in order to find the optimum solution for the above set up, it is essential to start with a reasonable

Table 3—Element Values of Fig. 5 for Chebyshev and Real Frequency Equalizers

Equalizer	C_1	L_2	C_3	L_4	R_g
Real Frequency	6.3588	0.5581	5.9547	0.3647	0.2144
Chebyshev	5.6618	0.59027	4.631	02992	0.31933

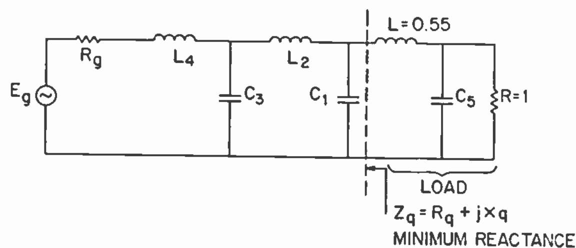

Fig. 5—Circuit topology of 4-element real frequency equalizer.

initial guess X_0. A initial guess to this problem can be obtained either from line segment solution or from any other nonlinear optimization program that computes ΔX or vector X.

As an example, for an RCL load with $R = 1$, $C = 5$, and $L = 0.55$, a four element "real frequency equalizer" was constructed using the numerical procedure just described. It yields an almost optimum solution so far as the definition of the optimum gain-bandwidth criterion is concerned. This result is compared with the four-element Chebyshev equalizer of analytic theory.[12]* The results are shown in Table 4 and the element values of the equalizer (shown in Fig. 5) are listed in Table 3. Gain plots of the equalizers are shown in Fig. 6.

As can be seen from the tables and plots, the optimum solution of real frequency is better than the Chebyshev equalizer. Using the real frequency technique for finding the maximum of the minimum, minimum gain was significantly improved while the ripples were smaller in the passband where the passband was chosen from $\omega_0 = 0$ to $\omega_c = 1$.

4. Study of Ripples

In the previous section, a numerical procedure was presented to approach the optimum solution for specified lower-upper bound of the gain in the passband. This optimization scheme leads to the idea of construction of the real frequency equalizers such that, for any fixed $\Delta = (G_{max}/G_{min}) - 1$ the minimum gain in the passband is maximized or that, for any specified minimum of the gain, Δ is minimized.

Table 4—Comparison of 4-Element Chebyshev and Real Frequency Ladder Equalizers

	Real Frequency	Chebyshev
G_{min}	0.646	0.582
G_{max}	0.754	0.828
$\Delta = (G_{max}/G_{min}) - 1$	0.167	0.423

* The Chebyshev equalizer was constructed using formulas given by Levy.[12]

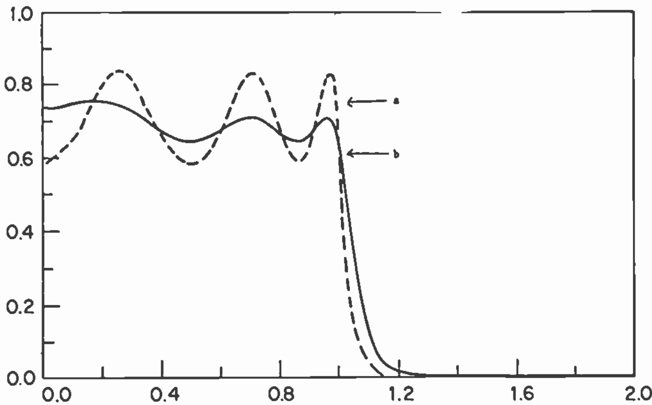

Fig. 6—Performance of the matched networks of 4-element equalizer: curve (a) equal ripple response and curve (b) real frequency response.

In this section the relation between the ripples and the minimum gain in the passband has been studied numerically. Results show that it is possible to construct a real frequency equalizer with the following attributes.

(1) For any fixed Δ, the minimum gain in the passband is maximized. That is to say, the real frequency technique offers almost optimum equalizer for any fixed Δ; or

(2) For specified minimum gain in the passband, the ripple factor Δ is minimized. In other words, for fixed lower bound, the largest peak of the gain is minimized. Thus, the real frequency technique offers the equalizer with the smallest ripple for any fixed lower bound of gain in the passband.

In the following experiments, as the minimum gain in the passband was swept, the corresponding Δ was minimized so that the relation between the minimum gain and the ripple could be traced numerically. All the computations have been carried out using linear programming with the revised simplex algorithm.

Experiment 1: For $R \| C$ load ($R = 1$, $C = 5$), the input impedance of the resistive-terminated equalizer was computed using the line segment technique such that, for different fixed lower bounds of the gain, the ripple factor Δ was minimized. Hence, the relation between the minimum of the passband gain and the ripple factor Δ was examined. For this experiment, seven break frequencies were fixed (0, 0.2, 0.4, 0.6, 0.8, 1, 1.1). Minimum susceptance design was preferred. The result of the experiment is shown in Fig. 7.

As shown in the figure, $G_{min} = f(\Delta)$ has two branches for $\Delta < 0.3$, which means that as the minimum gain increases, the ripples become

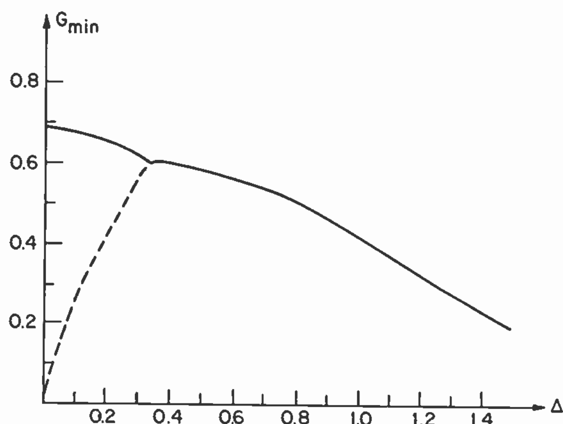

Fig. 7—Plot of G_{min} versus Δ using Fig. 1.

smaller. Also, it is possible to construct equalizers with small ripples for fixed lower gains. For $\Delta > 0.3$, G_{min} reduces smoothly. With this choice of break points, the optimum solution of the real frequency technique gives $G_{min} = 0.682$ and $\Delta = 0.04$.

Experiment 2: Here, experiment 1 is repeated for RCL load ($R = 1$, $C = 5$, $L = 0.55$). The same seven break frequencies were fixed. Break points of the line segments were computed such that, for fixed minimum of gain, ripple factor Δ was minimized over the prescribed frequency band. Minimum reactance design was preferred. The numerical relation between the minimum gain and Δ is shown in Fig. 8. In this case, an almost optimum solution is obtained for $G_{min} = 0.643$, $\Delta = 0.141$.

Experiment 3: In this experiment, using the same RCL load as experiment 2, a four-element, low-pass real frequency equalizer was constructed. As in the previous examples, the ripple factor Δ is minimized for fixed lower bounds of gain. The result obtained in this experiment is very similar to that of Experiments 1 and 2. Fig. 9 shows G_{min} versus Δ. The best result obtained with this low-pass ladder with monotone

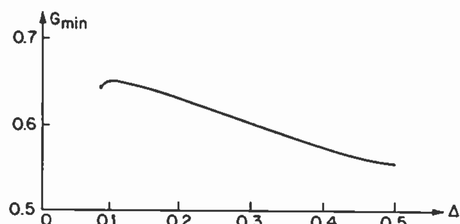

Fig. 8—$G = f(\Delta)$. The line segment solution for the equalizer to RCL load with $R = 1$, $C = 5$, $L = 0.55$.

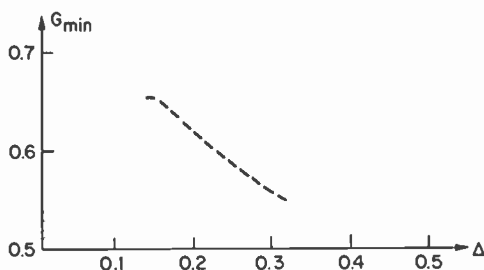

Fig. 9—G_{min} versus Δ for the four-element real frequency equalizer, constructed for RCL load with $R = 1$, $C = 5$, $L = 0.55$.

roll-off is $G_{min} = 0.646$, $\Delta = 0.168$. This is almost the optimum solution that the real frequency technique can offer.

5. Design of Bandpass Equalizers

In this section, an organized procedure will be described for designing bandpass equalizers via the real frequency technique using linear programming. Examples will also be presented.

5.1 Line Segment Solution

The first step is the computation of line segments to design the real frequency bandpass equalizers. Here, the algorithm given in Sec. 2 is used; however, for the bandpass problems, the choice of the line segments is a slightly different from the low-pass cases because of the zeros of transmission at dc (i.e., $\omega = 0$). There are several possibilities for representing the real part of the input impedance (R_q) of the resistive-terminated equalizer:

(1) *Low Pass Input*:
If the load has the zero of transmission at $\omega = 0$, then it may be sufficient to consider the real part of the input impedance R_q as having no zeros of transmission at dc.* In this case, the line segments for R_q will be chosen as they were in the low-pass design.

(2) *Bandpass Inputs*:
No matter what the load (whether it has zero transmission at dc or not), the line segments for $R_q(\omega)$ can be chosen so that beyond the passband frequencies, $R_q(\omega)$ goes to zero as shown in Fig. 10. In this case, end points of the line segments are strictly fixed at the zero level

* If the load does not have any zero of transmission at dc, then one may want to extract a reactive element from the equalizer (either a series C or a shunt L) so that a zero of transmission is introduced at dc. This element can be considered as part of the load. Hence the idea of low-pass input follows.

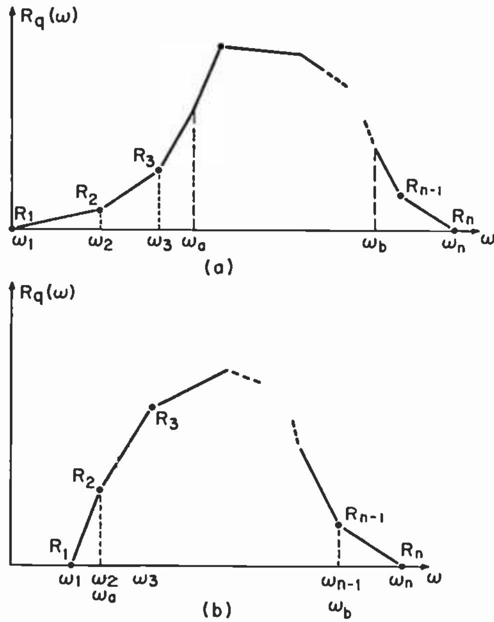

Fig. 10—Bandpass choice of the break points for the real part of the input impedance (R_q) of the resistive-terminated equalizer: (a) low-pass input; (b) bandpass input.

(i.e., $R_1 = 0$, $R_n = 0$). The fixed break frequencies of the end points control the sharpness of the roll off in the stop band. Note that in this solution, input impedance Z_q to the equalizer should be minimum reactance or minimum susceptance.

(3) *Element Extraction with Bandpass Input*:

There are some cases for which the input impedance to the equalizer is neither minimum reactance nor minimum susceptance. The two possible cases are shown in Fig. 11. These input impedances are often encountered in the design of bandpass equalizers, since different combinations of L and C elements are possible in the circuit topology. In this case, a reactive element can be extracted from the equalizer yielding the minimum-reactance (or minimum-susceptance) input impedance Z_q for the rest of the equalizer. In Fig. 11a, a series capacitor C_x is extracted from the equalizer so that the input impedance $\hat{Z}_q$ to the equalizer is minimum reactance. Similarly in Fig. 11b, a shunt inductor L_x is extracted from the equalizer so that the input admittance $\hat{Y}_q$ is minimum susceptance. In Fig. 11, the extracted elements introduce a zero of transmission at dc. However, there may be cases where the extracted elements introduce zero of transmission at finite frequencies or at infinity. Clearly the type of extraction depends on the

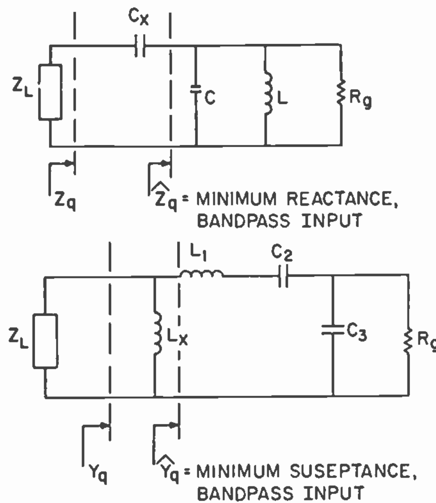

Fig. 11—Typical examples to the bandpass equalizers for which the input impedance is neither minimum reactance nor minimum susceptance.

load and the design specifications. Nevertheless, for most applications, it is sufficient to extract the reactive elements that introduce the zero of transmission at dc.

(4) *Low-Pass to Bandpass Transformations*:
If the given load is analytic and simple enough, it is possible to find the low-pass equivalent form of the load. Then one can solve the low-pass problem via the real frequency technique. Finally, the design is completed by using the low-pass to bandpass transformation. Since the number of low-pass prototype elements should be doubled in the final bandpass equalizer, this procedure is not a favorable one.

5.2 Rational Approximation of Line Segments for Bandpass Problems

The second step of the design procedure is the approximation of the line-segment solution. If the line segments go to zero, which is the typical case for bandpass problems, then the general form of the real part of the input impedance $R_q(\omega^2)$ (or $G_q[\omega^2]$) is

$$\hat{R}_q(\omega^2) = \frac{x_0\omega^{2k}}{1 + x_1\omega^2 + x_2\omega^4 + + \cdots x_n\omega^{2n}} \qquad [30]$$

or

$$\hat{R}_q(\omega^2) = \frac{x_0}{\omega^{-2k} + x_1\omega^{2(1-k)} + \cdots + x_n\omega^{2(n-k)}} \qquad [31]$$

Here, the numerical problem is to determine the coefficients of $\hat{R}_q(\omega^2)$ such that $\hat{R}_q(\omega^2) > 0\forall\omega$ and $\hat{R}_q(\omega^2)$ is the best fit to the line segment solution R_q.

Clearly, the algorithm introduced in Sec. 2.5 can also be used here with slight modification. It should be noted that algorithms introduced previously do not guarantee that $R_q(\omega)$ is positive over the entire frequency range $-\infty \leq \omega \leq \infty$. In this case, one may want to employ a constraint optimization routine that guarantees $R_q(\omega) \geq 0$. Use of a constraint optimization program is time consuming and may not yield satisfactory results. However, the following algebraic procedure overcomes the difficulties due to realizability.

A numerical-algebraic procedure is proposed to construct the nonnegative polynomials and approximate the line segments by rational functions.

Let $P_A(\omega)$ be an all-degree polynomial in ω, i.e.,

$$P_A(\omega) = a_0 + a_1\omega + \cdots + a_n\omega^n. \quad [32]$$

Let us define the nonnegative polynomial $P(\omega^2)$ as

$$P(\omega^2) = \frac{P_A^2(\omega) + P_A^2(-\omega)}{2} \geq 0\omega$$

$$P(\omega^2) = x_0 + x_1\omega^2 + x_2\omega^4 + \cdots + x_n\omega^n. \quad [33]$$

Then the coefficient x_i can be written in terms of a_n,

$$\begin{aligned} x_0 &= a_0^2 > 0 \\ x_1 &= a_1^2 + 2a_0a_2 \\ x_k &= a_k^2 + 2\sum_{j=1}^{k} a_{j-1}a_{2k-j+1} \\ x_n &= a_n^2 > 0. \end{aligned} \quad [34]$$

For given line segment solution, one can set

$$\hat{R}_q(\omega^2) = \frac{A_k\omega^{2k}}{x_0 + x_1\omega^2 + \cdots + x_n\omega^{2n}} \geq 0 \quad [35]$$

or

$$\hat{R}_q(\omega^2) = \frac{2A_k\omega^{2k}}{P_A^2(\omega) + P_A^2(-\omega)} \geq 0 \quad [36]$$

with $A_k > 0$.

Hence the problem reduces to a determination of the real coefficients a_i to find the best fit to the given line segments. In this case, the numerical problem is no longer linear. However, any nonlinear opti-

mization (such as Levenberg-Marquard) technique may be employed. Finally, the coefficients x_k are computed.

5.3 Examples of Bandpass Problems

In the following examples, algorithms introduced for low-pass problems are employed with slight modification.

Example 1: Computation of Bandpass Input Impedance Z_q
In this example (Fig. 12a), it is desired to illustrate a typical solution to bandpass problems via line segments. The line segment solution for *RCL* load with $R = 1$, $C = 5$, $L = 0.55$ was obtained. A series capacitor was also extracted from the equalizer yielding the minimum reactance input impedance for the rest of the equalizer with resistive termination. A rough sketch of the line segments is shown in Fig. 12b.

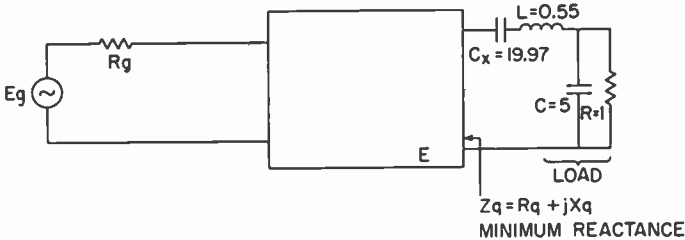

Fig. 12a—Computation of line segment input impedance of resistive-terminated equalizer to *RCL* load with $R = 1$, $C = 5$, $L = 0.55$. A capacitor C_x is extracted from the equalizer.

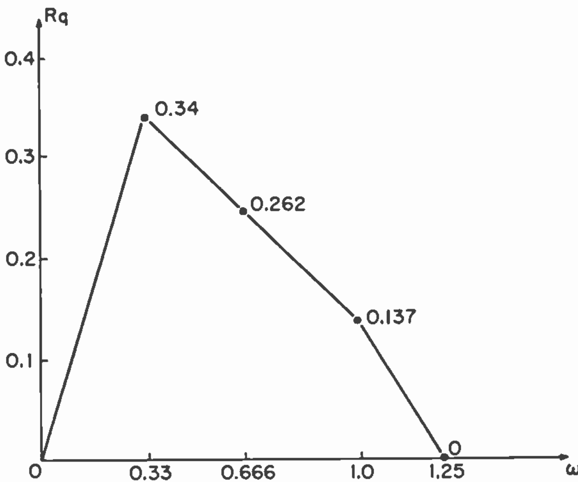

Fig. 12b—Line segment solution to Example 1.

The solution is outlined as follows:

Type of Design: Bandpass Minimum Reactance with Extracted Capacitor C_x.
Passband: $0.2 \le \omega \le 1$.
Break Frequencies: $\omega_1 = 0$; $\omega_2 = 0.33$; $\omega_3 = 0.66$; $\omega_4 = 1$; $\omega_5 = 1.25$
Solution to the Breakpoint R_k: $R_1 = 0$; $R_2 = 0.344$; $R_3 = .262$; $R_4 = 0.137$; $R_5 = 0$
Extracted Capacitor: $C_x = 19.97$
Performance of the Equalizer: $G_{min} = 0.55$, $G_{max} = 0.728$

Example 2:
In this example, a three element, bandpass equalizer was constructed for RCL load with $R = 1$, $C = 5$, $L = 0.55$ (Fig. 13).
Passband: $0.2 \le \omega \le 1.0$
Design Type: Minimum Reactance, a series capacitor C_x was also extracted from the equalizer.
Line Segment Solution: This is given in Example 1 (Fig. 12b).

The rational form of the real part of the input impedance $R_q(\omega^2)$ is found to be (Fig. 14a)

$$R_q(\omega^2) = \frac{A\omega^2}{B_2\omega^4 + B_1\omega^2 + 1},$$

where $A = 9.936$, $B_1 = 12.085$, and $B_2 = 50.17$.

The rational form of the input impedance $Z_q(s)$ is

$$Z_q(s) = \frac{a_1 s}{b_2 s^2 + b_1 s + 1},$$

where

$a_1 = 1.93921148$
$b_1 = 5.124048781$
$b_2 = 7.083149355$.

The performance of the equalized structure (Fig. 14b) is

$G_{max} = 0.650$

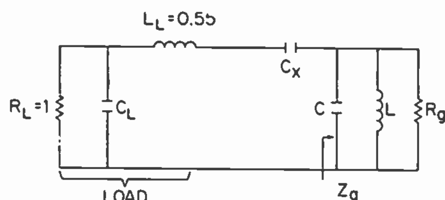

Fig. 13—Circuit topology of the equalizer of Example 2. The element values are $C_x = 12.063$, $C = 3.656$, $L = 1.939$, $R_q = 0.3784$.

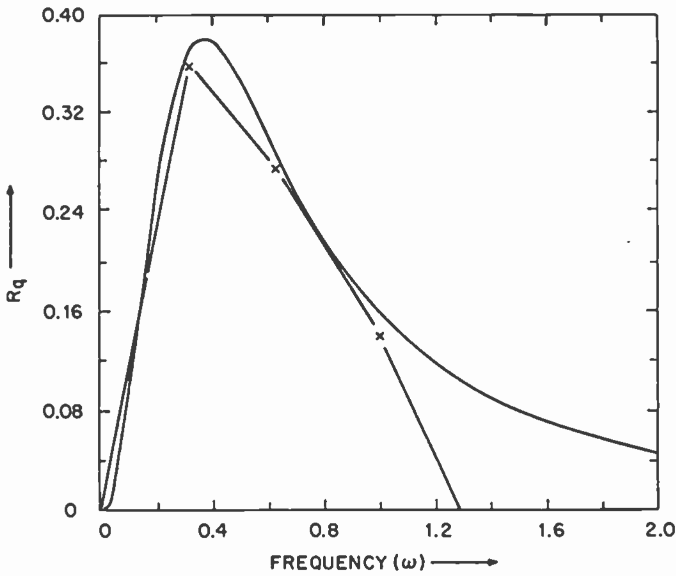

Fig. 14a—Real part of the input impedance of the equalizer for Example 2.

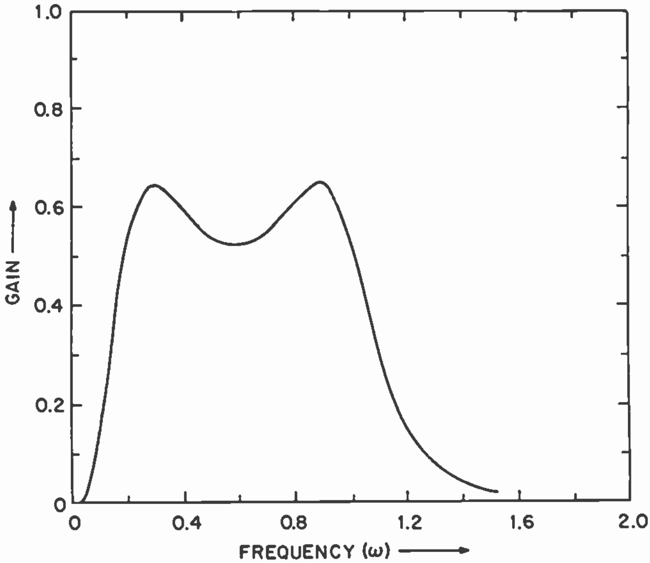

Fig. 14b—Performance of the matched system of Example 2.

$G_{min} = 0.525$

$$\Delta = \frac{G_{max}}{G_{min}} - 1 = 0.238.$$

Example 3:

This example is very similar to Example 2. Utilizing the same procedure, a five element, bandpass equalizer was designed for the *RCL* load ($R = 1$, $C = 5$, $L = 0.55$). The final circuit topology is shown in Fig. 15 and the results are summarized below:

Passband $= 0.2 \leq \omega \leq 1.0$

Design Type: Minimum reactance; a series capacitor C_x was extracted from the equalizer.

Line Segment Solution: As in Example 1.

The rational form of the real part of the input impedance $R_q(\omega^2)$ was found to be

$$R_q(\omega^2) = \frac{A\omega^2}{B_4\omega^8 + B_3\omega^6 + B_2\omega^2 + 1},$$

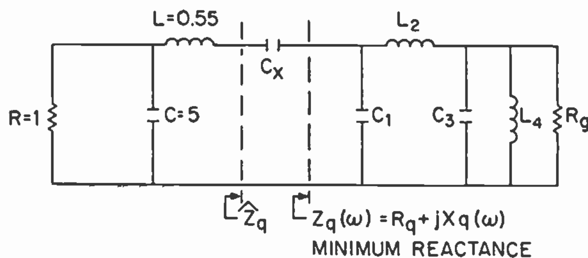

Element Values:

C_x	=	21.130	C_1	=	6.495
L_2	=	0.367	C_3	=	4.405
L_4	=	0.60	R_g	=	0.227

Fig. 15a—The circuit topology of the equalizer of Example 3 for case (1) (see text).

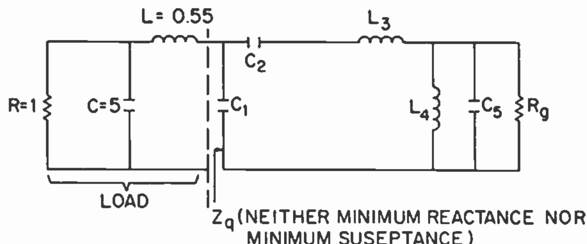

Fig. 15b—The circuit topology for the equalizer of Example 3 for case (2) (see text).

Table 5—Chebyshev Versus Real Frequency Bandpass Matching (Lead : $L = 0.55$, $C = 5.0$, $R = 1$; Passband: $0.2 \leq \omega \leq 1.0$)

Design Method	Total Equalizer Elements	Number of Coupled Coils in Matching Networks	G_{min}	$\Delta = \frac{G_{max}}{G_{min}} - 1$
Real Frequency	3	0	0.525	0.238
Real Frequency	5	0	0.628	0.08
Chebyshev	10	2	0.522	0.185
Chebyshev	14	2	0.587	0.09

where (see Fig. 16a)

$A = 12.20$
$B_1 = 12.11$
$B_2 = 210.90$
$B_3 = 442.23$
$B_4 = 324.43$

The rational form of the input impedance $Z_q(s)$ is

$$Z_q(s) = \frac{a_3 s^3 + a_2 s^2 + a_1 s}{b_4 s^4 + b_3 s^3 + b_2 s^2 + b_1 s + 1},$$

where

$a_1 = 2.034$ $\quad b_1 = 7.323$
$a_2 = 2.691$ $\quad b_2 = 20.758$
$a_3 = 2.773$ $\quad b_3 = 17.48$
$b_4 = 18.01$

For the circuit Topology, we may consider the following cases:

(1) Synthesize $Z_q(s)$ as it is. The structure will consist of synthesized Z_q and a series C_x, as shown in Fig. 15a.

(2) Define $\hat{Z}_q(s) = Z_q(s) + (SC_x)^{-1}$; then synthesize it such that the element distribution is improved as compared to case (1). $\hat{Z}_q(s)$ is not minimum reactance any more. Fig. 15b shows a possible circuit topology.*

The performance of the equalized structure (Fig. 16b) is

$G_{max} = 0.674,$

$G_{min} = 0.628,$

$\Delta = 0.07.$

* As a matter of fact, it was found that this topology of Fig. 15b provides the best element distribution for this example.

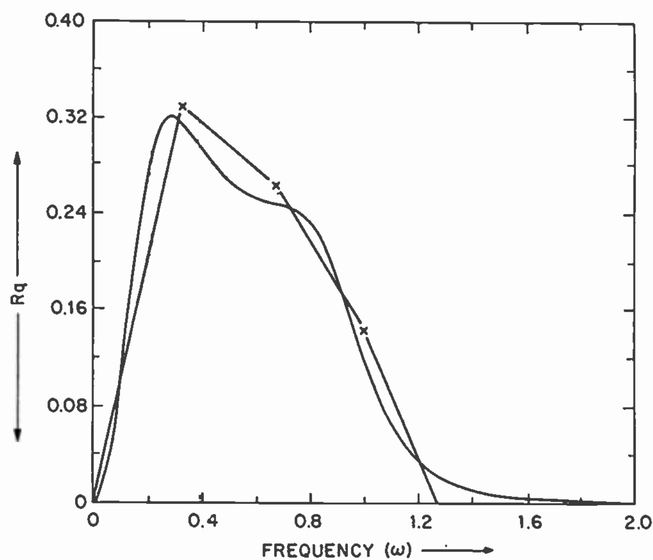

Fig. 16a—Real part of input impedance of the equalizer of Example 3.

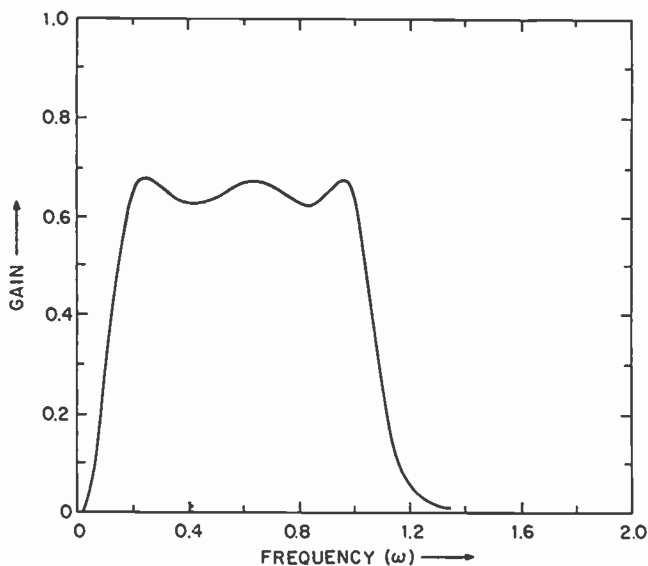

Fig. 16b—Gain response of Example 3.

Note that this problem can also be solved analytically employing the Chebyshev formula published in Ref. [15]. Comparative results are summarized in Table 5.[10]

6. Conclusion

In this paper, the real frequency technique for single matching problems has been implemented to design matching networks for both lowpass and bandpass problems using linear programming. A numerical procedure that employs the simplex algorithm has been utilized to reach optimum design. Computer experiments have also been performed to investigate the nature of the technique. It has been shown that the real frequency technique using linear programming offers matching networks with almost optimum gain performance.

Different versions of this technique have been applied to bandpass problems. Realizability aspects of the technique have also been discussed. An algebraic method for imposing realizability has been suggested that can readily be employed with the numerical setup of the problem. The examples and numerical experiments that have been presented in the paper indicate that the real frequency technique using linear programming can offer reasonable flexibility to the designer. Realizability and design constraints are incorporated in the computer program as a set of linear inequalities. This is naturally built into the linear programming algorithms such as simplex or revised simplex.

Acknowledgment

The author expresses his gratitude to Prof. H. J. Carlin of Cornell University, who originated the Real Frequency technique and conducted this research. Helpful discussions with Dr. L. C. Upadhyayula and Dr. A. Sharma are gratefully acknowledged.

References:

[1] H. J. Carlin, "A New Approach to Gain-Bandwidth Problems," *IEEE Trans.*, **CAS 23**, p. 170, April 1977.
[2] R. E. Griffith and R. A. Stewart, "A Non-linear Programming Technique for Optimization of Continuous Processing Systems," *Management Sci.*, No. 7, p. 378, 1961.
[3] P. Rabinowitz, *SIAM Rev.*, **10**, p. 121, 1968.
[4] R. E. Esch and W. L. Eastman, "Computational Methods for Best Approximation," Tech. Rep. SEG-TR-67-30, Sperry Rand Research Center, 1967.
[5] W. Spendley, G. R. Hext, and F. R. Himsworth, "Sequential Application of Simplex Designs in Optimization and Evolutionary Operation," *Technometrics*, **4**, p. 441, 1962.
[6] Dantzig, *Linear Programming and Extensions*, Princeton University Press, Princeton, NJ (1963).
[7] G. Hadley, *Linear Programming*, Addison-Wesley, Inc. (1970).
[8] S. I. Gass, *Linear Programming*, McGraw-Hill Book Co., NY (1958).

[9] International Mathematical Libraries Subroutines, Inc., 7500 Bellaire Bld., Houston, Texas 77036.
[10] J. J. Komiak, *A Real Frequency Technique for Broadband Matching an Arbitrary Load to a Resistive Generator*, Ph.D. Thesis, 1978, Dept. of Electrical Eng., Cornell University, Ithaca, NY.
[11] H. J. Carlin and P. Amustutz, "On optimum broadband matching," *IEEE Trans.*, **CAS 28**, No. 5, p. 401, May 1981.
[12] G. Matthaei, "Synthesis of Chebyshev Impedance Matching Networks, Filters, and Interstages," *IRE Trans.*, **CT-3**, p. 163, Sept. 1956.
[13] R. Levy, "Explicit Formulas for Chebyshev Impedance Matching Networks, Filters and Interstages," *Proc. IEE* (London), Vol. III, p. 1066, June 1964.
[14] W. K. Chen, "Synthesis of Optimum Butterworth and Chebyshev Broadband Impedance Matching Networks," *IEEE Trans.*, **CAS 24**, p. 152, April 1977.
[15] W. K. Chen and K. G. Kourounis, "Explicit Formulas for the Synthesis of Optimum Broadband Impedance Networks II," *IEEE Trans.*, **CAS-25**, No. 8, p. 609, Aug. 1978.
[16] N. Balabanian, *Network Synthesis*, Prentice Hall, Inc., Englewood Cliffs, NJ, 1958.

Forces Acting on the Tool in VideoDisc Mastering

R. Shahbender
RCA Laboratories, Princeton, NJ 08540

Abstract—The mechanics of cutting a VideoDisc master with an electro-mechanical cutter are considered and expressions are derived for the forces acting on the diamond tool as functions of tool geometry, substrate properties, rake angle, tool-substrate friction angle, and velocity of cutting. The analysis indicates that the tool forces vary linearly with depth of cut for normal recording and quadratically with groove depth for a "fast spiral."

1. Introduction

In recording on a VideoDisc master with an electro-mechanical cutter, average groove depth is established by mechanically adjusting the separation between cutter and disc surface. The desired separation is maintained constant by use of an air-bearing puck that supports the cutter above the disc surface. In principle, this should result in constant average groove depth.[1,2]

The analysis presented in this paper was performed to determine the forces acting on a tool during cutting as an aid to the design of a cutter and its support structure.

2. Mechanics of Cutting

The cutting edges of the diamond tool used in mastering VideoDiscs are orthogonal to the relative velocity vector between tool and work piece only when the rake angle is zero. For nonzero rake angles, the cutting edges are inclined to the velocity vector. To estimate the

cutting forces exerted on a tool, it would therefore be appropriate to consider the mechanics of oblique cutting. The resulting expressions are rather unwieldly and unnecessarily complicated, however, and considerable simplification results if the analysis is restricted to the mechanics of orthogonal cutting.

Results obtained from such an analysis are expected to be reasonably valid, since the inclination of the cutting edges to the velocity vector are fairly small for all rake angles of interest.

Fig. 1 is a sketch of a diamond tool. TD and TB are the cutting edges. For zero rake angle, the projections of TD and TB onto the work surface (TD′ and TB′, respectively) are orthogonal to the velocity vector between tool and work piece. For a nonzero rake angle, TD′ and TB′ are inclined at angles i as shown in Fig. 1. For a tool with an apex angle DTB of 140° and a rake angle α, the inclination angle i is given by

$$i = \tan^{-1}\left(\frac{\sin \alpha}{\tan 70}\right).$$

Thus for small rake angles, the inclination angle is approximately ⅓ the rake angle.

The total force acting on a tool may be obtained by summing the

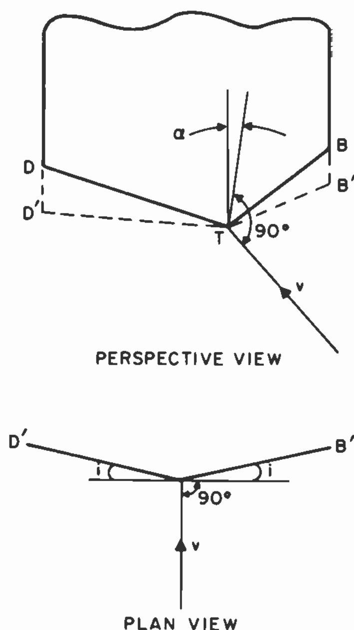

Fig. 1—Inclination angle of tool cutting edges.

forces on each cutting edge. The force on a cutting edge may be decomposed into three components: one component F_P parallel to the velocity vector, a second F_Q perpendicular to the work surface, and a third F_R orthogonal to the first two.

For a symmetrical V-groove cut (fast spiral), the F_P and F_Q components due to each cutting edge are equal and have the same direction. The sum of these components gives the total components acting on a tool. The values obtained for the total components are approximated by those obtained from an orthogonal cutting analysis. The F_R components are equal in magnitude but oppositely directed, resulting in zero lateral (radial) force on a tool.

For normal recording, the cutting edges are subjected to unequal forces. The F_R components are unequal and do not cancel, resulting in a net radial force acting on a tool. By restricting the analysis to orthogonal cutting, the radial force is assumed to be zero, and the other components are approximated.

3. Cutting and Inertia Forces on a Tool

The cutting force on a tool may be calculated using the thin-shear plane model developed by Merchant and Oxley.[3] The inertia reaction force generated by the chip (i.e., the sliver of material cut away to produce the groove) may be added to the cutting force to give the total tool force. Fig. 2 is a sketch showing the basic model assumed by Merchant and Oxley for the analysis of orthogonal cutting. We define

t = depth of cut in work piece (assumed uniform)

V = velocity of work piece (stationary tool)

t_c = thickness of chip

V_c = chip velocity assumed parallel to tool face

α = tool rake angle (the rake angle is shown in Fig. 1)

μ = $\tan\beta$ = coefficient of friction between tool and work piece

β = friction angle determined from μ

R = resultant tool force per unit width of cut

F = friction force on tool face per unit width of cut = $R \sin\beta$

N = normal force on tool face per unit width of cut = $R \cos\beta$

m = chip mass flow per second per unit width of cut.

In the thin-shear-plane model, the cutting force results from the

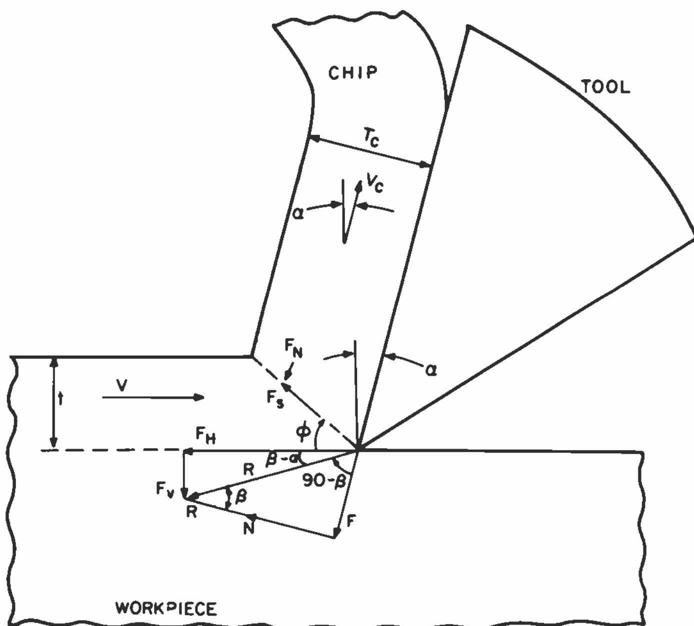

Fig. 2—Geometry of thin-shear-plane model for metal cutting.

workpiece shearing along a plane of constant area inclined at a constant angle. Let

F_S = shear force in shear plane per unit width of cut

F_N = normal force across shear plane per unit width of cut

ϕ = shear plane angle

τ = yield shear strength of workpiece.

The shear force is given by

$$F_S = \tau \times \text{area of shear plane per unit width of cut} \quad [1]$$

$$= \tau t / \sin \phi .$$

The resultant force R may be decomposed into a horizontal component F_H and a vertical component F_V as shown in Fig. 2. These may be expressed in terms of F_s, F_N, and inertial components due to the chip:

$$F_H = \text{cutting force}$$

$$= F_S \cos \phi + m[V - V_C \sin \alpha] + F_N \sin \phi \quad [2]$$

$$= R \cos(\beta - \alpha).$$

$$F_V = \text{thrust force}$$

$$= F_N \cos\phi - mV_C \cos\alpha - F_S \sin\phi \qquad [3]$$

$$= R \sin(\beta - \alpha).$$

From the geometry of Fig. 2, we have

$$t_c = \frac{t}{\sin\phi}\cos(\phi - \alpha). \qquad [4]$$

Conservation of chip mass leads to

$$V_C = \frac{Vt}{t_C} = \frac{V \sin\phi}{\cos(\phi - \alpha)}. \qquad [5]$$

Eqs. [2] and [3] may be manipulated to give F_N. If Eqs. [4] and [5] are substituted into the resulting expression, we obtain

$$F_N = F_S \tan(\phi + \beta - \alpha) + \tan(\phi + \beta - \alpha)\frac{\cos\alpha}{\cos(\phi - \alpha)} mV. \qquad [6]$$

For an orthogonal cut of unit width, depth t, and at a cutting velocity V, the mass flow is

$$m = \rho t V. \qquad [7]$$

where ρ is the density of the workpiece. If Eqs. [1], [6], and [7] are substituted into Eqs. [2] and [3], we obtain

$$F_H = t f_H(\phi, \alpha, \beta, V, \tau, \rho)$$

$$F_V = t f_V(\phi, \alpha, \beta, V, \tau, \rho),$$

where f_H and f_V are functions of the indicated variables and are independent of t.

4. Spiral Groove

For a fast spiral groove, shown schematically in Fig. 3, we have

$$dF = F db = f t db$$

and

$$F_T = \int_{-B}^{+B} f t db = 2f \int_0^D \tan 70\, t dt$$

$$= D^2 \tan 70° f$$

where

dF = element of force for width db of either the horizontal or vertical component

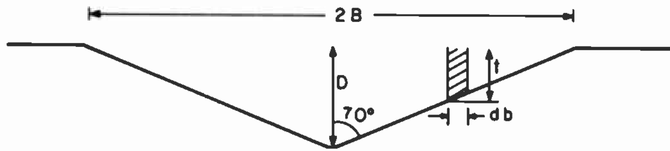

Fig. 3—Geometry of fast spiral groove.

F_T = horizontal or vertical component of tool force

F = horizontal or vertical force, i.e., F_H or F_V per unit width

f = f_H or f_V as given previously

D = depth of groove.

Performing the indicated manipulations leads to F_{HT} and F_{VT}, the horizontal and vertical components of the force exerted by the tool:

$$F_{HT} = D^2 \tan 70 \{\tau[\cot \phi + \tan(\phi + \beta - \alpha)]\} + \rho \frac{V^2 \cos \alpha \cos \phi}{\cos(\phi - \alpha)}[1 + \tan(\phi + \beta - \alpha)\tan \phi] \quad [8]$$

$$F_{VT} = D^2 \tan 70 [\cot \phi \tan(\phi + \beta - \alpha) - 1] \cdot \left[\tau + \rho \frac{V^2 \cos \alpha \sin \phi}{\cos(\phi - \alpha)}\right] \quad [9]$$

Eq. [9] shows that vertical force F_{VT} is zero for $\beta = \alpha$. If the rake angle is greater than the friction angle, i.e., $\beta < \alpha$, then F_{VT} is negative and it requires an upward directed force to keep the tool in a stable position.

The coefficient of static friction μ between diamond and metal[4] is in the range of 0.1 to 0.15. It is not affected by lubrication, and is probably larger than the coefficient of kinetic friction. The corresponding value of β is in the range of 5.7 to 8.5 degrees.

The shear angle ϕ may be determined in a number of ways, as described in the literature.[3] An empirical best fit to a large body of experimental data[3] shows that

$$\phi = 50 - 0.8(\beta - \alpha) \text{ degrees.} \quad [10]$$

The data used in arrriving at the above expression involves conventional machining with conventional tools rather than micro-machining with a diamond tool. Experimental data from Guarracini et al[5] indicate a shear angle of 35 ± 3 degrees for the case of a disc machined with normal grooves (overcut) and a rake angle $\alpha = 0.5$ degrees. This would

imply a relation of the form

$$\phi = 40 - 0.8(\beta - \alpha) \quad [11]$$

as being more appropriate for VideoDisc machining.

The shear strength τ of the copper substrate material is approximately given by

τ = ½ × Ultimate Tensile Strength × (1 + Poisson's ratio).

For standard VideoDisc electrodeposited copper, Dechert and Trager[6] report an average ultimate strength of 1.08×10^5 psi. Poisson's ratio for copper is approximately 0.34. Thus we obtain a value for the shear strength of

$$\tau = 7.24 \times 10^4 \text{ psi}$$
$$= 5.1 \times 10^6 \text{ gm per cm}^2.$$

The density of copper is 8.9×10^3 kg/m^3. At 225 rpm, the cutting velocity is:

$V = 3.45$ m sec^{-1} at an outside radius of 5.76 inch

$V = 1.52$ m sec^{-1} at an inside radius of 2.546 inch

Table 1 lists the computed values of F_{HT} and F_{VT} for the following

Table 1—Horizontal and Vertical Components of Tool Force F_{HT} and F_{VT} in Grams (Outside Radius: Velocity = 3.45 m/sec; Inside Radius: Velocity = 1.52 m/sec)

Groove Depth D (μm)	F_{HT} and F_{VT} for Different Rake Angles α									
	$\alpha = -2°$		$\alpha = -1°$		$\alpha = 0°$		$\alpha = 1°$		$\alpha = 2°$	
	F_{HT}	F_{VT}	F_{HT}	F_{VT}	F_{HT}	F_{VT}	F_{HT}	F_{VT}	F_{HT}	F_{VT}
Coefficient of Friction $\mu = 0.1$, $\tau = 5 \times 10^6$ gm/cm^2										
1	0.33	0.04	0.32	0.04	0.31	0.03	0.31	0.03	0.30	0.02
2	1.31	0.18	1.28	0.15	1.25	0.13	1.23	0.10	1.20	0.08
3	2.94	0.40	2.89	0.34	2.82	0.28	2.76	0.23	2.70	0.18
4	5.23	0.71	5.12	0.60	5.01	0.50	4.91	0.40	4.81	0.31
Coefficient of Friction $\mu = 0.15$, $\tau = 5 \times 10^6$ gm/cm^2										
1	0.35	0.06	0.34	0.06	0.33	0.05	0.33	0.04	0.32	0.04
2	1.39	0.26	1.36	0.23	1.33	0.20	1.30	0.17	1.27	0.15
3	3.13	0.58	3.06	0.51	2.99	0.45	2.93	0.39	2.88	0.33
4	5.56	1.03	5.44	0.91	5.32	0.80	5.21	0.69	5.10	0.58
Coefficient of Friction $\mu = 0.1$, $\tau = 4 \times 10^6$ gm/cm^2										
1	0.26	0.04	0.26	0.03	0.25	0.03	0.25	0.02	0.24	0.02
2	1.05	0.14	1.02	0.12	1.00	0.10	0.98	0.08	0.96	0.06
3	2.35	0.32	2.30	0.27	2.26	0.23	2.21	0.18	2.16	0.14
4	4.18	0.57	4.09	0.48	4.01	0.40	3.93	0.32	3.85	0.25
Coefficient of Friction $\mu = 0.15$, $\tau = 4 \times 10^6$ gm/cm^2										
1	0.28	0.05	0.27	0.05	0.27	0.04	0.26	0.03	0.25	0.03
2	1.11	0.21	1.09	0.18	1.06	0.16	1.04	0.14	1.02	0.12
3	2.50	0.47	2.45	0.41	2.40	0.04	2.34	0.31	2.29	0.26
4	4.45	0.83	4.35	0.73	4.26	0.64	4.17	0.55	4.08	0.47

range of values of the variables:

Depth of groove $D = 1, 2, 3$ and $4\ \mu m$

Coefficient of friction $\mu = 0.1$ and 0.15

Rake angle $\alpha = -2, -1, 0, 1, 2$ degrees

Yield shear strength $\tau = 5 \times 10^6$ and 4×10^6 gm/cm^2

Cutting velocity $V = 3.45$ and 1.52 m sec^{-1}

Shear angle ϕ as given by Eq. [11]

The computed results indicate that the forces F_{HT} and F_{VT} at the outside and inside radii differ only in the third decimal place—i.e., at the milligram level. Thus only one set of values, rounded to 2 decimal places, are tabulated.

5. Normal Recording

Fig. 4a is a sketch of average groove geometry during normal recording. The dotted lines show the cuts made by a diamond tool. The tool force

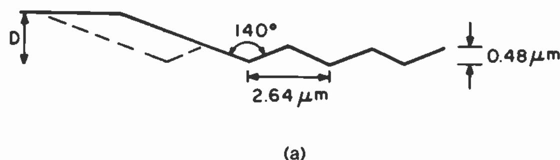

(a)

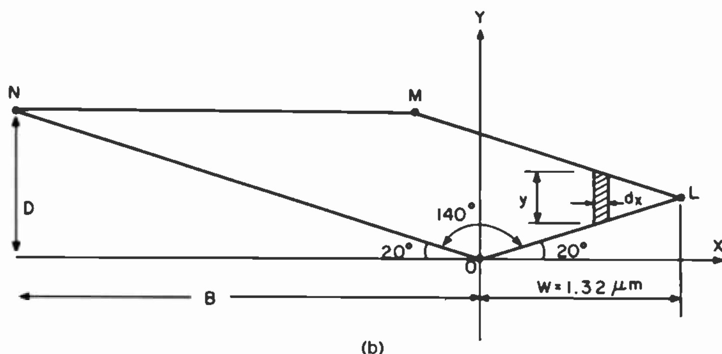

(b)

Fig. 4—Normal recording: (a) average groove geometry and (b) components of tool force.

is given by

$$dF = \int_{-B}^{W} fydx, \qquad [12]$$

where y, dx, W, and B, are defined in Fig. 4b, and dF and f are the same as previously defined. The coordinates of points L, M, and N in Fig. 4b are

$$L \equiv [W, W \tan 20]$$

$$M \equiv [2W - D \cot 20, D]$$

$$N \equiv [-D \cot 20, D]$$

Point M will lie on the Y-axis for

$$D = D_0 = 2W \tan 20 \simeq 0.96\ \mu\text{m}.$$

For all depths of cuts larger than D_0, point M will lie in the second quadrant. Under these conditions, y as a function of X is given by

$$\begin{array}{ll} 0 < X < W & y = 2 \tan 20[W - X] \\ 2W - D \cot 20 < X < 0 & y = 2W \tan 20 \\ -B < X < 2W - D \cot 20 & y = D + X \tan 20. \end{array}$$

Substituting in the above integral leads to

$$F = f\left\{\int_{0}^{W} ydx + \int_{+2W-D\cot 20}^{0} ydx + \int_{-B}^{2W-D\cot 20} ydx\right\} \qquad [13]$$

$$= \{2WD - W^2 \tan 20\} f.$$

Thus, in the case of normal recording, the horizontal and vertical components of the force exerted by the tool F_{HT} and F_{VT} are given by Eqs. [8] and [9] with the term

$$2WD - W^2 \tan 20 = (2.64D - 2.54)$$

substituted for the term $D^2 \tan 70$.

The numerical values of F_{HT} and F_{VT} given in Table 1 may be used provided that each entry is multiplied by the ratio

$$\frac{2.64D - 2.54}{2.75D^2} \text{ where } D \geq 0.96\ \mu\text{m}.$$

Table 2 lists the values of this ratio for $D = 1, 2, 3$, and $4\ \mu$m.

The above expressions indicate that the tool forces are quadratically related to groove depth in a fast spiral cut and linearly related to the depth of cut for normal recording.

Table 2—Ratio of Forces for Normal and Fast Spiral Recording

$D(\mu m)$	1	2	3	4
$\frac{2.64D - 2.54}{2.75\, D^2}$	0.04	0.25	0.22	0.18

6. Conclusions

(1) The tool forces depend quadratically on groove depth for a fast spiral with a horizontal component that is several grams in magnitude and a vertical component that is several hundred milligrams in magnitude.
(2) The tool forces depend linearly on depth of cut for normal recording with a horizontal component that is on the order of 1 gm or less, and a vertical component that is on the order of several tens of milligrams.
(3) The inertial components of tool force at half real speed are small compared to the cutting components of tool force. Thus the tool forces at this speed are relatively independent of the radius at which cutting is occurring.
(4) At a rake angle equal to the friction angle ($\alpha = \beta$), the vertical component of tool force reduces to zero. If the rake angle is greater than the friction angle ($\alpha > \beta$), an upward directed force is required to keep the tool in a stable position.
(5) Recording at real time doubles the value of cutting velocity. This increases the inertial components as the square of the velocity and results in a measurable difference in tool force at inside and outside radii.

Acknowledgments

The author wishes to thank J. Reisner and C. A Whybark for fruitful discussions.

References

[1] J. A. VanRaalte, "VideoDisc Mastering—An Overview," *RCA Review*, **43**, No. 1, p. 5, March 1982.
[2] J. H. Reisner, J. Valachovic, R. E. Simm, and H. I. Moss, "Principles for the Design of Cutters for VideoDisc Recording," *RCA Review*, **43**, No. 1, p. 21, March 1982.
[3] E. J. Armarego, and R. H. Brown, *The Machining of Metals*, Prentice Hall, Inc., N.Y. (1969).
[4] E. Oberg, F. D. Jones, and H. Horton, *Machinery's Handbook*, 21st Edition, Industrial Press, Inc.
[5] J. Guarracini, J. H. Reisner, J. L. Walentine, and C. A. Whybark, "Micromachining VideoDisc Grooves and Signals," *RCA Review*, **43**, No. 1, p. 66, March 1982.
[6] C. A. Deckert, and L. Trager, personal communication.

A Diamond-Like Carbon Film

Joseph Zelez
RCA Laboratories, Princeton, NJ 08540

Abstract—Amorphous, diamond-like carbon films have been produced by cracking N-C_4H_{10} in a glow discharge using ultra pure carbon as the electrodes in a bias sputtering system. Films produced at low or high deposition rates can be in either tensile or compressive stress in the range of 10^7–10^8 dynes-cm^{-2}. A SIMS analysis of the film indicates the presence of <1 at. % H_2. Analysis by ESCA showed the films to be carbon with only trace impurities of O_2, which were most likely on the surface. The bonding structure of this film is being investigated.

The transmittance in the IR spectra as measured from 2.5 to 25 μm is characteristic of an AR coating. The corrected transmittance for the film on an infinite substrate ranges from 0.5489 to 0.99699, while the reflectance ranges from 0.00521 to 0.34843. Other useful properties of the film are that it is highly insulating (10^{14} Ωcm) and has high dielectric strength, extreme hardness, and chemical inertness. Potential applications of this film as a protective coating for semiconductors, high-energy lasers, and plastic lenses are discussed briefly.

Introduction

Diamond-like carbon films have been made by low-energy carbon ion-beam deposition,[1] rf plasma decomposition from a hydrocarbon gas such as butane[2–8,13] or other alkanes,[9] and by ion plating and dual ion beam techniques.[10–12] We have developed a hybrid process that can be used to deposit thin films of diamond-like carbon on such substrates

as Si, SiO_2, Al, Al_2O_3, KBr, NaCl, ZnMn, GaAs, InP, stainless steel, plastics and paper.

The diamond-like carbon films were prepared by cracking normal butane under widely different discharge conditions. This resulted in films with low tensile or compressive stress.

Experimental

The process chamber used for depositing the films is shown in Fig. 1. The rf system consists of two water-cooled ultrapure parallel-plate carbon electrodes with variable separation. They are capacitively coupled to an rf-bias sputtering generator.[14] The upper electrode is 15.2 cm in diameter and the bottom electrode, on which the substrates

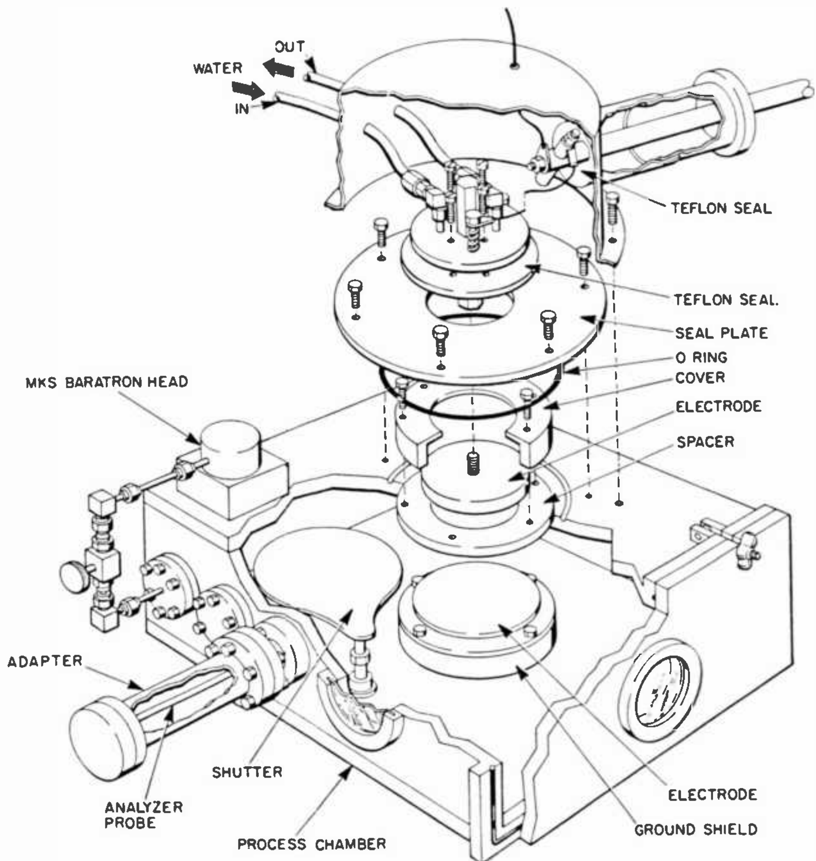

Fig. 1—Process chamber for producing amorphous, diamond-like film.

to be coated were placed, is 22.9 cm in diameter. Both electrodes are 0.635 cm thick.

The stainless steel process chamber is evacuated down to 10^{-6} Torr by an oil diffusion pump backed by a two-stage rotary oil pump. The normal butane is then leaked into the system and the pressure is raised to 8×10^{-4} Torr. The high-vacuum valve is throttled to maintain the operating pressure gradient between the process chamber and the diffusion pump, the operating pressure being in the range of 25 to 70 mTorr as measured on an MKS Baratron. The rf power is then applied to the pair of electrodes with the lower electrode biased in the range of 0 to −100 volts and the upper electrodes biased in the range of −200 to −2500 volts. The normal butane is 99.99% pure, its impurities being iso-butane and N_2. The discharge is excited at various target potentials, and a film is deposited onto the substrates at rates varying between 8 to 360 Å/min.

The process-chamber integrity is monitored using a UTI/100C Residual Gas Analyzer and Computer Display System.

Results

The films prepared by this hybrid process, as well as those prepared by other researchers, are chemically inert against acids and alkalis, and have excellent adhesion to Si.

Film densities ranging from 1.9–2.67 g/cc have been obtained by others. The densities of films deposited in various thicknesses on microsheet glass were measured gravimetrically and found to average about 2.7 g/cc.[5,9]

SIMS has been used to determine chemical composition by the composition of fragment ions. The diamond-like film contains <1 at. % H_2. AES could not be performed on these films because of charging produced by the electron beam on the highly-insulating diamond-like film. ESCA showed the films to be carbon with only trace impurities of O_2. It was determined by TEM that the diamond-like film is amorphous. Typical values of film stress are listed in Table 1. The stress was measured by depositing the film on one side of a microsheet glass (2.54 cm diameter by 0.007 cm thick) and measuring the amount of deflection of the disc from a flat surface. The stress G_T can be related to the deflection by the disc at a distance r from the center of the disc by the equation

$$G_T = \frac{\sigma E_s t_s^2}{3(1-\nu)t_f r^2},$$

where σ is the amount of deflection in the coated disc, E_s is the Young's

Table 1—Values of Film Stress

No.	Upper Electrode Potential (Volts)	Lower Electrode (Substrate-Target) Potential (Volts)	Film Thickness (μm)	Film Stress (T = Tensile C = Conpressive) (Dyne/cm²)
1	−450	−50	1.44	7.0×10^7(T)
2	−450	−50	0.72	2.8×10^7(T)
3	−450	−50	1.50	2.0×10^7(T)
4	−400	−50	0.42	3.2×10^8(T)
5	−400	−50	2.75	9.0×10^8(T)
6	−400	−50	0.82	9.6×10^8(T)
7	−350	−50	0.25	6.0×10^8(T)
8	−350	−50	1.00	1.2×10^8(T)
9	−300	−50	0.22	1.5×10^8(C)
10	−250	−50	0.18	3.9×10^8(C)
11	−250	−50	0.08	7.5×10^8(C)

modulus of the disc, t_s is the disc thickness, ν is the Poisson's ratio of the disc, t_f is the thickness of the diamond-like film, and r is the disc radius.

Observations on deposited films indicate that the carbon films possess very high internal stress that may be caused by tilted tetrahedral bonds and/or by H_2 or residual gas inclusions.[10]

Diamond-like films are able to scratch glass and to resist scratching by glass and metal.[2] Diamond-like film hardness has been measured using a Vickers microhardness pyramid indentor. However, others consider quantitative hardness tests using conventional diamond indentations problematic.[10]

Functional tests were applied to the diamond-like film produced by the hybrid process. Fig. 2 illustrates type 304 stainless steel writing tubes whose smallest diameter was coated with a 5-μm-thick film. A

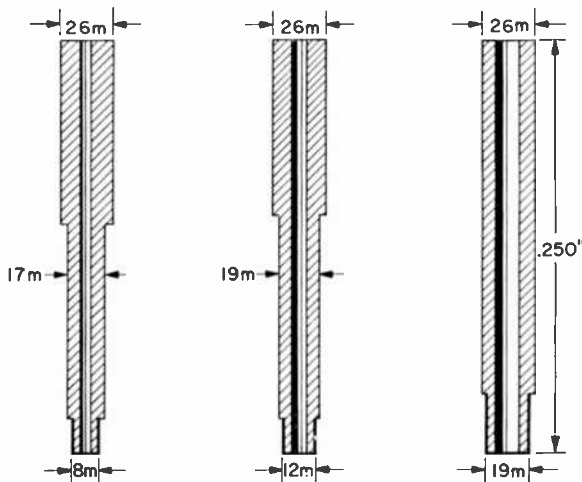

Fig. 2—Writing tubes to measure film adhesion and hardness.

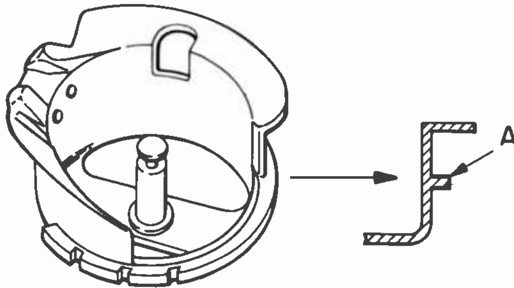

Fig. 3—Hook Component A for industrial bobbin.

35 g weight is applied to the tubes, causing them to strike a drum of Mylar drafting paper; the writing tubes are then tilted to an angle of 60°. Rotating the drum slowly (approximately 1 rpm) the tube travels a distance of 100 meters. After the test is terminated, the film is examined for adhesion and erosion. It was concluded that the film could not flex with the 8 mil diameter tube and eroded away after 13 meters. The 12 mil diameter tube offered some improvement (an additional 12 meters) and the 19 mil diameter tube performed repeatedly.

The hook components shown in Figs. 3 and 4 are mates that make up an industrial sewing machine bobbin. Areas A and B were coated with a film 4-kÅ thick. When the bobbin was threaded and rotated at 7000-10,000 rpm, the diamond-like film eliminated the need for oil lubricants and reduced the wear at edges A and B.

The entire magnetic head component shown in Fig. 5 was coated with a 400-Å-thick diamond-like film. The main area of interest is the ZnMn ferrite located at the outer edge. Various tapes have been used in the video cassette recorder and there is no evidence of film damage.[15]

Diamond-like films are electrically insulating.[1,2,4,5,9,12] Table 2 lists some electrical properties of a 1260 Å-thick film deposited on an aluminized Si wafer. Note the high resistivity, and breakdown voltage.

Diamond-like carbon films have been reported to have refractive

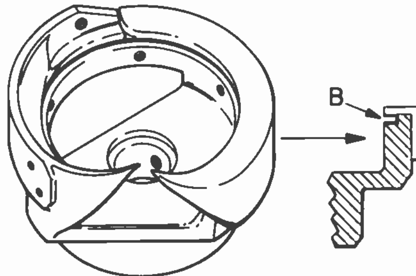

Fig. 4—Hook Component B for industrial bobbin.

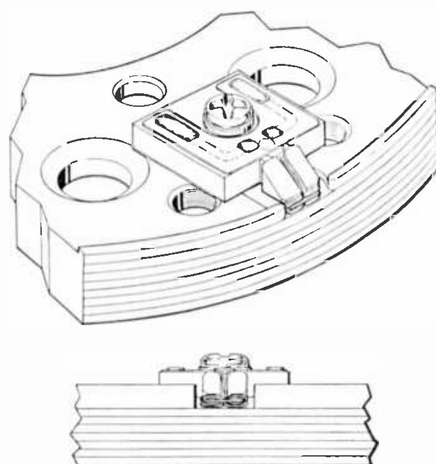

Fig. 5—Magnetic head component—VCR.

indices from 1.8–2.8.[1-3,11,13] Values of the refractive index for our films were calculated from the measured reflectance R and transmittance T of a film-Si substrate composite. Because Si has a high refractive index, corrections for reflection losses in the calculations tend to introduce significant errors that were evident from the sum of R and T. Therefore, only an approximate value of the refractive index in the infrared was obtained (2.0–2.4) from 2.5 to 25 μm.

Figs. 6 and 7 show the transmittance and reflectance of a typical film in the infrared. The films are completely transparent in the visible spectrum. The films exhibit, to varying degrees, absorption by an aliphatic hydrocarbon. The (CH_2, CH_3) modes at 2870, 2920, 2960, 1420, 1375 cm^{-1} are evident. In addition, two weak modes are present at 1080 and 1720 cm^{-1}, which are associated with O_2-containing func-

Table 2—Electrical Properties of 1260Å Thick Film

tan δ 10 kHz	ϵ	$\rho \times 10^{14}$ $\Omega - cm$	$E_d \times 10^7$ V/cm
0.0076	8.7	1.49	3.6
0.0074	8.7	1.51	3.6
0.0074	8.9	1.47	3.6
0.0081	8.8	1.51	3.6
0.0074	8.8	1.48	3.6
0.0073	8.7	1.47	3.6
0.0075	8.9	1.50	3.6

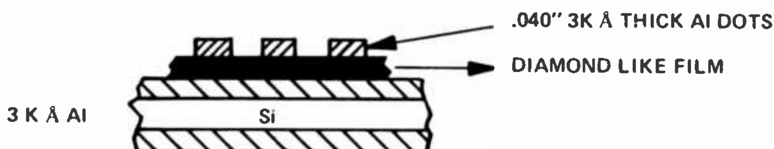

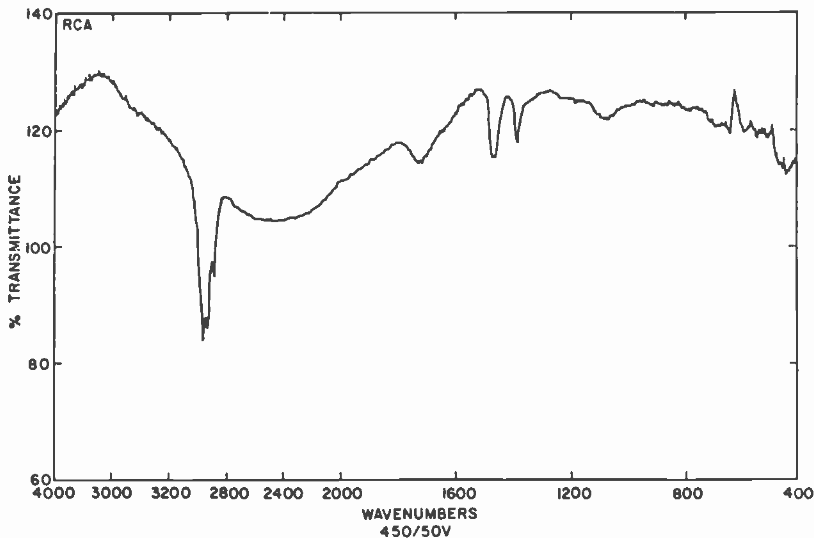

Fig. 6—Transmittance of a diamond-like film 9200 Å thick in *IR*. Upper electrode at −450V and lower electrode at −50V.

tional groups. The band at 1720 cm^{-1} is characteristic of a carbonyl functional group, while the band at 1080 cm^{-1} is probably related to an ether or ester functional group. These may form when the coated Si wafer is in an ambient, i.e., it may have a reactive surface. The transmittance is characteristic of an AR coating. This is evident from the reflectance data.[16]

A 3000-Å thick film was deposited on a quartz disc to measure the energy bandgap. The Tauc model for an amorphous film was followed. In this model, the square root of the absorption (α) and the photon energy (eV) product is plotted versus the photon energy to obtain the energy gap (Fig. 8). For a crystalline indirect-bandgap semiconductor only the square root of α is plotted versus eV. The plot in Fig. 8 obtained by the Tauc model indicates the bandgap of the film is on the order of 3 eV.[16]

The amorphous diamond-like film has possible high-energy-laser applications (e.g., as chemically inert encapsulants for coated optics). Damage thresholds for this film were measured using a pulsed chemical laser. Generally, for films deposited by techniques other than the hybrid process described here, the damage thresholds are low, reflecting problems of stress (delamination) or absorption (low melt and erosion thresholds). The diamond-like film had a melt threshold that was comparable to those seen for crystalline Si and showed no tendency to delaminate. The film had a minimal OH-absorption band (which occurs at the laser wavelength) and also low stress. The laser

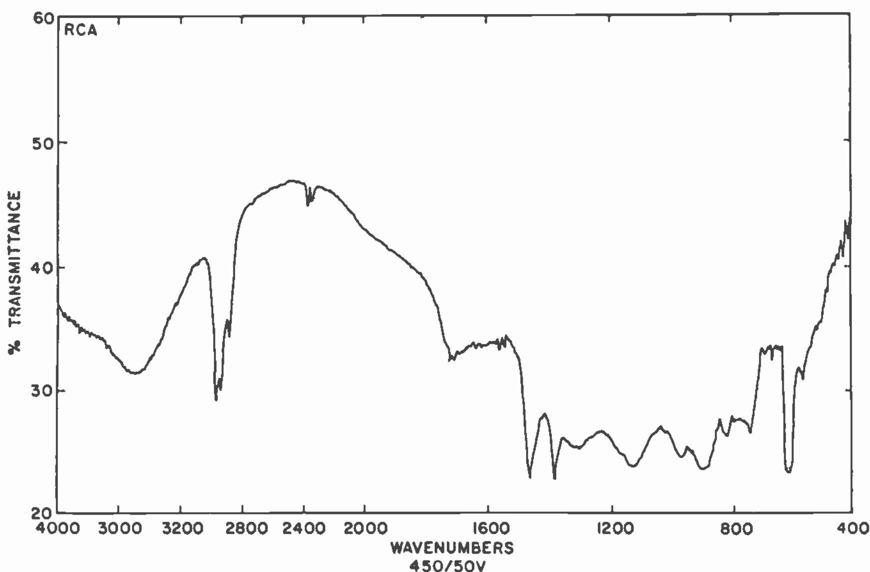

Fig. 7—Reflectance of a diamond-like film 9200 Å thick in *IR*. Upper electrode at −450V and lower electrode at −50V.

test is encouraging in that it suggests the film can be deposited so as to survive thermal shock.[17]

The diamond-like films were deposited on one or both surfaces of polystyrene, polycarbonate, methyl methacrylate, and custom resin 39 lenses to thickness of $\lambda/2$ at 5500 Å. Lens transmission is increased 6–17%. The film passed the Scotch tape and rubber eraser tests, thus

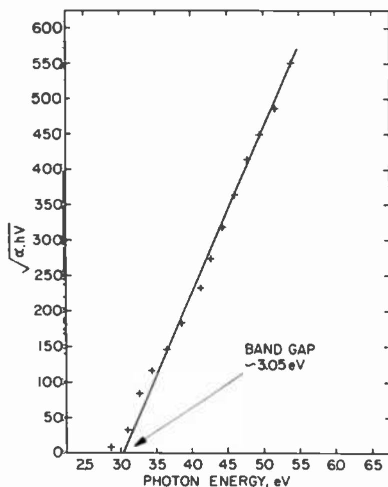

Fig. 8—Tauc model for measuring energy bandgap.

proving that it can be used not only as an AR coating but also as a protective coating for plastic lenses.

Conclusions

It has been shown that a low stress, highly insulating diamond-like film can be produced using N-butane and ultrapure carbon electrodes in a hybrid process. The film has excellent optical properties when applied to glass or plastic substrates. Further studies will include the possibility of N or P type doping, and a measurement of the temperature coefficient of conductivity of the film.

Acknowledgments

The author wishes to acknowledge the assistance of Charles W. Magee and Joseph T. McGinn for the SIMS, RHEED, and TEM analysis. The IR spectra and some of the visible spectra were taken by Peter Zanzucchi and William R. Frenchu. Fred J. Tams, III, aluminized the Si wafers for the films' electrical property measurements. In addition, I am indebted to John L. Vossen for his critical review of this manuscript.

References

[1] S. Aisenberg and R. Chabot, "Ion-Beam Deposition of Thin Films of Diamond-Like Carbon," *J. Appl. Phys.*, **42**, p. 2953 (1971).
[2] S. M. Ojha and L. Holland, "Some Characteristics of Hard Carbonaceous Films," *Thin Solid Films*, **40**, p. L31 (1977).
[3] L. Holland and S. M. Ojha, "Infrared Transparent and Amorphous Carbon Grown Under Ion Impact in Butane Plasma," *Thin Solid Films*, **48**, p. L21 (1978).
[4] S. Berg and L. P. Anderson, "Diamond-Like Carbon Films Produced in a Butane Plasma," *Thin Solid Films*, **58**, p. 117 (1979).
[5] S. M. Ojha, H. Norström, and D. McCulluch, "The Growth Kinetics and Properties of Hard and Insulating Carbonaceous Films Grown in an RF Discharge," *Thin Solid Films*, **60**, p. 213 (1979).
[6] T. Banno, T. Ito, S. Baba, and A. Kinbara, "Sputtering of Carbon Coatings," *Proc. 8th Internl. Vac. Cong.*, Vol. 1 (F. Abeles and M. Croset, Eds.), Societe Francaise du Vide, Paris (1980), pp. 46–49.
[7] A. Alnaimi and S. Berg, "Adhesion Properties of Carbon Films," *Proc. 8th Internl. Vac. Cong.*, Vol. 1 (F. Abeles and M. Croset, Eds.), Societe Francaise du Vide, Paris (1980), pp. 336–339.
[8] H. Vora and T. J. Moravec, "Structural Investigation of Thin Films of Diamond Like Carbon," *J. Appl. Phys.*, **52**, p. 6151 (1981).
[9] L. P. Anderson, S. Berg, H. Norström, R. Olaison, and S. Towta, "Properties and Coating Rates of Diamond-Like Carbon Films Produced by RF Glow Discharge of Hydrocarbon Gases," *Thin Solid Films*, **63**, p. 155 (1979).
[10] Chr. Weissmantel, C. Schürer, F. Fröhlich, P. Grau, and H. Lehman, "Mechanical Properties of Hard Carbon Films," *Thin Solid Films*, **61**, p. L5 (1979).
[11] P. G. Turner, R. P. Howson, and C. A. Bishop, "Preparation and Optical Properties of Transparent Carbon Films Prepared in Various Hydrocarbon Atmosphere RF Plasmas," *Inst. Phys. Conf.*, Ser. No. 54, Chapt. 6, p. 229.

[12] B. A. Banks and S. K. Rutledge, "Ion Beam Sputter Deposited Diamond-Like Films," NASA TM-82873 (1982).
[13] A. Bubenzer, B. Dischler, and A. Nyaiesh, "Optical Properties of Hydrogenated Hard Carbon Films," *Thin Solid Films*, **9**, p. 81 (1982).
[14] J. L. Vossen and J. J. O'Neill, "Ultra-stable System for RF Sputtering with RF-Induced Substrate Bias," *J. Vac. Sci. Technol.*, **12**, p. 1052 (1975).
[15] Private communication, Yoshiharu Namba, Univ. of Osaka, Osaka, Japan.
[16] Private communication, Peter Zanzucchi.
[17] Private communication, Terry M. Donovan, Dept. of the Navy, Naval Weapons Center, China Lake, Calif.

Sine-Wave Threshold Contrast-Sensitivity Function: Dependence on Display Size*

C. R. Carlson
RCA Laboratories, Princeton, NJ 08540

Abstract—Threshold contrast-sensitivity measurements were obtained using sine-wave gratings with the size of the displayed field as a parameter. It was found that for frequencies above roughly 1 cycle/degree, relative contrast sensitivity is determined by a fixed number of cycles in the displayed field. For frequencies below 1 cycle/degree, relative performance is not predicted by a fixed number of cycles. Additionally, the low-frequency roll-off in the shape of the contrast-sensitivity function was maintained for all display sizes measured. Extrapolation of the measured results indicates that no significant modification in the shape of the contrast-sensitivity function is expected for displays greater than 60 degrees in diameter.

1. Introduction

The threshold contrast-sensitivity function for spatial sine-wave gratings is strongly dependent on the size of the sine-wave field used to perform the measurements.[1-8] This fact is not surprising if the detection processes of the human visual system are capable of spatial integration over finite visual areas. Hoekstra et al.[4] and Savoy and McCann[5] reported that the visibility of gratings below roughly 7 cycles/degree is determined by a critical number of cycles in the display field. They found that when the display field contains more than 5 to 10 cycles of

* Research supported by the Office of Naval Research under Contract No. N00014-74-C-0184.

a grating at a specific spatial frequency, there is no improvement in contrast sensitivity. Earlier, McCann et al.[6] reported that at low spatial frequencies the detection threshold of sine-wave gratings is dependent primarily on the number of cycles in the display field. Furthermore, they found that, for spatial frequencies below approximately 3 cycles/degree, the threshold is independent of spatial frequency. Similar results were also reported by Hoekstra et al.[4]

These results led these workers to conclude that the low-frequency roll-off of the human visual contrast-sensitivity function is due to the inadequate number of displayed cycles in the measurement fields at low spatial frequencies. Although we agree that under certain conditions this effect can contribute to the low-frequency roll-off,[7] we feel that it is extremely unlikely that the low-frequency roll-off is entirely due to the finite number of displayed cycles. This result is contrary to such well-known psychophysical effects as Mach bands,[8] and, more importantly, to the neurophysiological studies that indicate a center-surround organization of the receptive fields in the mammalian retina.[9] These studies suggest that the visual system should exhibit some attenuation of low spatial frequencies.

In this paper we present the results of measurements on the effect of display size on the contrast-sensitivity function. We show that at low spatial frequencies contrast sensitivity is related in a simple, continuous fashion to the number of cycles in the display field. Furthermore, we show that for spatial frequencies below 3 cycles/degree contrast sensitivity is not exclusively a function of the number of cycles in the display field. Most importantly, we show that the low-frequency roll-off in the contrast-sensitivity function is not eliminated when the display contains an arbitrarily large number of cycles at low spatial frequencies.

2. Experimental Situation

The sine-wave gratings used in this investigation were generated on two separate apparatus. Experiments involving the large display formats and low spatial frequencies were performed using an optical projection system; those involving small display formats and high spatial frequencies were performed using a Tektronix 631 TV monitor. Additional details about the construction and performance of these systems are given elsewhere.[11,12]

In terms of viewing angle, the display diameters investigated with the TV monitor were 0.5°, 1.0°, 2.3°, and 6.5°. Display diameters of 6.5° and 60° were investigated using the optical projection system.

The results of the 6.5° display measurements obtained using both systems were in good agreement.

All measurements were made at threshold with vertical gratings at a mean display luminance of 34 mL. The luminance of the area surrounding the display was 3.4 mL, and the viewing distance for all experiments was 190 cm. Binocular vision was employed without artificial pupils. The contrast of the gratings was defined in the conventional manner to be the maximum minus the minimum grating luminance, divided by the sum of the maximum and minimum grating luminance.

The measurements were performed on two subjects, C.R.C. and R.I. Each grating was presented continuously on the screen until its threshold was determined by the method of adjustment. Ten readings were taken at each spatial frequency for each observer, and the results were averaged. The observers viewed the screen by allowing their eyes to wander slowly about a small region in the center of the display. This technique replicates normal viewing conditions and was also found to give more consistent results.

3. Experimental Results

The results of this study are shown in Fig. 1. The solid lines on the figures represent smooth fits to the experimental data points. This set of curves clearly shows the strong functional dependence between contrast sensitivity and display size. At high spatial frequencies contrast sensitivity is independent of display size for displays greater than approximately 2.3° in diameter. For displays smaller than this value, contrast sensitivity is reduced, even for the highest spatial frequencies measured. We believe that this reduction in sensitivity is realized because three factors become more significant as the display is made smaller: (1) the number of cycles across the display is reduced;[1-8] (2) the vertical extent of the display is diminished;[8] and (3) the difference between the display luminance and the surround luminance has a relatively greater influence.[9,11] For the conditions of this experiment, only the finite number of cycles across the display plays an important role in modifying the contrast sensitivity function for displays above roughly 2.0° in diameter.[3,4,8,9,11]

At low spatial frequencies the contrast-sensitivity function exhibits the strong functional dependence on display size mentioned previously. However, it can be seen from the curves that even for the 60° diameter display the peak in the contrast-sensitivity function is maintained. These results show no indication of a flattening in the response curves at low spatial frequencies, as predicted by Hoekstra et al.[4] and by

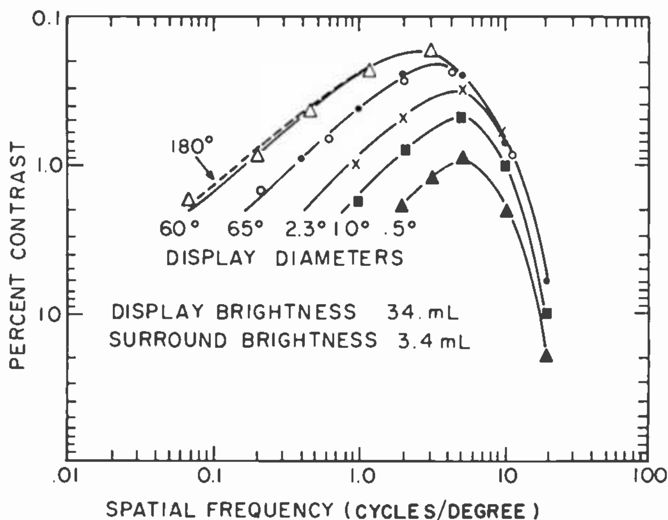

Fig. 1—Threshold contrast-sensitivity measurement results as a function of spatial frequency with display diameter as the parameter. The viewing distance was 190 cm, and binocular vision without artificial pupils was used. The dashed line indicates the predicted contrast sensitivity function for a display subtending 180 degrees.

Savoy and McCann.[5] The results of Fig. 1 have been replotted in Fig. 2 to indicate more clearly the relationship between contrast sensitivity and the number of cycles, N, in the display field. This figure shows that for displays with diameters less than 6.5°, there is a low-frequency regime where contrast sensitivity is roughly described by the number of cycles in the measurement field. However, this relationship clearly breaks down for the largest display size measured.

In order to answer the question of whether the low-frequency roll-off would eventually be eliminated for even larger displays, we have plotted in Fig. 3 the spatial frequency, f_c, at which the contrast sensitivity functions of Fig. 1 intercept the 1% contrast line at low spatial frequencies as a function of inverse display diameter, $1/D$. The experimental data is well described by the simple formula

$$f_c = 0.15 + 1.59/D. \quad [1]$$

The important feature of this curve is that the intercept for $D = 180°$ is safely above the origin. That is, the low-frequency attenuation will be maintained even for a display subtending 180° of visual angle. Indeed, the expected change in going from the 60° diameter display to a larger display is negligible. Further, there is no indication from these data points that an alternative interpretation is possible. In Fig. 1 we

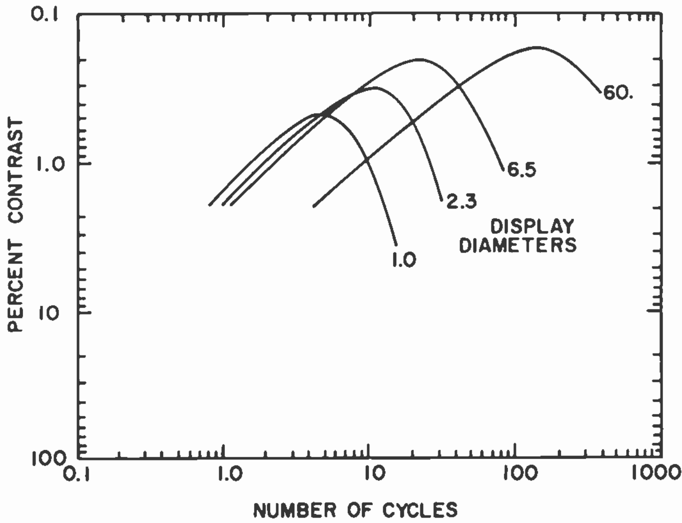

Fig. 2—The results of Fig. 1 replotted as a function of the number of cycles across the display field.

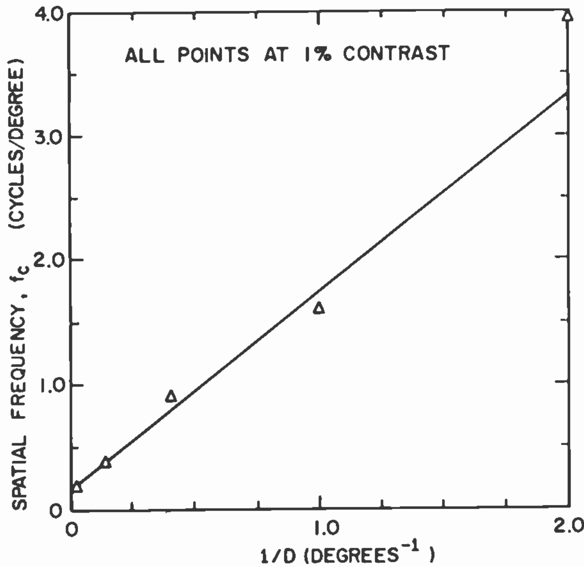

Fig. 3—The spatial frequency, f_c, at which the low frequency portions of the curves in Fig. 1 intercept the 1% contrast line as a function of inverse display diameter, $1/D$. The solid line on the figure is given by $f_c = 0.15 + 1.59/D$.

have plotted, as a dashed line, the expected contrast-sensitivity function for an infinite display.

From the data of Fig. 1 we have also determined the relationship between contrast sensitivity and the size of the display field at specific spatial frequencies. These results are shown in Fig. 4 for the spatial frequencies of 0.7, 1.0, and 3.0 cycles/degree. It can be seen that when the data are plotted as a function of the inverse display diameter, the results are well approximated by linear functions. At 3.0 cycles/degree the appropriate analytical expression is

$$m_T = 0.17 + 0.41/D. \quad [2]$$

Our results can be replotted to show that the relative attenuation in contrast sensitivity at each spatial frequency is not determined by a fixed number of cycles in the display field. This conclusion is summarized in Fig. 5 for spatial frequencies between 0.3 and 10 cycles/degree. The ordinate represents the number of cycles, at a given spatial frequency, necessary to realize 50% of the contrast sensitivity that would be obtained for a display containing an infinite number of cycles. Several conclusions can be obtained from this figure. First, for spatial frequencies up to 3 cycles/degree, the number of cycles necessary to reach a given level of attenuation is not constant. For example, at 0.3 cycle/degree, the 50% attenuation point is realized with only 3 cycles across the display; at 3.0 cycles/degree, 7 cycles are required. Second, as observed by Hoekstra et al.[4] and by Savoy and McCann,[5] in the

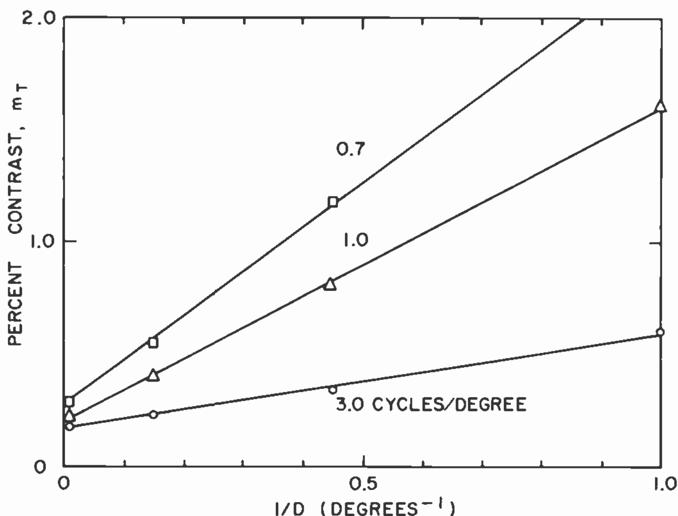

Fig. 4—The results of Fig. 1 replotted to show the relationship between contrast sensitivity and inverse display diameter for sine-wave gratings at 0.7, 1.0, and 3.0 cycles/degree.

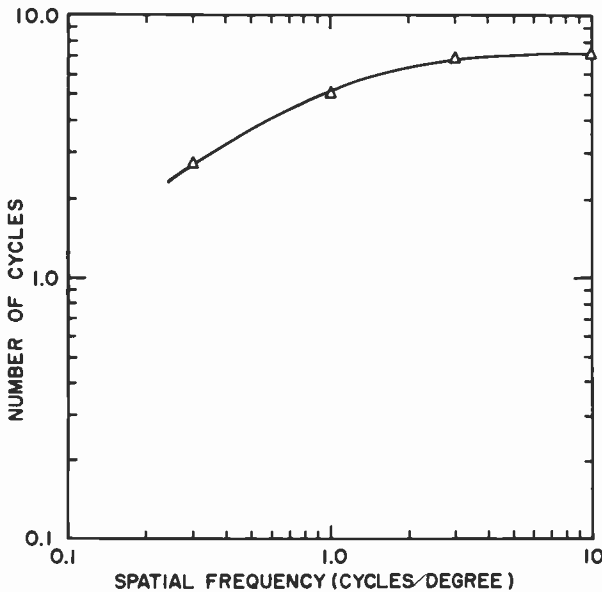

Fig. 5—The number of cycles in the measurement field required to obtain 50% of the maximum contrast sensitivity at a given spatial frequency, as a function of spatial frequency.

range of spatial frequencies between 3.0 and 10 cycles/degree, a fixed number of cycles does adequately describe the threshold detection process. Although we cannot extrapolate our results past 10 cycles/degree (due to the area-size and surround-brightness effects mentioned previously), other workers have found that the "critical" number of cycles at higher spatial frequencies is still roughly between 5 and 10 cycles.[1,2] It has been shown recently that such behavior is consistent with an imaging system that preserves the shape of the images independent of their size.[13,14]

Finally, we note that the results presented above reflect indirectly on the question of whether the visual system processes low spatial frequency information. As Kelly[15] has pointed out, the number of cycles necessary for a truncated sine-wave grating to act as an effective approximation to an infinite target is roughly 7. This is because for gratings containing a smaller number of cycles, the spectral extent of the gratings is comparable to the frequency of the grating. As we have shown, for frequencies below approximately 1.0 cycle/degree, the critical number of cycles (defined at 50% of maximum contrast sensitivity) falls off sharply. Therefore, we conclude that the lowest spatial frequencies of images cannot play an important role in visual processing.

4. Conclusions

In conclusion, we have shown that there exists a low spatial frequency roll-off in the human threshold contrast sensitivity function that is independent of display size. This conclusion is also supported by the research of Estévez and Cavonius.[7] We have also shown that the visibility of gratings at low spatial frequencies can not be described simply by a constant number of cycles in the display field. Our results and conclusions differ from those of Hoekstra et al.[4] and Savoy and McCann[5] because of the wide range of display sizes we used to perform our experiments. In limiting experiments to smaller display sizes, it is possible to misinterpret the limiting relationship between display size and contrast sensitivity because the constant term of Eq. [1] is small compared with the term proportional to $1/D$. And finally, we have determined the full visual threshold contrast-sensitivity function that is independent of display size effects. It is this function that should be used as the describing function for the human visual system for sine-wave gratings at threshold.

Acknowledgment

I wish to thank R. W. Cohen, I. Gorog, and R. Infanti for their assistance throughout the course of this work.

References

[1] T. W. Coltman and A. E. Anderson, "Noise Limitations to Resolving Power in Electronic Imaging," *Proc. IRE*, **48**, p. 858 (1960).
[2] J. M. Findlay, "A Spatial Integration Effect in Visual Acuity," *Vision Res.*, **9**, p. 157 (1969).
[3] H. A. W. Schober and R. Hilz, "Contrast Sensitivity of the Human Eye for Square-Wave Gratings," *J. Opt. Soc. Am.*, **55**, p. 1086 (1965).
[4] J. Hoekstra, D. P. van der Goot, G. van den Brink, and F. A. Bilsen, "The Influence of the Number of Cycles Upon the Visual Contrast Threshold for Spatial Sine Wave Patterns," *Vision Res.*, **14**, p. 365 (1974).
[5] R. L. Savoy and J. J. McCann, "Visibility of Low-Spatial-Frequency Sine-Wave Targets: Dependence on Number of Cycles," *J. Opt. Soc. Am.*, **65**, p. 343 (1975).
[6] J. J. McCann, R. L. Savoy, J. A. Hall, Jr., and J. J. Scarpetti, "Visibility of Continuous Luminance Gradients," *Vision Res.*, **14**, p. 917 (1974).
[7] O. Estévez and C. R. Cavonius, "Low Frequency Attenuation in the Detection of Gratings: Sorting Out the Artifacts," *Vision Res.*, **16**, p. 497 (1976).
[8] E. R. Howel and R. F. Hess, "The Functional Area for Summation to Threshold for Sinusoidal Gratings," *Vision Res.*, **18**, p. 369 (1978).
[9] F. M. Lowry and J. J. DePalma, "Sine-Wave Response of the Visual System. I. The Mach Phenomenon," *J. Opt. Soc. Am.*, **51**, p. 422 (1961).
[10] R. L. DeValois, "Central Mechanisms of Color Vision," from *Handbook of Sensory Physiology*, Vol. VIII-3 (R. Tung, ed., Springer-Verlag, NY, 1973) p. 210.
[11] R. W. Cohen, I. Gorog, and C. R. Carlson, *Image Descriptors for Displays*, Technical Report for the Office of Naval Research, Contract No. N00014-74-C-0184, Jan. 1975.
[12] R. W. Cohen, C. R. Carlson, and G. D. Cody, *Image Descriptors for Displays*, Technical Report for the Office of Naval Research, Contract No. N00014-75-C-0184, Jan. 1976.

[13] C. R. Carlson, R. W. Klopfenstein, and C. H. Anderson, "Spatially Inhomogeneous Scaled Transforms for Vision and Pattern Recognition," *Opt. Lett.*, **6**, p. 386 (1981).
[14] R. W. Klopfenstein and C. R. Carlson, "Theory of Shape-Invariant Imaging Systems," submitted for publication to *J. Opt. Soc. Am.*
[15] D. H. Kelly, "How Many Bars Make a Grating," *Vision Res.*, **15**, p. 625 (1975).

Patents Issued to RCA Inventors—Third Quarter 1982

July

D. E. Carlson Fabricating Amorphous Silicon Solar Cells by Varying The Temperature of The Substrate During Deposition of The Amorphous Silicon Layer (4,339,470)
S. Chio Shank Diamond Cleaning (4,339,281)
S. Chio and G. A. Kim Stylus Tip Fabrication From a Synthetic Diamond Stone (4,340,954)
P. J. Coyle Method for Interconnecting Solar Cells (4,340,803)
R. C. Dennison and J. M. Walter Synchronizing System with Chroma Parity Detection (4,339,770)
A. Goldman Etching Method Using a Hardened PVA Stencil (4,339,528)
A. Goldman Etching Method Using a PVA Stencil Containing N-Methylol Acrylamide (4,339,529)
I. Gorog, M. A. Leedom and J. P. Wittke Method and Apparatus for Positioning a Tapered Body (4,341,472)
P. E. Haferl Vertical Deflection Circuit (4,338,549)
J. R. Hale Beading Apparatus for Making an Electron Gun Assembly Having Self-Indexing Insulating Support Rods (4,341,545)
R. R. Handel CRT with ARC Suppression Means Therein (4,338,543)
J. R. Harford Television Intermediate Frequency Amplifier with Feedback Stabilization (4,342,005)
L. J. Hillenbrand, J. R. Preston and D. A. Berry High Density Information Disc (4,340,629)
J. V. Howard Television Deflection Yoke Mount (4,338,584)
G. John, P. M. Heyman and D. P. Bortfeld Variable Pitch Grooved Label for VideoDisc (4,341,952)
G. Kaganowicz and J. W. Robinson Method of Coating Substrates with an Abrasive Layer (4,339,471)
K. C. Kelleher Processor Controlled VideoDisc Servo System (4,340,949)
N. R. Landry Short Horn Radiator Assembly (4,338,609)
L. J. Levin Optical Recording Medium with a Thick Overcoat (4,340,959)
D. D. Mawhinney Vehicle Identification System (4,339,753)
A. F. McDonie and W. K. Miller Method of Making Potassium, Cesium, Rubidium, Antimony Photocathode (4,339,469)
E. A. Miller RF Heating Coil Construction for Stack of Susceptors (4,339,645)
M. E. Miller Minimum Tracking Force Stylus (4,340,956)
M. Packer and O. D. Black Coated Printed Circuit Wiring Board and Method of Soldering (4,340,167)
T. R. Pampalone Aqueous Developable Poly(Olefin Sulfone) Terpolymers (4,341,861)
J. I. Pankove Method for Fabricating Adjacent Conducting and Insulating Regions in a Film By Laser Irradiation (4,339,285)
A. Presser Electronically Tunable Resonator Circuit (4,338,582)
J. J. Prusak and M. L. Whitehurst Apparatus for Electroforming (4,341,613)
D. J. Sauer Differential Amplifier Having a Low-Pass Characteristic (4,342,001)
J. D. Shearer Solder Draw Pad (4,339,784)
M. C. Stewart Carriage Alignment Apparatus for VideoDisc Player (4,342,109)
R. G. Stewart Noise Protection Circuits (4,339,809)
D. J. Tamutus Method of Fabricating a Color-Selection Structure for a CRT (4,341,591)
M. Toda and S. Osaka Rotative Motor Using a Piezoelectric Element (4,339,682)
C. M. Tomasetti, M. D. Harsh and A. F. McDonie Method for Stabilizing the Anode Sensitivity of a Photomultiplier Tube (4,341,427)
R. Torres and J. G. Henderson Automatic Tuning Circuit Arrangement with Switched Impedances (4,339,827)
J. A. van Raalte and D. W. Fairbanks Stylus Tip Positioning Technique (4,341,437)
J. J. Williams, Jr. and R. A. Dischert Hardware Reduction By Truncation of Selected Number of Most Significant Bits for Digital Video System Using Subsampling and Adaptive Reconstruction (4,340,940)
H. J. Wolkstein Optimization Circuit for a Serrodyne Frequency Translator (4,338,528)

August

T. E. Benner Mesh Assembly Having Reduced Microphonics for a Pick-up Tube (4,347,459)
D. A. Berry, J. R. Preston and L. J. Hillenbrand High Density Information Disc Lubricants (4,342,660)
J. C. Bleazey and J. Guarracini Driver Arrangement for Stylus Lifting/Lowering Apparatus (4,344,166)
D. Botez Single Filament Semiconductor Laser with Large Emitting Area (4,347,486)
S. L. Corsover, L. W. Dobbins and P. B. Pierson Variable-Velocity Film Exposing and Developing Apparatus (4,344,088)
A. M. Goodman and M. L. Tarng Method of Passivating A Semiconductor Device with a Multi-Layer Passivant System by Thermally Growing a Layer of Oxide on an Oxygen Doped Polycrystalline Silicon Layer (4,344,985)
R. J. Gries, C. E. Conn and S. Miko Television Receiver High Frequency Regulated Power Supply Including a Low Voltage Ferroresonant Transformer Coupled to a Step-Up High Voltage Transformer (4,345,188)
J. R. Harford Variable Load Impedance Gain-Controlled Amplifier (4,344,043)
J. R. Harford Gain-Controlled Amplifier Utilizing Variable Emitter Degeneration and Collector Load Impedance (4,344,044)
J. R. Harford Variable Emitter Degeneration Gain-Controlled Amplifier (4,345,214)
J. W. Harmon and J. H. Atherton Low Power Voltage Multiplier Circuit (4,344,003)
J. E. Hicks Television Receiver High Voltage Generator Protection Circuit (4,343,028)
L. J. Hillenbrand, J. R. Preston and D. A. Berry High Density Information Disc (4,346,469)
L. B. Johnston System for Compensating for Transfer Characteristic Variations of Electron Guns (4,344,021)
W. A. Lagoni Apparatus for Reducing the Effect of Co-Channel Interference on Synchronizing Pulses (4,343,019)
F. D. Marschka Screen Contact Means for a Cathode Ray Tube (4,344,015)
W. Phillips, C. C. Neil and J. M. Hammer Method for Making Planar Optical Waveguide Comprising Thin Metal Oxide Film Incorporating a Relief Phase Grating (4,343,890)
J. R. Preston, L. J. Hillenbrand and D. A. Berry High Density Information Disc (4,346,468)
J. E. Rudy Timing Circuit for the Digital Generation of Composite Luminance and Chrominance Video Signal for Non-Interlaced Television Raster Scan-Line Pattern (4,344,075)
W. W. Salt, Jr. Retainer Ring for Securing Substrates in a Vacuum Deposition System (4,344,383)
O. H. Schade, Jr. Differential-Input Amplifier Circuitry with Increased Common-Mode Voltage Range (4,345,213)
O. H. Schade, Jr. Compensation of Base-Current-Related Error in Current Mirror Amplifier Circuitry (4,345,216)
W. F. Speer Rotary Tuning Mechanism (4,347,628)
R. G. Stewart Power Gated Decoding (4,344,005)
M. L. Tarng Etching a Semiconductor Material and Automatically Stopping Same (4,343,676)
B. K. Taylor Removable Protective Cover for a VideoDisc Stylus Cartridge (4,342,394)
C. M. Tomasetti and J. A. Ulaky Photomultiplier Tube Having a Gain Modifying Nichrome Dynode (4,347,458)
C. C. Wang, L. Ekstrom, T. C. Lausman and H. Wielicki VideoDisc Lubricants (4,342,659)
M. H. Wardell, Jr. Electron Tube Base with Flow Channels Therein (4,345,812)
G. C. Waybright High Voltage Protection Circuit for a Television Receiver (4,345,275)
C. E. West and R. J. Ramspacher Transistor Heat Sink Assembly (4,344,106)
P. C. Wilmarth Method for Making Printed Circuit Boards with Connector Terminals (4,343,084)
O. M. Woodward and J. G. Henderson Loop Antenna Arrangements for Inclusion in a Television Receiver (4,342,999)

September

F. Aschwanden Comparison Arrangement for a Digital Tuning System (4,352,206)
J. H. Atherton and C. P. Jindra Signal Comparison Circuit (4,348,596)

D. A. Berry High Density Information Disc Lubricants (4,351,048)
J. F. Bull Actuation Rate Limiter (4,349,754)
F. Caprari Radiation Shadow Projection Exposure System (4,348,105)
M. G. Caracappa System and Method for Frequency Discrimination (4,352,194)
D. J. Carlson and S. H. Tsou Multi-Band Antenna Coupling Network (4,352,111)
C. A. Catanese and S. Bloom Multicolor Cathode-Ray Tube with Quadrupolar Focusing Color-Selection Structure (4,350,922)
H. N. Crooks VideoDisc Player Having Record Side Identifying Apparatus (4,352,175)
A. T. Crowley Precise Digitally Programmed Frequency Source (4,349,887)
M. T. Duffy and P. J. Zanzucchi Method and Apparatus for Determining the Quality of a Semiconductor Surface (4,352,016)
M. T. Duffy, J. F. Corboy and P. J. Zanzucchi Apparatus for Determining the Quality of a Semiconductor Surface (4,352,017)
C. A. Elliott VideoDisc Player Having Carriage Detent Mechanism (4,351,046)
T. J. Faith, Jr. Monitor for Oxygen Concentration in Aluminum-Based Films (4,348,886)
D. W. Flatley and S. T. Hsu Process for Tapering Openings in Ternary Glass Coatings (4,349,584)
J. E. Gillberg Circuit with Dual-Purpose Terminal (4,350,906)
N. F. Gubitose, M. R. Schuler and D. L. Patterson Crystal Seed Holder Assembly (4,348,365)
W. E. Harlan Self-Limiting Video Signal Peaking Circuit (4,350,995)
W. E. Harlan Automatic Video Signal Peaking Control (4,351,003)
J. G. Henderson Apparatus for Automatically Steering an Electrically Steerable Television Antenna (4,349,840)
M. E. Hertzler System for Applying a Liquid to the Studs of a Color Kinescope Faceplate Panel (4,351,265)
M. D. Holbrook and W. K. Knapp Precharge Circuit (4,352,031)
R. H. Hughes Electron Gun with Balanced Lens Lips to Reduce Astigmatism (4,350,923)
L. L. Jastrzebski and P. A. Levine Semiconductor Imagers (4,348,690)
N. R. Landry Coax to Rectangular Waveguide Coupler (4,349,790)
F. D. Marschka Main Lens Assembly for an Electron Gun (4,350,925)
F. Okamoto and K. Kato Method for Preparing Inorganic Sulfides (4,348,299)
L. L. Rarig, R. A. Alleman and D. L. Miller Apparatus for Sensing Bare Metal on a Moving Strip of Insulatively Coated Conductive Material (4,351,263)
G. A. Reitmeier and R. A. Dischert Adaptive Composite-Component Transcoding Hierarchy for Digital Video (4,352,122)
P. D. Southgate and J. P. Beltz Inspection System for Detecting Defects in Regular Patterns (4,349,880)
S. N. Subbarao and H. Huang Method for Fabricating Via Holes in a Semiconductor Wafer (4,348,253)
M. L. Tarng and W. A. Hicinbothem, Jr. Method of Depositing a Refractory Metal on a Semiconductor Substrate (4,349,408)
M. Toda and S. Osaka Fluid Flow Velocity Sensor Using a Piezoelectric Element (4,351,192)
J. Valachovic, G. A. Alphonse, J. H. Reisner and K. F. Etzold Piezoelectric Transducer for Recording Video Information (4,349,902)

AUTHORS

Curtis Carlson is a Tau Beta Pi graduate from Worcester Polytechnic Institute, where he received his BS degree in Physics in 1967. He received his MS and PhD degrees from Rutgers University in 1969 and 1973, respectively. Since joining the technical staff of RCA Laboratories in 1973, Dr. Carlson has been involved in the general areas of imaging devices, image analysis, and human perception. He is a member of the SMPTE Vision Committee on High Definition Television and was recently a Special Editor of an issue of the SID Proceedings on "Advances in Visual Information Processing." In 1979, he received an RCA Individual Outstanding Achievement Award. Dr. Carlson is currently Head of Image Quality and Human Perception at RCA Laboratories.

Hammam Elabd received the BSc degree in Electrical Engineering from Cairo University, Egypt, in 1969, and MSc degrees from the University of Arkansas, Fayetteville, AR, and Rensselaer Polytechnic Institute, Troy, NY, in 1975 and 1979, respectively. He received the PhD degree in Electrical Engineering from Rensselaer Polytechnic Institute in 1979. His PhD thesis described the material, optical, and electrical properties of the PbS-Si heterojunction infrared detector. From 1969 to 1970 Dr. Elabd worked as a system analyst and programmer in the Suez Canal Co. and Cairo University Computer Center. From 1970 to 1975 he was a member of the technical staff of Brown Boveri and Cie A.G., Mannheim, West Germany. From 1974 to 1979 he was a research assistant in the area of solid-state devices in the Department of Electrical Engineering of the University of Arkansas, Purdue University, and Rensselaer Polytechnic Institute. During the same period he served as a consultant and lecturer in the areas of power electronics, remote control, telemetry, and load management systems. He is currently a member of the technical staff at RCA Laboratories Princeton, N.J., where he is involved in the development of Schottky Barrier IR-CCD arrays. This work has led to contributions in the areas of detector process development for the platinum silicide and paladium silicide Schottky-barrier detectors, and detector and IR-CCD image sensor characterization. In 1981 he was awarded an RCA Oustanding Achievement Award for contributions to the science and technology of Schottky-Barrier infrared detectors that have led to the development of high performance IR-CCD image sensors.

Dr. Elabd is a member of the IEEE and the society of Photo-Optical Instrumentation Engineers.

Scott A. Keneman received BSEE and MSEE degrees from the Massachusetts Institute of Technology in 1967 and the PhD in Electrical Engineering from the University of Pennsylvania in 1974. He joined RCA Laboratories in 1964 as a member of the MIT-RCA Co-Op Program. Following a number of years of research applying superconductive, electro-optics, and gaseous electronics technologies to memories and displays, Dr. Keneman joined the New Products Laboratory of the Consumer Electronics Division in 1978 to assess new technologies for RCA's existing and future product lines. In June, 1980, he was made Manager, TV Digital Systems, in the New Products Lab. In this capacity, he is responsible for the development of TV tuning, remote control systems, and Teletext Decoder Products.

Dr. Keneman is a member of the IEEE, Eta Kappa Nu, Tau Beta Pi, and Sigma Xi. He has been granted 6 patents.

Walter F. Kosonocky was awarded BS (1955) and MS (1957) degrees in Electrical Engineering by Newark College of Engineering, Newark, NJ. In 1965, he received the ScD degree in Engineering from Columbia University, New York, NY. Since June 1955, he has been employed at RCA Laboratories, Princeton, NJ. He was appointed a Fellow of the Technical Staff in 1979. At RCA Laboratories, Dr. Kosonocky has been engaged in research on solid-state devices, circuits, and system applications. This work included the following areas: ferrite memories, parametric digital circuits, tunnel diode circuits, applications of lasers as switching and digital devices, optical hologram memories, and MOS photosensor arrays. From 1970 to 1977, he was engaged in the development of charge-coupled devices for digital, imaging, and signal processing applications. Since 1977, he has led a team effort on the development of Schottky-barrier infrared image sensors. He has been granted 38 U.S. patents. He received RCA Laboratories Achievement Awards in 1959, 1963, and 1980, and the RCA David Sarnoff Award in 1981.

Dr. Kosonocky is a member of Tau Beta Pi, Eta Kappa Nu, and Sigma Xi, and Fellow of IEEE. From 1963 to 1967, he was Chairman of the Solid-State Circuits Committee of IEEE's Circuits and Systems Society. From 1974 to 1978, he served as Chairman of the Integrated Circuits Technology Committee of the IEEE Electron Devices Society. He is presently the Chairman of the VLSI Committee of the IEEE Electron Devices Society.

Dietrich Meyerhofer studied Engineering Physics at Cornell University and received the PhD degree in Physics from MIT in 1957. Since 1958 he has been a staff member at the RCA Laboratories in Princeton, NJ. His research activities have included the study of electrical properties of semiconductors and insulators, of light emission from semiconductor diodes and lasers, and of Q-switching of the CO_2 laser. Dr. Meyerhofer investigated electronic applications in the printing industry, including the use of holograms for printing and microfiche. He has carried out studies of electro-optic effects in liquid crystals and of the mech-

anisms underlying the functioning of dynamic scattering and field-effect display devices. Currently, Dr. Meyerhofer is involved in testing and characterizing resists for microlithography, comparisons of exposures by uv light and electron beams, and modelling of exposure and development processes.

Dr. Meyerhofer is a member of the American Physical Society, the IEEE, and of Sigma Xi.

Joe Mitchell received his B.S. degree from Seton Hall University in 1961 and his M.S. from Rutgers in 1978, both in Physics. He joined Weston Instruments in 1961 where he worked for four years on thin film techniques for microcircuitry and photoconductors. He came to RCA in 1966 as a member of the DME group in Somerville where he worked on thin film microcircuits, photodiode arrays, the fabrication of acoustic wave devices, and microwave integrated circuits. In 1972, he was transferred to the Microwave Technology Center of RCA Laboratories where he was responsible for the fabrication of microwave integrated circuits and components. He returned to Somerville in 1973 to work on thermal compression bonding of lead frames to ceramic packages in SSTC. In 1974, he joined the SSTC Photomask group where he assumed responsibility for new processing techniques and equipment. In that capacity, he was an original task force member involved in the training and acceptance testing on RCA's MEBES Electron Beam Lithography system. As a senior member of the technical staff, he is presently responsible for the processing and quality of Electron Beam Photomasks made on MEBES.

Richard Mooney joined RCA in 1967, working in a number of areas including Consumer Electronics Division's TV Engineering group and "SelectaVision" video cassette recorder group. He is presently working in the Technical Training Department, responsible for training RCA Distributor service personnel in circuit operation and troubleshooting techniques on various consumer products marketed by RCA.

Rabah Shahbender received a Ph.D. in Electrical Engineering from the University of Illinois. He joined RCA in Camden, N.J., in 1955 as a development engineer. In 1959, he transferred to RCA Laboratories in Princeton, N.J., where he has been active in the areas of physical electronics, digital devices, and digital memories.

Dr. Shahbender is a Fellow of IEEE, a member of AAAS, Sigma Xi, and Eta Kappa Nu, and a Fellow of the University of Illinois.

Kenneth M. Schlesier received the B.S. from Newark College of Engineering in 1965 and the Ph.D degree in device physics from Princeton University in 1970. He joined the Technical Staff of RCA Laboratories, Princeton, NJ where he worked on MOS device physics and wafer processing. He made several contributions to the development of radiation hardened CMOS circuits and has presented invited papers and several internal reports on this subject. In 1974 Dr. Schleisier was a co-recipient of an RCA Laboratories Achievement Award for work in dielectric materials. In 1976 Dr. Schlesier concentrated his efforts on reliability aspects of CMOS integrated circuits including dielectric breakdown and threshold stability of mass-produced CMOS circuits. He also participated in a highly successful team effort for improving yield of a high volume CMOS-LSI process.

In 1978, he joined the New Products Laboratory of the RCA Consumer Electronics Division (CE), Indianapolis, Indiana, where he worked on reliability and performance of ICs used by Consumer Electronics. In 1979, Dr. Schlesier rejoined the RCA Laboratories staff and studied the effects of piezoresistivity on performance and reliability of plastic packaged ICs. He is now working on reliability aspects of advanced CMOS IC technologies.

Dr. Schlesier is a member of IEEE.

Binboga Siddik Yarman received his BS degree in Electrical Engineering from the Technical University of Istanbul, Istanbul, Turkey, in 1974 and his MEEE from Stevens Institute of Technology in New Jersey in 1977. He completed his Ph.D. in the area of broadband matching at Cornell University in November 1981. In 1982, he joined RCA Laboratories, David Sarnoff Research Center, Princeton, N.J. He is currently working on new design concepts for broadband, multi-stage microwave amplifiers. His interests include analytic and computer-aided designs of passive and active microwave circuits.

Dr. Yarman is a member of the IEEE and the Turkish Electrical Engineers Chamber.

Joseph Zelez received a B.A. in Physics from Temple University in 1968. He joined the RCA Laboratories as a research technician in 1963. His work involved vacuum evaporation of thin films for a variety of applications. In 1969, he became a project engineer at Ansley East Corporation in Doylestown, PA where he was responsible for optical thin film design and fabrication. In 1970 he was appointed thin film product manager at Kinney Vacuum Co. in Pennsauken, NJ. In 1971 he became manager of thin film operations at the Intek Corporation in Middletown, PA. He rejoined RCA Laboratories in 1975 in the Thin Film Technology group where he is currently an Associate Member of the Technical Staff. Since then his work has involved thin film deposition and etching for a variety of applications. His principal interests are in dc and rf sputtering, quantitative residual gas analysis, electron beam gun technology and microlithography.

Mr. Zelez holds 3 U.S. patents. He is a member of the Optical Society of America and the American Vacuum Society.

Index Volume 43, 1982

March

1. VideoDisc Mastering

5 **VideoDisc Mastering—An Overview**
J. A. van Raalte

21 **Principles for the Design of Cutters for VideoDisc Recording**
J. H. Reisner, J. Valachovic, R. E. Simms, and H. I. Moss

35 **Power Dissipation in Piezoelectric Cutterheads**
G. A. Alphonse

44 **Thermal Analysis of VideoDisc Cutter**
R. Shahbender

57 **Approximate Resonance Spectrum of a VideoDisc Cutter**
R. Shahbender, K. S. Vanguri, and B. T. Khuri-Yakub

66 **Micromachining VideoDisc Grooves and Signals**
J. Guarracini, J. H. Reisner, J. L. Walentine, and C. A. Whybark

84 **A Method for the Characterization of Piezoelectric VideoDisc Recording Heads Using a Bridge Circuit**
G. A. Alphonse

95 **A Quadrature Michelson Interferometer System for Probing Surface Vibrations—Applications to VideoDisc Cutters**
K. F. Etzold

116 **Testing Methods for the Characterization of Cutterhead Performance in Mastering VideoDiscs**
R. L. Truesdell

126 **High Performance Optical Reader for Substrates**
M. Lurie, W. Barnette, I. Gorog, and R. Jebens

2. Stylus and Pickup Circuit

167 **The VideoDisc Stylus Electrode**
H. L. Pinch, D. A. Furst, and R. T. Smith

179 **Basics of VideoDisc Stylus Dynamics and Interaction with Surface Imperfections**
R. W. Nosker and D. L. Matthies

194 **Capacitive-Pickup Circuitry for VideoDiscs**
R. C. Palmer, E. J. Denlinger, and H. Kawamoto

3. VideoDisc Record

212 **Electrical and Physical Properties of Carbon-Filled PVC for Capacitance Pickup VideoDiscs**
P. Datta and H. Kawamoto

224 **Capillary Behavior and Lubricating Properties of the RCA VideoDisc**
R. Williams and C. C. Wang

4. System Testing

228 **VideoDisc Systems at the RCA David Sarnoff Research Center**
D. P. Barton, R. R. Barton, M. Blecker, P. W. Lyons, K. A. Pitts, P. G. Stein, and J. R. Woolston

257 **Patents**

260 **Authors**

June

277 **An Optical Communications Link in the 2.0–6.0 GHz band**
Daniel W. Bechtle and Stefan A. Siegel

310 **Fluorescent Tracers—Powerful Tools for Studying Corrosion Phenomena and Defects in Dielectrics**
Werner Kern, Robert B. Comizzoli,and George L. Schnable

339 **Simplified Analysis of Kinescope Electron Guns**
D. A. de Wolf

363 **Miniature Beryllia Circuits—A New Technology for Microwave Power Amplifiers**
F. N. Sechi, R. Brown, H. Johnson, E. Belohoubek, E. Mykietyn, and M. Oz

375 **Interpreting the Beta Versus Collector Current and Temperature Characteristics of a Transistor**
Robert Amantea

391 **Positive and Negative Tone Near-Contact Printing of Contact Hole Maskings**
Lawrence K. White

412 **Authors**

418 **Patents**

September

423 **Chemically Vapor-Deposited Borophosphosilicate Glasses for Silicon Device Applications**
Werner Kern and George L. Schnable

458 **A Radiation Hardened 256X4 Bulk CMOS RAM**
L. S. Napoli, R. K. Smeltzer, R. Donnelly, and J. Yeh

464 **Single Sideband, Amplitude Modulated, Satellite Voice Communication System Having 6000 Channels per Transponder**
Krishnamurthy Jonnalagadda

489 **Broadband Microwave Power Amplifiers Using Lumped-Element Matching and Distributed Combining Techniques**
R. L. Camisa and A. Mikelsons

504 **Offset Near-Field Gregorian Antenna Scanning Beam Analysis**
Eugene C. Ngai

529 **A Simplified Real Frequency Technique for Broadband Matching a Complex Generator to a Complex Load**
B. S. Yarman

542 **The Photoresponse of Thin-Film PtSi Schottky Barrier Detectors with Optical Cavity**
Hamman Elabd and Walter F. Kosonocky

548 **Theory of Large-Angle Deflection of Electrons in the Magnetic Field Inside a Television Tube**
Basab B. Dasgupta

558 **Patents**

561 **Authors**

December

569 **Theory and Measurements of Photoresponse for Thin Film Pd_2Si and PtSi Infrared Schottky-Barrier Detectors with Optical Cavity**
Hamman Elabd and Walter F. Kosonocky

590 **Peizoresistivity Effects in Plastic-Encapsulated Integrated Circuits**
Kenneth M. Schlesier, Scott A. Keneman, and Richard T. Mooney

608 **Proximity Printing of Chrome Masks**
Dietrich Meyerhofer and Joe Mitchell

626 **Real Frequency Broadband Matching Using Linear Programming**
B.S. Yarman

655 **Forces Acting on the Tool in VideoDisc Masting**
Rabah Shahbender

665 **A Diamond-Like Carbon Film**
Joseph Zelez

675 **Sine-Wave Threshold Contrast Sensitivity Function: Dependence on Display Size**
C. R. Carlson

684 **Patents**

687 **Authors**

691 **Index to Volume 43, 1982**

Index to Authors, Volume 43, 1982

G. A. Alphonse Power Dissipation in Piezoelectric Cutterheads, March, p. 35
—A Method for the Characterization of Piezoelectric VideoDisc Recording Heads Using a Bridge Circuit, March, p. 84
R. Amantea Interpreting the Beta Versus Collector Current and Temperature Characteristics of a Transistor, June, p. 375
W. Barnette High Performance Optical Reader for Substrates, March, p. 128
D. P. Barton VideoDisc Systems Testing at the RCA David Sarnoff Research Center, March, p. 228
R. R. Barton VideoDisc Systems Testing at the RCA David Sarnoff Reserch Center, March, p. 228
D. W. Bechtle An Optical Communications Link in the 2.0–6.0 GHz Band, June, p. 277
E. Belohoubek Miniature Beryllia Circuits—A New Technology for Microwave Power Amplifiers, June, p. 363
M. Blecker VideoDisc Systems Testing at the RCA David Sarnoff Reserch Center, March, p. 228
R. Brown Miniature Beryllia Circuits—A New Technology for Microwave Power Amplifiers, June, p. 363
R. L. Camisa Broadband Microwave Power Amplifiers Using Lumped-Element Match-

ing and Distributed Combining Techniques, September, p. 489
C. R. Carlson Sine-Wave Threshold Contrast Sensitivity Function: Dependence on Display Size, December, p. 675
R. B. Comizzoli Fluorescent Tracers—Powerful Tools for Studying Corrosion Phenomena, June, p. 310
B. B. Dasgupta Theory of Large-Angle Deflection of Electrons in the Magnetic Field Inside a Television Tube, September, p. 548
P. Datta Electrical and Physical Properties of Carbon-Filled PVC for Capacitance Pickup VideoDiscs, March, p. 212
E. J. Denlinger Capacitive-Pickup Circuitry for VideoDiscs, March, p. 194
D. A. deWolf Simplified Analysis of Kinescope Electron Guns, June, p. 339
R. Donnelly A Radiation Hardened 256X4 Bulk CMOS RAM, September, p. 458
H. Elabd The Photoresponse of Thin-Film PtSi Schottky Barrier Detectors with Optical Cavity, September, p. 542
—Theory and Measurements of Photoresponse for Thin-Film Pd_2Si and PtSi Infrared Schottky-Barrier Detectors with Optical Cavity, December, p. 569
K. F. Etzold A Quadrature Michelson Inferometer System for Probing Surface Vibrations—Applications to VideoDisc Cutters, March, p. 95
D. A. Furst The VideoDisc Stylus Electrode, March, p. 167
I. Gorog High Performance Optical Reader for Substrates, March, p. 128
J. Guarracini Micromachining VideoDisc Grooves and Signals, March, p. 66
R. Jebens High Performance Optical Reader for Substrates, March, p. 128
H. Johnson Miniature Beryllia Circuits—A New Technology for Microwave Power Amplifiers, June, p. 363
K. Jonnalagadda Single Sideband, Amplitude Modulated, Satellite Voice Communication System Having 6000 Channels per Transponder, September, p. 464
H. Kawamoto Capacitive-Pickup Circuitry for VideoDiscs, March, p. 194
—Electrical and Physical Properties of Carbon-Filled PVC for Capacitive Pickup VideoDisc, March, p. 212
S. A. Keneman Piezoresistivity Effects in Plastic-Encapsulated Integrated Circuits, December, p. 590
W. Kern Fluorescent Tracers—Powerful Tools for Studying Corrosion Phenomena and Defects in Dielectrics, June, p. 310
—Chemically Vapor-Deposited Borophosphosilicate Glasses for Silicon Device Applications, September, p. 423
B. T. Khuri-Yakub Approximate Resonance Spectrum of a VideoDisc Cutter, March, p. 57
W. F. Kosonocky The Photoresponse of Thin-Film PtSi Schottky Barrier Detectors with Optical Cavity, September, p. 542
—Theory and Measurements of Photoresponse for Thin Film Pd_2Si and PtSi Infrared Schottky-Barrier Detectors with Optical Cavity, December, p. 569
M. Lurie High Performance Optical Reader for Substrates, March, p. 128
P. W. Lyons VideoDisc Systems Testing at the RCA David Sarnoff Research Center, March, p. 228
D. L. Matthies Basics of VideoDisc Stylus Dynamics and Interaction with Surface Imperfections, March, p. 179
D. Meyerhofer Proximity Printing of Chrome Masks, December, p. 608
A. Mikelsons Broadband Microwave Power Amplifiers Using Lumped-Element Matching and Distributed Combining Techniques, September, p. 489
J. Mitchell Proximity Printing of Chrome Masks, December, p. 608
R. T. Mooney Piezoresistivity Effects in Plastic-Encapsulated Integrated Circuits, December, p. 590
H. I. Moss Principles for the Design of Cutters for VideoDisc Recording, March, p. 21
E. Mykietyn Miniature Beryllia Circuits—A New Technology for Microwave Power Amplifiers, June, p. 363
L. S. Napoli A Radiation Hardened 256X4 Bulk CMOS RAM, September, p. 458
R. W. Nosker Basics of VideoDisc Stylus Dynamics and Interaction with Surface Imperfections, March, p. 179
E. C. Ngai Offset Near-Field Gregorian Antenna Scanning Beam Analysis, September, p. 504
M. Oz Miniature Beryllia Circuits—A New Technology for Microwave Power Amplifiers, June, p. 363
R. C. Palmer Capacitive-Pickup Circuitry for VideoDisc, March, p. 194
H. L. Pinch The VideoDisc Stylus Electrode, March, p. 167

K. A. Pitts VideoDisc Systems Testing at the RCA David Sarnoff Research Center, March, p. 228
J. H. Reisner Principles for the Design of Cutters for VideoDisc Recording, March, p. 21
—Micromachining VideoDisc Grooves and Signals, March, p. 66
K. M. Schlesier Piezoresistivity Effects in Plastic-Encapsulated Integrated Circuits, December, p. 590
G. L. Schnable Fluorescent Tracers—Powerful Tools for Studying Corrosion Phenomena and Defects in Dielectrics, June, p. 310
—Chemically Vapor-Deposited Borophosphosilicate Glasses for Silicon Device Applications, September, p. 423
F. N. Sechi Miniature Beryllia Circuits—A New Technology for Microwave Power Amplifiers, June, p. 363
R. Shahbender Thermal Analysis of VideoDisc Cutter, March, p. 44
—Approximate Resonance Spectrum of a VideoDisc Cutter, March, p. 57
—Forces Acting on the Tool in VideoDisc Mastering, December, p. 655
S. A. Siegel An Optical Communication Link in the 2.0–6.0 GHz Band, June, p. 277
R. E. Simms Principles for the Design of Cutters for VideoDisc Recording, March, p. 21
R. K. Smeltzer A Radiation Hardened 256X4 Bulk CMOS RAM, September, p. 458
R. T. Smith The VideoDisc Stylus Electrode, March, p. 167
P. G. Stein VideoDisc Systems Testing at the RCA David Sarnoff Research Center, March, p. 228
R. L. Truesdell Testing Methods for the Characterization of Cutterhead Performance in Mastering VideoDiscs, March, p. 116
J. Valachovic Principles for the Design of Cutters for VideoDisc Recording, March, p. 21
K. S. Vanguri Approximate Resonance Spectrum of a VideoDisc Cutter, March, p. 57
J. A. vanRaalte VideoDisc Mastering—An Overview, March, p. 5
J. L. Walentine Micromachining VideoDisc Grooves and Signals, March, p. 66
C. C. Wang Capillary Behavior and Lubricating Properties of the RCA VideoDisc, March, p. 224
L. K. White Positive and Negative Tone Near-Contact Printing of Contact Hole Masks, June, p. 391
C. A. Whybark Micromachining VideoDisc Grooves and Signals, March, p. 66
R. Williams Capillary Behavior and Lubricating Properties of the RCA VideoDisc, March, p. 224
J. R. Woolston VideoDisc Systems Testing at the RCA David Sarnoff Research Center, March, p. 228
B. S. Yarman A Simplified Real Frequency Technique for Broadband Matching a Complex Generator to a Complex Load, September, p. 529
—Real Frequency Broadband Matching Using Linear Programming, December, p. 626
J. Yeh A Radiation Hardened 256X4 Bulk CMOS RAM, September, p. 458
J. Zelez A Diamond-Like Carbon Film, December, p. 665

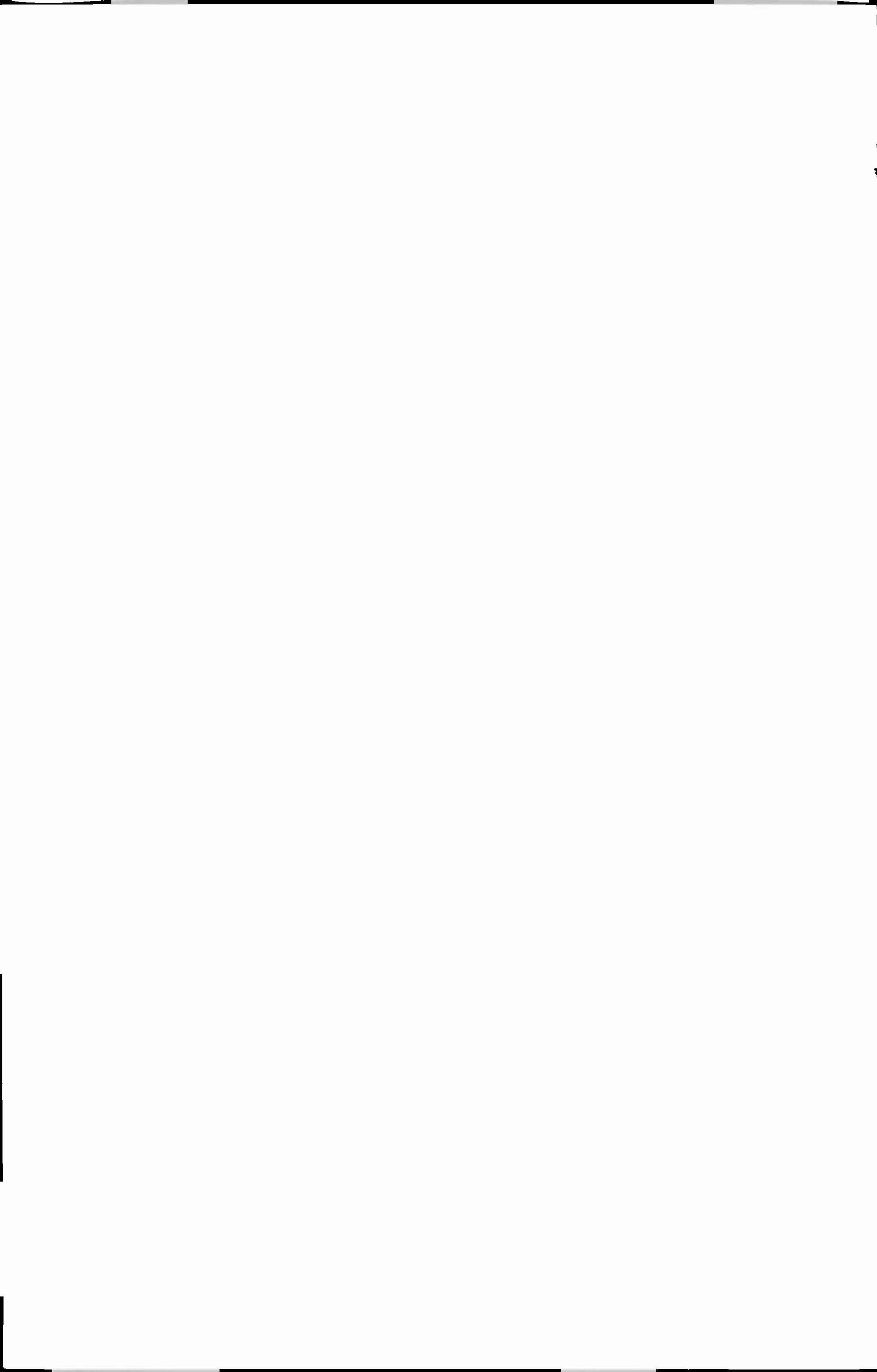

STATEMENT OF OWNERSHIP

Statement of Ownership, Management and Circulation (Act of August 12, 1970, Section 3685, Title 39, United States Code).

1. Title of Publication: RCA REVIEW, Publication No. 00336831. 2. Date of Filing: September 30, 1982. 3. Frequency of Issue: Quarterly. No. of Issues Published Annually: Four (4). Annual Subscription Price $8.00. 4. Complete Mailing Address of Known Office of Publication: RCA—David Sarnoff Research Center, Princeton, Mercer County, New Jersey 08540. 5. Complete Mailing Address of the Headquarters or General Business Offices of the Publishers: RCA—David Sarnoff Research Center, Princeton, New Jersey, Mercer County, New Jersey 08540. 6. Full Names and Complete Mailing Address of Publisher, Editor, and Managing Editor: Publisher—RCA Corporation, Research & Engineering, Princeton, New Jersey 08540, Editor/Managing Editor—Ralph F. Ciafone, RCA, David Sarnoff Research Center, Princeton, New Jersey 08540. 7. Owner: Cede & Company, Box 20, Bowling Green Station, New York, New York 10004; Kray & Company, 120 S. LaSalle Street, Chicago, Illinois 60603; Pacific & Company, Box 7877, San Francisco, California 94120. 8. Known Bondholders, Mortgagees, and Other Security Holders: Metropolitan Life Insurance Company, 1 Madison Avenue, New York, New York 10010; New York Life Insurance Company, 51 Madison Avenue, New York, New York 10010; John Hancock Mutual Life Insurance Company, Hancock Place, Boston, Massachusetts 02117; The Mutual Benefit Life Insurance Company, 520 Broad Street, Newark, New Jersey 07101. 10. Extent and Nature of Circulation: Average No. Copies Each Issue During Preceding 12 Months, and Actual No. Copies of Single Issue Published Nearest to Filing Date, respectively, are as follows: (A) Total No. Copies (Net Press Run) 4,580–3,800; (B) Paid Circulation—1. Counter Sales 463–545; 2. Mail Subscriptions 2,662–2,410; (C) Total Paid Circulation 3,125–2,955; (D) Free Distribution by Mail, Carrier, or Other Means-Samples, Complimentary, and Other Free Copies 314–347; (E) Total Distribution 3,439–3,302; (F) Copies Not Distributed—Office Use, Left Over, Unaccounted, Spoiled After Printing 1,141–498; (G) Total 4,580-3,800. I certify that the statements made by me above are correct and complete.

Ralph F. Ciafone, Editor